UNIVERSITAT ROVIRA I VIRGILI

COMPUTATIONAL CHEMISTRY FOR HOMOGENEOUS REDOX CATALYSIS

Ignacio Funes Ardoiz

ADVERTIMENT. L'accés als continguts d'aquesta tesi doctoral i la seva utilització ha de respectar els drets de la persona autora. Pot ser utilitzada per a consulta o estudi personal, així com en activitats o materials d'investigació i docència en els termes establerts a l'art. 32 del Text Refós de la Llei de Propietat Intel·lectual (RDL 1/1996). Per altres utilitzacions es requereix l'autorització prèvia i expressa de la persona autora. En qualsevol cas, en la utilització dels seus continguts caldrà indicar de forma clara el nom i cognoms de la persona autora i el títol de la tesi doctoral. No s'autoritza la seva reproducció o altres formes d'explotació efectuades amb finalitats de lucre ni la seva comunicació pública des d'un lloc aliè al servei TDX. Tampoc s'autoritza la presentació del seu contingut en una finestra o marc aliè a TDX (framing). Aquesta reserva de drets afecta tant als continguts de la tesi com als seus resums i índexs.

ADVERTENCIA. El acceso a los contenidos de esta tesis doctoral y su utilización debe respetar los derechos de la persona autora. Puede ser utilizada para consulta o estudio personal, así como en actividades o materiales de investigación y docencia en los términos establecidos en el art. 32 del Texto Refundido de la Ley de Propiedad Intelectual (RDL 1/1996). Para otros usos se requiere la autorización previa y expresa de la persona autora. En cualquier caso, en la utilización de sus contenidos se deberá indicar de forma clara el nombre y apellidos de la persona autora y el título de la tesis doctoral. No se autoriza su reproducción u otras formas de explotación efectuadas con fines lucrativos ni su comunicación pública desde un sitio ajeno al servicio TDR. Tampoco se autoriza la presentación de su contenido en una ventana o marco ajeno a TDR (framing). Esta reserva de derechos afecta tanto al contenido de la tesis como a sus resúmenes e índices.

WARNING. Access to the contents of this doctoral thesis and its use must respect the rights of the author. It can be used for reference or private study, as well as research and learning activities or materials in the terms established by the 32nd article of the Spanish Consolidated Copyright Act (RDL 1/1996). Express and previous authorization of the author is required for any other uses. In any case, when using its content, full name of the author and title of the thesis must be clearly indicated. Reproduction or other forms of for profit use or public communication from outside TDX service is not allowed. Presentation of its content in a window or frame external to TDX (framing) is not authorized either. These rights affect both the content of the thesis and its abstracts and indexes.

Ignacio Funes Ardoiz

Computational Chemistry for Homogeneous Redox Catalysis

DOCTORAL THESIS

Supervised by

Prof. Feliu Maseras

Institute of Chemical Research of Catalonia

UNIVERSITAT ROVIRA I VIRGILI

ICIQ
Institut
Català
d'Investigació
Química

EXCELENCIA
SEVERO
OCHOA

Tarragona

2017

ICIQ - Institut Català d'Investigació Química

Avgda, Països Catalans 16,

43007 Tarragona (Spain)

Prof. Feliu Maseras, Group Leader at the Institute of Chemical Research of Catalonia,

I STATE that the present study, entitled "Computational Chemistry for Homogeneous Redox Catalysis" presented by Ignacio Funes Ardoiz for the award of the degree of Doctor, has been carried out under my supervision in my group at the Institute of Chemical Research of Catalonia and that it fulfills all the requirements to be eligible for the International Doctor Distinction.

Tarragona, June 30th, 2017

Doctoral Thesis Supervisor

Prof. Feliu Maseras

Acknowledgments

The elaboration of this thesis would not have been possible without the support of many friends and co-workers.

Me gustaría empezar por agradecer a mi supervisor, el profesor Feliu Maseras. La verdad es que nunca imagine las vueltas que daría a mi vida su aparición. Allá por 2012, él me aceptó en su grupo como SummerFellow, y desde entonces su apoyo ha sido constante. Me dio la oportunidad de hacer el máster en su grupo y posteriormente el doctorado. Yo no soy un alumno fácil. Me gusta discutir, dar guerra, y sobretodo tener cierta independencia en el camino que debo seguir. Feliu siempre ha comprendido esto, y no he podido tener mejor guía. Me gustaría hacer también una mención especial a su apoyo en las actividades de divulgación, tan necesaria en nuestra sociedad. Él lo ha visto siempre como tiempo invertido y no perdido, llegando a acompañarme en mi primera actuación en público. Y tras varios años, ahora es Feliu el que me envía la información de eventos nuevos, por ser el que "gana cosas raras". La verdad es que no me he podido sentir más cómodo en su grupo.

Durante mi estancia en el ICIQ he conocido también a muchísima gente que me ha facilitado la vida, tanto profesional como personalmente. Me gustaría agradecer el apoyo a la familia de los teóricos, en especial a Adiran y a su móvil, por ser mis compañeros de descanso. No me puedo olvidar tampoco de todos los amigos que he hecho a lo largo de los años, Víctor, Fernando, Sergi, Marcos, Ximo, Dolores y otros muchos que estoy seguro de que me dejo en el tintero. En cuanto a la ciencia, los profesores Núria López y Carles Bo siempre han estado ahí cuando he tenido algún problema, compartiendo su experiencia conmigo. Finalmente, en este apartado tengo que hacer especial mención a Núria Vendrell, que ha hecho que el papeleo siempre estuviera a tiempo y en orden, aunque yo fuese un auténtico desastre.

Me gustaría dar las gracias también a los profesores Robert S. Paton y Jean-Didier Marechal, que me acogieron de forma espectacular en sus grupos de investigación durante las estancias. De ellos aprendí mucho, y sobre todo me trataron extremadamente bien desde un punto de vista personal.

Quiero remarcar también el apoyo que me dio, y me ha seguido dando, mi mentor, el profesor Diego Sampedro, con quien aprendí lo maravillosa que puede ser la química teórica durante la carrera, y quien me introdujo en el mundo de la investigación.

Tengo que hacer una mención aparte a mi compañero de trabajo y gran amigo Pablo Garrido. Hemos colaborado activamente durante el doctorado, descubriendo cosas fascinantes. Él ha sido mi apoyo *in situ*, motivándome en momentos bajos, enseñándome lo que es la electroquímica, y sobretodo dándome tantos buenos momentos fuera del ICIQ, con la salsa y el LOL por bandera.

Acompañándome desde Logroño, no puedo olvidarme de Alejandro García, siempre disponible para desconectar con una buena cerveza, y que además me ha echado una mano con el inglés, pese a lo limitado de tiempo que he estado durante la escritura de la tesis. También a la "cuadrilla" de Tudela, que me ha acompañado en todo momento, en especial a Carlos Izquierdo por su ayuda con la portada.

Dar las gracias también al apoyo que ha mostrado en todo momento mi familia. Mis padres, Félix y Carmela, y mi hermana Andrea, que desde la distancia siempre han estado ahí. Siempre han confiado en mí y en mis decisiones. Además, creo que después de estos tres años, han acabado entendiendo lo que es la química computacional, a excepción del gato de Schrödinger, que aún genera discusión en casa. No puede olvidar a mis abuelas, Conchita y Josefina, que han fallecido durante estos tres años y estoy seguro de que estarían más que orgullosas en este momento.

Finalmente, mis últimas líneas sólo podrían ir dedicadas a ti, Elena. Mi mejor amiga, compañera, amante y soporte. Si me has aguantado estos tres años, siendo tan agotador como he sido, ya no hay escusa para que no lo hagas el resto de nuestra vida.

List of publications

Related with this thesis:

[1] "Redox Non-Innocent Ligand Controls Water Oxidation Overpotential in a New Family of Mononuclear Cu-Based Efficient Catalysts"
Garrido-Barros, P.; Funes-Ardoiz, I.; Drouet, S.; Benet-Buchholz, J.; Maseras, F.; Llobet, A. *J. Am. Chem. Soc.* **2015**, *137*, 6758.

[2] "Cooperative Reductive Elimination: The Missing Piece in the Oxidative-Coupling Mechanistic Puzzle"
Funes-Ardoiz, I.; Maseras, F. *Angew. Chem. Int. Ed.* **2016**, *55*, 2764-2767.

[3] "Single Electron Transfer Steps in Water Oxidation Catalysis. Redefining the Mechanistic Scenario"
Funes-Ardoiz, I.; Garrido-Barros, P.; Llobet, A.; Maseras, F. *ACS Catal.* **2017**, *7*, 1712-1719.

[4] "Science of Synthesis: Water as an Oxygen Source for Oxidation Reactions" (Book Chapter)
Garrido-Barros, P.; Funes-Ardoiz, I.; Farrás, P.; Gimbert-Suriñach, C.; Maseras, F.; Llobet, A. *In Press*

[5] "The elusive mechanism for oxidative coupling in homogeneous catalysis" (Invited perspective)
Funes-Ardoiz, I.; Maseras, F. Manuscript in preparation

Not related with this thesis (at ICIQ):

[6] "DFT Rationalization of the Diverse Outcomes of the Iodine(III)-Mediated Oxidative Amination of Alkenes"

Funes-Ardoiz, I.; Sameera, W. M. C..; Romero, R. M.; Martínez, C.; Souto, J. A.; Sampedro, D.; Muñiz, K.; Maseras, F. *Chem. Eur. J.* **2016**, *22*, 7545-7553.

[7] "Funcionalization of CnH2n+2 Alkanes: Supercritical Carbon Dioxide Enhances the Reactivity towards Primary Carbon-Hydrogen Bonds"
Gava, R.; Olmos, A.; Noverges, B.; Varea, T.; Funes-Ardoiz, I.; Belderrain, T.R.; Caballero, A.; Maseras, F.; Asensio, G.; Pérez, P.J. *ChemCatChem* **2015**, *7*, 3254-3260.

Previous publications (at Unirioja):

[8] "Oxazolone-based photoswitches: Synthesis and properties"
Blanco-Lomas, M.; Funes-Ardoiz, I.; Campos, P.J.; Sampedro, D. *Eur. J. Org. Chem.* **2013**, *29*, 6611-6618.

[9] "Benzylidene-oxazolones as photoswitches: Photochemistry and theoretical calculations"
Funes-Ardoiz, I.; Blanco-Lomas, M.; Campos, P.J.; Sampedro, D. *Tetrahedron* **2013**, *69*, 9766-9771.

[10] "Intermolecular and regioselective access to polysubstituted benzo- and dihydrobenzo[c]azepine derivatives: Modulating the reactivity of group 6 non-heteroatom-stabilized alkynyl carbene complexes"
González, J.; Gómez, A.; Funes-Ardoiz, I.; Santamaría, J.; Sampedro, D. *Chem. Eur. J.* **2014**, *20*, 7061-7068.

[11] "Computational assessment of non-heteroatom-stabilized carbene complexes reactivity: Formation of oxazine derivatives"
Funes-Ardoiz, I.; Sampedro, D. *J. Org. Chem*. **2014**, *79*. 11824-11828.

[12] "On the mechanism of the Shapiro reaction: understanding the regioselectivity"
Funes-Ardoiz, I.; Sampedro, D. *RSC Adv*. **2015**, 5. 37292-37297.

[13] "Understanding the Mechanism of the Divergent Reactivity of Non-Heteroatom-Stabilized Chromium Carbene Complexes with Furfural Imines: Formation of Benzofurans and Azetines"
Funes-Ardoiz, I.; González, J.; Santamaría, J.; Sampedro, D. *J. Org. Chem*. **2016**, *81*, 1565-1570.

[14] "Rational Design and Synthesis of Efficient Sunscreens To Boost the Sola Protection Factor"
Losantos, R.; Funes-Ardoiz, I.; Aguilera, J.; Herrera-Ceballos, E.; García-Iriepa, C.; Campos, P. J.; Sampedro, D. *Angew. Chem. Int. Ed.* **2017**, *56*, 2632-2635.

[15] Patent: "Compuestos fotoprotectores análogos de MMA, procedimiento de síntesis y composición que comprende los mismos".
Inventors: Diego Sampedro, Raúl Losantos, Ignacio Funes.
Patent code: ES-2550374

Contents

Abstract

Redox chemistry is the use of oxidizing or reducing agents to promote complex and energy-demanding chemical reactions by changing the formal oxidation state of at least one element. Any such reaction involves necessarily electron transfer processes, and they often require single electron transfer processes. Single electron transfer chemistry stands apart from the conventional two-electron chemistry (acid-base catalysis, cross-coupling reactions, etc.) and so its reactivity and reaction mechanisms need to be considered differently. Experimental methodologies based on redox chemistry such as artificial photosynthesis and reductive/oxidative couplings have been recently the subject of intense research. The ultimate goal of these experimental methodologies is to open the way to a more sustainable chemistry by improving problematic issues such as the fuel-based energy dependence and the poor atom-economy in chemical synthesis.

As computer power has raised over the decades, so too has the interest in Computational Chemistry, that has already become a field on its own right. Today, we can model a wide range of chemical reactions of practical interest, and we are able to predict the reactivity through the chemical space. In this Thesis, we have applied the power of Computational Chemistry to perform a comprehensive computational study on the mechanism of two key redox catalyzed reactions: water oxidation and oxidative coupling. The formal differences between the two reaction types are an added interest to search for similarities through the analysis of the complex electronic structure of the transition metal intermediates. Because of the size of the systems and the involvement of transition metals, Density Functional Theory (DFT) has been selected as the computational methodology.

The first chapter introduces an overview of redox reactivity including previous computational work on the field. Chapter 2 describes all the theoretical methods used in the reaction mechanistic studies throughout chapters 3 and 4. It also illustrates the development of two new theoretical methodologies, one to apply quasi-harmonic corrections to the free energy in an easy way and the other to calculate standard redox potentials from a simple thermodynamic cycle.

Chapter 3 covers the computational study on two different oxidative coupling reactions: the rhodium/copper catalyzed oxidative coupling of benzoic acid and alkyne and the ruthenium/copper co-catalyzed homocoupling of carbazole under aerobic conditions. The specific effect of the oxidant was clarified in the first case, demonstrating a cooperative effect between rhodium and copper, leading to a new type of elementary step, the cooperative reductive elimination. For the second study, we collaborated with the experimental group of Prof. Patureau, and we analyzed the puzzling integration of ruthenium, copper and molecular dioxygen in the process, and obtained results in excellent agreement with the experimental kinetic measurements. These studies highlight the relevant mechanistic role played by the oxidant, and will help in the experimental design of new more efficient oxidative couplings.

In chapter 4, we analyzed computationally the mechanism of water oxidation for different homogeneous copper catalysts. In collaboration with the experimental group of Prof. Llobet, we first developed a new family of mononuclear copper-based water oxidation catalyst. Latter, we showed that the activation of the catalyst is based on a ligand oxidation, and the oxygen-oxygen bond formation step occurs through an unprecedented mechanism: the Single Electron Transfer-Water Nucleophilic Attack (SET-WNA). This mechanistic knowledge led to the rational design of new ligands that decreased the water oxidation overpotential down to 170 mV. Finally, this chapter culminates in an effort to extend the new reported mechanism into other important copper catalysts, redefining the mechanistic scenario of the oxygen-oxygen bond formation, especially for first-row transition metal catalysts.

Chapter 1

Introduction

1.1 Redox Reactions

A Reduction-Oxidation or redox reaction is a chemical reaction in which the formal oxidation state of at least one element changes during the transformation. Redox reactions can be separated in two half-reactions: oxidation and reduction. The oxidation represents a transformation where one or more electrons are lost, while the reduction consists on the gain of one or more electrons.

The description above includes a lot of chemical transformations but excludes some significant processes (Scheme 1.1). Obviously, those without electron transfers, such as acid-base reactivity, but also those where the final results is redox neutral, regardless of the oxidation state of intermediate species. One significant example of the latter is cross-coupling. In cross-coupling, the catalysts is first oxidized by oxidative addition and later reduced by reductive elimination.

Scheme 1.1 Redox reactivity versus redox-neutral reactivity. Each character represents one general element.

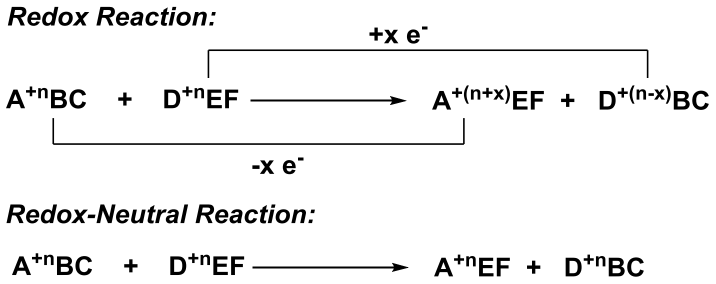

Redox reactions are very common in daily life.[1] They can be found in batteries, inside our cells (cellular respiration), combustion or in plants (photosynthesis). Moreover, in modern chemistry, redox processes have been demonstrated to be essential in a variety of transformations, such as complicated synthetic reactions, radical reactivity of artificial photosynthesis.

Scheme 1.2 Comparison between electrochemical methods *vs* external chemical method to promote redox reactions.

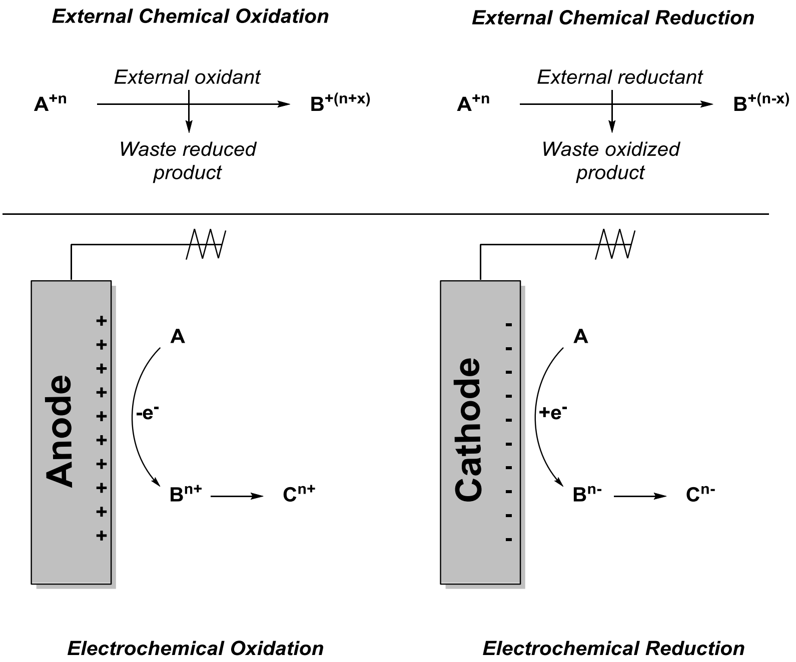

Usually, in a redox transformation, we are only interested on one of the half-reactions, either oxidation or reduction. To keep the neutrality of the electron transfer, the complementary half-reaction is carried out using a sacrificial oxidant or reductant. A general classification is shown in Scheme 1.2. Depending on the methodology, two different approaches can be used: external redox agents or an electrochemical method. In the first one, an external species is added to the system that gives or removes electrons from the reactants. In the second one, an external potential is applied to an electrode in contact with the reacting solution, which can give or remove electrons from the system. In both cases, the catalytic version of redox transformations is usually the best approach to speed up the reactions and to promote more efficient and clean processes.

Connelly and Geiger summarized the advantages and disadvantages of both methods.[2] Electrochemical methods are very useful for mechanistic analysis, as the control of the electric potential provides valuable information on the electron transfer event. However, the presence of an electrolyte restricts the use of nonpolar solvents and can contaminate the product. More critically, preparative applications are limited because the electrode only transfers electrons on the surface, limiting the rate of the reaction. The advantage for chemical redox agents are the easy introduction of nonpolar solvents (facilitating reaction with apolar organic substrates) and the preparation of large-scale reactions. On the other hand, these chemical reagents have a fixed redox potential, which limits the scope of mechanistic studies; and bring waste products resulting from the consumption of the redox agent, which may hinder separation if the structure is similar to the product. An additional problem is that these redox reagents may be noninnocent, especially in inner-sphere electron transfers.

We will discuss in what follows some modern examples of redox processes based on external reagents. Sacrificial redox reagents have been used extensively in the literature to promote a large number of interesting reactions. An exhaustive review of this topic is outside the scope of this introduction and therefore we just present a brief overview of two different types of reactivity that are based on this methodology: the photoredox catalyzed reaction and the oxidative/reductive couplings.

Scheme 1.3 Representative examples of transition metal (left) and organic chromophores that promote photoredox reactions.

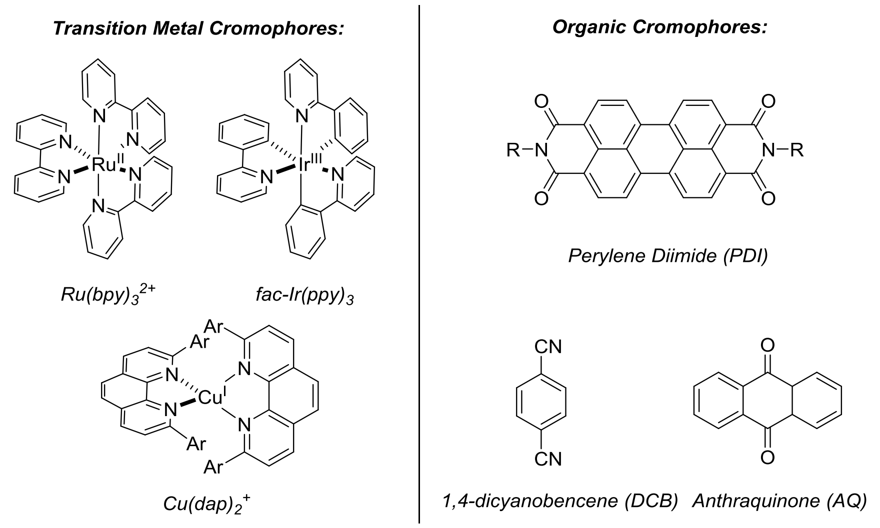

Photoredox catalysis has grown tremendously during the last two decades. These reactions are based on the absorption of light by a photoredox catalyst which becomes prone to single electron transfer events in the excited state. Single electron transfer to/from organic molecules gives then access to novel reactivity that complements the classical two-electron chemistry.[3,4,5,6] The development of photoredox catalyzed organic reactions has been strongly related with the discover of robust and efficient transition metal [7,8] or organic chromophores,[9,10,11] that can trap light to promote photoinduced electron transfers. Two different redox activation cycles can be followed by the photoredox catalyst (Scheme 1.4). If the first electron transfer reduces the substrate, the process is call oxidative quenching because the catalyst is oxidized in this step. In contrast, if the substrate is initially oxidized, the photoredox cycle is named reductive quenching.

Scheme 1.4 Schematic representation of the oxidative (left) and reductive (right) quenching cycles. P represents the photoredox catalysts, A and D stand for acceptor and donor respectively.

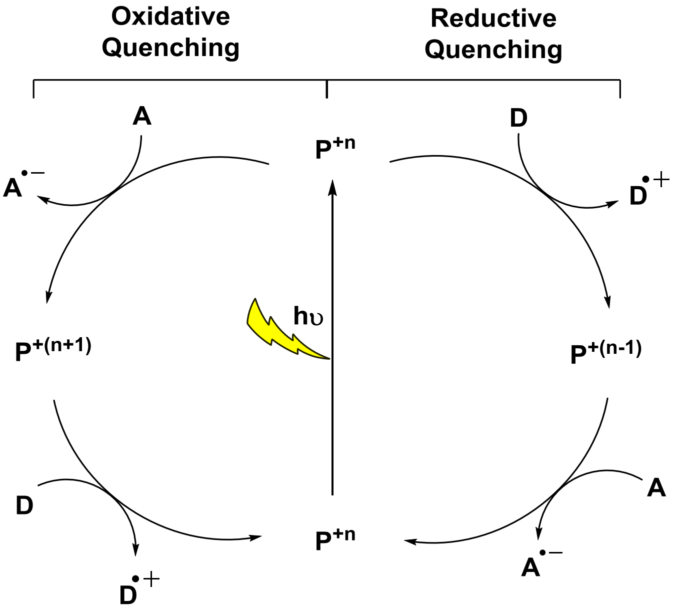

These reactions can be oxidative, reductive or redox neutral, depending on the nature of the transformation. If the substrate is oxidized to produce the product, the process is named oxidative photoredox catalysis. In this reaction, the photoredox catalyst traps one electron from the substrate, and the active catalyst is regenerated using and external sacrificial oxidant, ideally molecular dioxygen.[12,13] The second possibility occurs when the substrate is reduced during the reaction . In this case, an external reductant is needed to regenerate the catalytic cycle.[14,15] Finally, if the substrate is transformed with a nucleophile and an electrophile, the reaction can be redox neutral, and the photoredox catalyst just helps in the activation of the process (the substrate is initially oxidized or reduced, and the reverse electron transfer takes place to regenerate the catalytic cycle). This latter case is not a "redox" reaction according to our definition above.[16,17]

Another synthetically interesting group of redox reactions is constituted by oxidative and reductive couplings. These are formally related to the classic cross-coupling reactions,[18] but introduce a sacrificial oxidant (in oxidative coupling) or reductant (in reductive coupling) to expand the scope and to make the reactions more sustainable .

Scheme 1.5 Several representative examples of oxidative coupling reactions. [2 3,24,25,26]

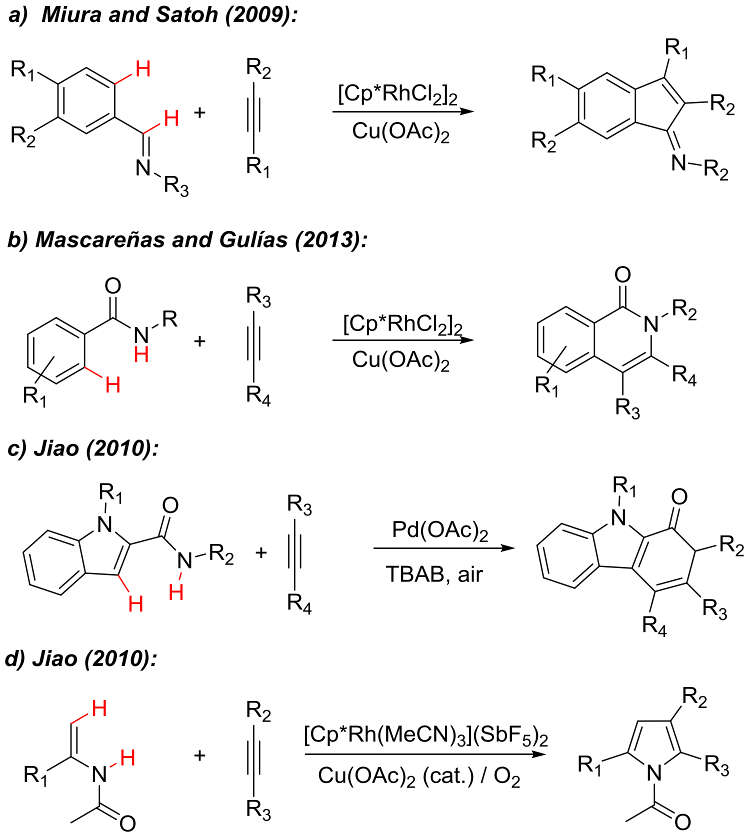

Oxidative coupling is a methodology that allows to build chemical complexity using a transition metal catalyst in a high oxidation state and a sacrificial oxidant.[19] In the reaction, two nucleophiles can be coupled, releasing two electrons to the catalyst, that is regenerated with the external oxidant. Interestingly, these catalysts can frequently activate C-H or other heteroatom-H bonds directly (Scheme 1.5),[20,21,22] avoiding the prefunctionalization of the substrates and therefore, improving the atom economy of the reactions. Metal based sacrificial oxidants are the most common (such as silver(I) or copper(II) acetate).[23,24] Research is in progress on the use molecular oxygen as the final oxidant,[25,26] generating only water as waste product. In these reactions, the role of the oxidant is still obscure and a complete understanding of reaction mechanism is becoming crucial to develop new reactions in a rational way.

Scheme 1.6 Several representative examples of reductive coupling reactions.[29,30,31,32]

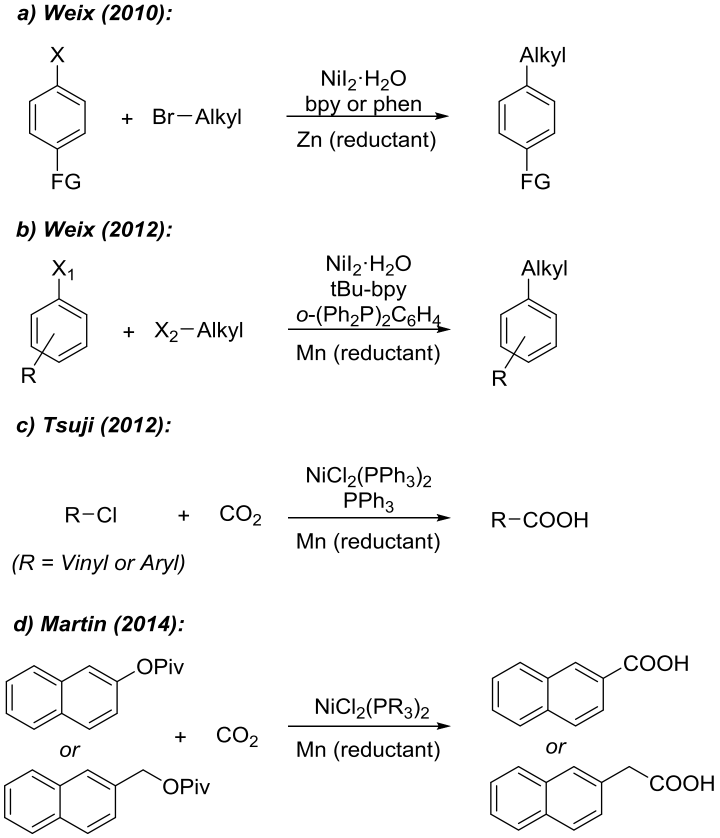

A complementary approach is that of reductive coupling. In this case, the reaction occurs between two electrophiles that accept two electrons from the transition metal catalyst.[27,28] An external reductant is required to regenerate the catalyst (Scheme 1.6), a role that is often played by Mn or Zn powder.[29,30] One of the most interesting applications of these reactions has been the introduction of a cheap and abundant electrophile such as carbon dioxide as feedstock in chemical synthesis.[31,32]

Scheme 1.7 Reduction of electrophiles and oxidation of nucleophiles to promote reverse reactivity.

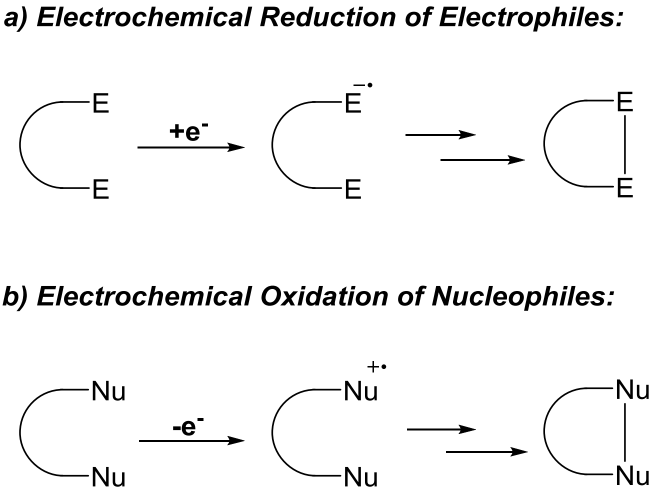
a) Electrochemical Reduction of Electrophiles:

b) Electrochemical Oxidation of Nucleophiles:

We will now briefly review redox reactions based on electrochemistry.[33] This methodology has been extensively used to design new synthetic routes with special properties in organic synthesis.[34,35] Reducing electrophiles or oxidizing nucleophiles opens the door to change the properties of the reactants and induces totally different reactivity than the classical organic routes (Scheme 1.7). In that way, if an electron is injected into an electrophile, it is converted into a nucleophile. The same effect takes place if an electron is removed from a nucleophile.[36] This *umpolung* effect is very useful to discover new synthetic routes for the synthesis of challenging organic natural compounds.

Scheme 1.8 Key anodic oxidation step in the synthesis of dixiamycin B from xiamycin A.

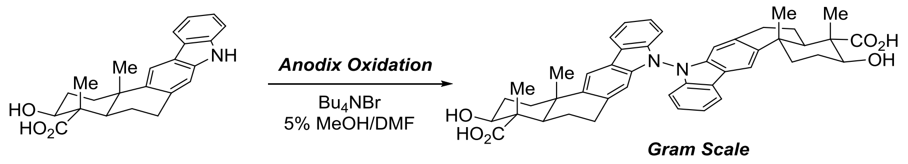

Recently, Baran and co-workers highlighted the importance of organic electrochemistry in natural product synthesis.[37] They mentioned that exploring electrochemical transformations is usually difficult due to the scarcity of commercially available equipments. These reactions are environmentally friendly and can tolerate different functional groups. For this reason, they are appropriated for late stage functionalization of complex compounds. For example, an anodic oxidation was found to be the key step in the synthesis of dixiamycin B (Scheme 1.8).[38] In addition, electrochemical methodology was also used to promote allylic C-H oxidation selectively and in 100 gram scale, demonstrating that electrochemistry can be useful in preparative applications.[39]

Electrochemistry has also played a key role in the development of artificial photosynthesis, which is based on the catalytic production of solar fuels.[40] This process is based on the water splitting reaction, producing hydrogen and oxygen using sunlight as the energy input. Classically, this reaction has been divided in the two half reactions, the water oxidation and the proton reduction, being the first one the bottleneck of the process. The water oxidation reaction is a four electron process, involving the cleavage of four O-H bonds and the formation of an O-O bond. For this reason, it is both thermodynamically and kinetically challenging.[41] During the last years, the development of water oxidation catalysts (homogeneous and heterogeneous) has been a hot topic in chemistry and electrochemistry has been used to follow the reaction, to analyze the mechanism and to construct electrochemical cells.[42]

Scheme 1.9 A representative examples of homogeneous water oxidation catalysts based on ruthenium and iridium.[43,44,45,46,47]

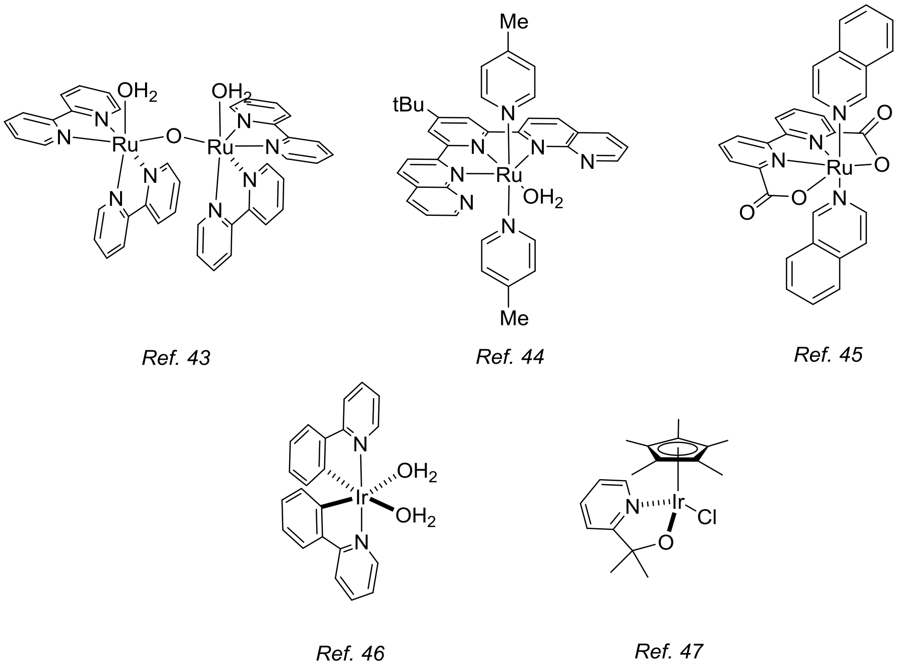

Regarding the homogeneous version of the reaction, which is the one of interest in this thesis, several advances have been done since the first molecular water oxidation catalyst reported in 1982.[43] This approximation to the water oxidation reaction provides a wide range of chemical techniques (spectroscopy, analytical electrochemistry, etc) to understand the most relevant factors that affect the reactivity, such as the structure, the electronic properties of the ligands or the coordination number. A large number of molecular catalysts have been reported and some representative examples are shown in Scheme 1.9. The major problem is that they are mainly based on expensive and highly toxic precious metals such as ruthenium and iridium.[48]

In order to overcome these drawbacks, cheaper and more abundant first row transition metals have started to be proposed for this reaction.

Although only few examples have been reported until now, this is a promising field that should develop rapidly in the near future.

To summarize, redox reactions are, and will be, essential for the development of modern chemistry. This thesis will be focused on the study of two of the processes discussed above, the oxidative coupling and the water oxidation reactions (chapters 3 and 4, respectively). A larger and more specific introduction of these topics can be found in the first section of each chapter, providing a more specific review of the state of the art of these processes.

1.2 Computational Perspective on Homogeneous Redox-Catalyzed Reactions

Understanding reaction mechanisms is essential to develop chemistry in a more rational way. In this context, computational chemistry has been, and will be, an important tool to increase the knowledge of chemical processes. The development of new theories, such as Density Functional Theory, in conjunction with the increase of computer power, has largely expanded the range of application for computational chemistry. Quantum chemistry provides nowadays useful information about intermediates that cannot be characterized experimentally, and transition states, which can explain the key factors that affect the efficiency of a reaction. It is especially appropriate for the study of complex multistep catalytic processes.

During the last decades, large efforts have been apply to calculate mechanisms for two electron chemistry, such as cross-coupling or hydrogenation reactions.[49] However, theoretical studies of redox processes, which usually involve single electron transfer steps, are still scarcely explored. We summarize here some relevant theoretical examples of redox chemistry. In addition, an extended version of the previous theoretical studies on specific topics can be found in each chapter of this thesis.

Regarding the photoredox catalyzed reactions, our group have reported recently some relevant studies on the computational characterization of the mechanisms.[50,51] In the case of oxidative and reductive couplings, there are some previous theoretical studies, but in most of the cases, they are specific examples that cannot be generalized. Key questions, such as the role of the oxidant or the reductant during the processes, have been seldom addressed. Our group recently reported one example that demonstrates the role of the oxygen in the Glaser-Hay reaction.[52] In addition, radical reactions into nonheme high-valent iron-oxo or metal-oxo moieties have been extensively studied computationally in the literature.[53]

On the other hand, the calculation of standard redox potential of species in solution has been successfully addressed.[54,55]. However, when a solid species is involved, the calculation of standard redox potential is still a challenge and only few attempts have been done with an associated error that limits the applicability of these methods to understand reaction mechanisms in which one solid is involved, such as in reductive couplings.[56]

Finally, we have to mention that in the case of water oxidation reaction, the field is much more mature.[57] The basis for the oxygen-oxygen bond formation mechanism has been well-established in ruthenium and iridium chemistry. Studies are however still lacking in first-row transition metal water oxidation catalysis. They can help in the rational design of new catalysts for this reaction.

Thus, we consider that the application of computational chemistry to homogeneous redox catalysis is totally needed at this point and it would help in the development of more efficient processes in the future.

1.3 Objectives

The main goal of this thesis is to improve the understanding of redox catalyzed reactions in solution. We intend to reach this goal through the Density Functional Theory (DFT) study of two different types of processes: oxidative coupling and water oxidation reactions. The formal differences between both reactions will help to better characterize the underlying similarities between these processes based on electron transfers. We expect that the improved understanding of the reaction mechanisms will assist in the rational design of new reactions in the field.

The specific objectives of each chapter are discussed separately below:

- **Chapter 2**: We analyze the available tools for the description of redox catalyzed reactions in solution, and we propose the tuning of some methods.

- **Chapter 3**: We intend to understand the role of the oxidant in oxidative couplings through the characterization of the full catalytic cycle for two or these processes. The first one is the rhodium-catalyzed coupling of benzoic acid and alkynes with copper(II) as final oxidant. The second one is a ruthenium- and copper- catalyzed carbazole homocoupling using dioxygen as final oxidant. In the second process we are collaborating with the experimental group of Prof. Patureau (University of Kaiserlautern).

- **Chapter 4**: We intend to improve our understanding of the oxygen-oxygen bond formation event in water oxidation by transition metal complexes. We start by analyzing the behavior of new copper complexes in collaboration with the experimental group of Prof. Llobet (ICIQ). We later move towards the generation of a complete mechanistic picture of water oxidation reaction, including the first-row catalysts.

1.4 References

[1] Brown, T. L.; Lemay, H. E.; Bursten, B. E.; Murphy, C. J.; Woodward, P. M. *Chemistry The Central Science,* 13th Edition, Pearson: Boston, USA, 2015. Pages 138-146.

[2] Connelly, N. G.; Geiger, W. E. *Chem. Rev.* **1996**, *96*, 877-910.

[3] Romero, N. A.; Nicewicz, D. A. *Chem. Rev.* **2016**, *116*, 10075-10166.

[4] Prier, C. K.; Rankik, D. A.; MacMillan, D. W. C. *Chem. Rev.* **2013**, *113*, 5322-5303.

[5] Xuan, J.; Xiao, W.-J. *Angew. Chem. Int. Ed.* **2012**, *51*, 3828-3838.

[6] Levin, M.D.; Kim, S.; Toste, F. D. *ACS Cent. Sci.* **2016**, *2*, 293-301.

[7] Balzani, V.; Juris, A.; Venturi, M. Campagna, S.; Serroni, S. *Chem. Rev.* **1996**, *96*, 759-834.

[8] Balzani, V.; Campagna, S. *Topics in Curren Chemistry: Photochemistry and Photophysics of Coordination Compounds II*, Vol. 287, Springer-Verlag, Berlin Heidelberg, Germany, 2007.

[9] Fukuzumi, S.; Ohkubo, K. *Org. Biomol. Chem.* **2014**, *12*, 6059-6071.

[10] Kainz, Q.M.; Matier, C.D.; Batoszewicz, A.; Zultanski, S.L.; Peters, J.C.; Fu, G.C. *Science*, **2016**, *351*, 681-684.

[11] Discekici, E.H.; Treat, N.J.; Poelma, S.O.; Mattson, K.M.; Hudson, Z.M.; Luo, Y.; Hawker, C.J.; Read de Alaniz, J. *Chem. Commun.* **2015**, *51*, 11705-11708.

[12] Zou, Y.-Q.; Chem, J.-R.; Liu, X.-P.; Lu, L.-Q.; Davis, R. L.; Jorgensen, K. A.; Xizo, W.-J. *Angew. Chem. Int. Ed.* **2012**, *51*, 784-788.

[13] Tucker, J. W.; Narayanam, J. M. R.; Shah, P. S.; Stephenson, C. R. J. *Chem. Commun.* **2011**, *47*, 5040-5042.

[14] Maji, T.; Karmakar, A.; Reiser, O. *J. Org. Chem.* **2011**, *76*, 736-739.

[15] Nakajima, M.; Fava, E.; Loescher, S.; Jiang, Z.; Rueping, M. *Angew. Chem. Int. Ed.* **2015**, *54*, 8828-8832.

[16] Neumann, M.; Füldner, S.; König, B.; Zeitler, K.; *Angew. Chem. Int. Ed.* **2011**, *50*, 951-954.

[17] Shih, H.-W.; Vander Wal, M. N.; Grange, R. L.; MacMillan, D. W. C. *J. Am. Chem. Soc.* **2010**, *132*, 13600-13603.

[18] Nishihara, Y. *Applied Cross-Coupling Reactions*, 1st Edition, Springer-Verlag: Berlin, Germany, 2013.

[19] Lei, A.; Shi, W.; Liu, C.; Liu. W.; Zhang, H.; He, C. *Oxidative Cross-Coupling Reactions*, 1st Edition; Wiley-VCH: Weinheim, Germany, 2017.

[20] Le Bras, J.; Muzart, J. *Chem. Rev.* **2011**, *111*, 1170-1214.

[21] Wendlandt, A. E.; Suess, A. M.; Stahl, S. S. *Angew. Chem. Int. Ed.* **2011**, *50*, 11062-11087.

[22] Bergman, R. G. *Nature* **2007**, *446*, 391-393.

[23] Fukutani, T.; Umeda, N.; Hirano, K.; Satoh, T.; Miura, M. *Chem. Commun.* **2009**, 5141-5143.

[24] Quiñones, N.; Seoane, A.; Gacía-Fandiño, R.; Mascareñas, J. L.; Gulías, M. *Chem. Sci.* **2013**, *4*, 2874-2879.

[25] Shi, Z.; Cui, Y.; Jiao, N. *Org. Lett.* **2010***,* *12*, 2908-2911.

[26] Stuart, D. R.; Alsabeh, P.; Kuhn, M.; Fagnou, K. *J. Am. Chem. Soc.* **2010**, *132*, 18326-18339.

[27] Moragas, T.; Correa, A.; Martin, R. *Chem. Eur. J.* **2014**, *20*, 8242-8258.

[28] Nguyen, K. D.; Park, B. Y.; Luong, T.; Sato, H.; Garza, V. J.; Krische, M. J. *Science* **2016**, *354*, 300(aah5133:1-5)

[29] Everson, D. A.; Shrestha, R.; Weix, D. J. *J. Am. Chem. Soc.* **2010**, *132*, 920-921.

[30] Everson, D. A.; Jones, B. A.; Weix, D. J. *J. Am. Chem. Soc.* **2012**, *134*, 6146-6159.

[31] Correa, A.; Leon, T.; Martin, R. *J. Am. Chem. Soc.* **2014**, *136*, 1062-1069.

[32] Fujihara, T.; Nogi, K.; Xu, T.; Terao, J.; Tsuji, Y. *J. Am. Chem. Soc.* **2012**, *134*, 9106-9109.

[33] Savéant, J.-M. *Chem. Rev.* **2008**, *108*, 2348-2378.

[34] Yoshida, J.; Kataoka, K.; Horcajada, R.; Nagaki, A. *Chem. Rev.* **2008**, *108*, 2265-2299.

[35] Grimshaw, J. *Electrochemical Reactions and Mechanisms in Organic Chemistry*, 1st Edition, Elsevier Science B. V.: Amsterdam, The Netherlands, 2000.

[36] Little, R. D.; Moeller, K. D. *Interface* **2002**, *Winter*, 36-42.

[37] Horn, E. J.; Rosen, B. R.; Baran, P. S. *ACS Cent. Sci.* **2016**, *2*, 302-308.

[38] Rosen, B. R.; Werner, E. W.; O'Brien, A. G.; Baran, P. S. *J. Am. Chem. Soc.* **2014**, *136*, 5571-5574.

[39] Horn, E. J.; Rosen, B. R.; Chem. Y.; Tang, J.; Chen, K.; Eastgate, M. D.; Baran, P. S. *Nature*, **2016**, *533*, 77-81.

[40] Gust, D.; Moore, T. A.; Moore, A. L. *Acc. Chem. Res.* **2009**, *42*, 1890-1898.

[41] Sala, X.; Maji, S.; Bofill, R.; Garcia-Anton, J.; Escriche, L.; Llobet, A. *Acc. Chem. Res.* **2014**, *47*, 504-516.

[42] Dau, H.; Limberg, C.; Reier, T.; Risch, M.; Roggan, S.; Strasser, P. *ChemCatChem* **2010**, *2*, 724-761.

[43] Gersten, S. W.; Samuels, G. J.; Meyer, T. J. *J. Am. Chem. Soc.* **1982**, *104*, 4029-4030.

[44] Zong, R.; Thummel, R. P. *J. Am. Chem. Soc.* **2005**, *127*, 12802-12803.

[45] Duan, L.; Bozoglian, F.; Mandal, S.; Stewart, B.; Privalov, T.; Llobet, A.; Sun, L. *Nat. Chem.* **2012**, *4*, 418-423.

[46] McDaniel, N. D.; Coughlin, F. J.; Tinker, L. L.; Bernhard, S. *J. Am. Chem. Soc.* **2008**, *130*, 210-217.

[47] Parent, A. R.; Brewster, T. P.; De Wolf, W.; Crabtree, R. H.; Brudvig, G. W. *Inorg. Chem.* **2012**, *51*, 6147-6152.

[48] Karkas, M. D.; Verho, O.; Johnston, E. V.; Akermark, B. *Chem. Rev.* **2014**, *114*, 11863-12001.

[49] Sperger, T.; Sanhueza, I. A.; Kalvet, I.; Schoenebeck, F. *Chem. Rev.* **2015**, *115*, 9532-9586.

[50] Fernández-Alvarez, V. M.; Nappi, M.; Melchiorre, P.; Maseras, F. *Org. Lett.* **2015**, *17*, 2676-2679.

[51] Dell'Amico, L.; Fernández-Alvarez, V. M.; Maseras, F.; Melchiorre, P. *Angew. Chem. Int. Ed.* **2017**, *56*, 3304-3308.

[52] Jover, J.; Spuhler, P.; Zhao, L.; McArdle, C.; Maseras, F. *Catal. Sci. Technol.* **2014**, *4*, 4200-4209.

[53] Ye, S.; Geng, C.-Y.; Shaik, S.; Neese, F. *Phys. Chem. Chem. Phys.* **2013**, *15*, 8017-8030.

[54] Marenich, A. V.; Ho, J.; Coote, M. L.; Cramer, C. J.; Truhlar, D. G. *Phys. Chem. Chem. Phys.* **2014**, *16*, 15068-15106.

[55] Baik M. –H. Friesner, R. A. *J Phys. Chem. A* **2002**, *106*, 7407-7412.

[56] Shimodaira, Y.; Miura, T.; Kudo, A.; Kobayashi, H. *J. Chem. Theory. Comput.* **2007**, *3*, 789-795.

[57] Balcells, D. *Adv. Organomet. Chem.* **2016**, *65*, 115-173.

Chapter 2

Theoretical Background

2.1 Computational Chemistry

The development of computers during the last century has enabled us to carry out large amount of mathematical operations in a short time. This, in combination with the advancement of theoretical chemistry methodologies, has been crucial for the rapid evolution of computational chemistry. Nowadays, even with a personal computer, it is possible to effectively simulate the properties of a chemical system. Moreover, the parallelization of the computer work on supercomputers warrants the rapid screening of molecular systems and the applicability of accurate theoretical models such as quantum chemistry methods.

We can define computational chemistry as the branch of chemistry responsible for modeling, explaining and predicting properties of a chemical structure or a chemical reaction with the assistance of computers. The combination of computational and experimental chemistry allows the development of new reactions in a rational way. In addition, theoretical chemistry has evolved also considerably, covering a wide variety of situations, from little systems with very high accuracy, where quantum chemistry is essential to describe properly the reactivity, to large systems, such as proteins, in which molecular mechanics or a multi-scale model based on quantum mechanics and molecular mechanics can produce good models to understand molecular interactions or even reactivity.

Scheme 2.1 Schematic representation of the development of predictive models using theoretical, experimental and computational chemistry.

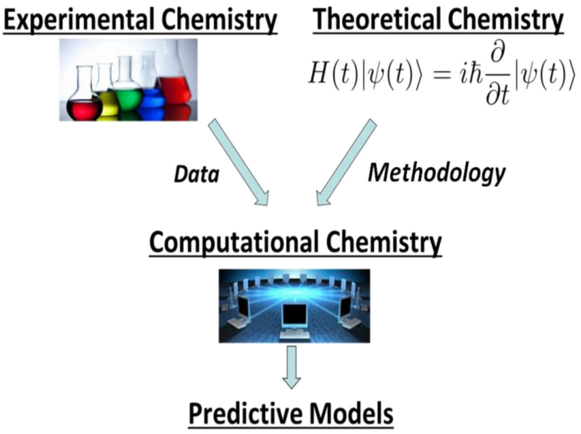

The workflow of computational chemistry is summarized in Scheme 2.1. Using the appropriate methodology developed by theoretical chemistry and the valuable data obtained experimentally, computational chemistry can interpret the results and construct models. If the models are accurate enough, they can be used to predict new properties or reactions, facilitating the discovery of new processes in a rational manner. This interdisciplinary approach is essential for modern chemistry.

In this Thesis we will focus on the transition metal catalyzed-redox chemistry. The size of the system (up to 100-150 atoms) is small enough to apply very accurate quantum chemistry methods, especially those based on density functional theory (DFT). We will cover a variety of redox reactions, based on two different topics: oxidative coupling and water oxidation catalytic reactions. Our methodology must provide a sufficiently clear picture of both reactions to generate predictions over the system.

2.2 Theoretical Methods

Density functional theory for electronic structure calculations

Theoretical chemistry has produced many methods to calculate chemical reactions. In the study of reaction mechanisms, free energies are calculated to obtain the thermodynamics (minimum calculations) and kinetics (transition state calculations). As the chemical reactivity is strongly related with electronic structure, only the methods that explicitly consider the electrons are useful to compute reaction pathways. In this context, quantum chemistry is the most accurate theory. Several approaches have been developed to make the methodology applicable to systems of practical interest.

Classically, quantum chemistry has been based on the multielectronic wavefunction approach. This wavefunction depends on 3N variables (N being the number of electrons of a specific system) plus N spin-variables and must satisfy the Schrödinger equation. The resolution of the Schrodinger equation is very complicated from a mathematical point of view. For this reason, these methodologies rely on an approximate wavefunction and try to improve it in a systematic way. Unfortunately, the computational cost of these methods (usually named Hartree-Fock-derived methods) is often too high to analyze real chemical reactions in detail and they are only applied in model systems. This computational cost may be defined as the time required by the computer to complete a calculation.

More recently, a different approach to quantum chemistry has been developed as an alternative and more efficient way to study chemical reactivity: Density Functional Theory (DFT). The main idea behind DFT is that the energy (or other properties) of a system can be expressed as a functional of the electron density ρ(r) (Eq 2.1). This electron density is defined as the probability of finding one electron in an infinitesimal volume. This function is represented by only three spatial coordinates, and the integration over all the space yields the number of electrons of the system.

$$E = E[\rho(\vec{r})] \qquad \text{(Eq. 2.1)}$$

This change of paradigm increases the efficiency of the method dramatically and allows the calculation of larger systems (up to 100-200 atoms) at a very accurate level. Thus, we will use this theory all along the Thesis. Several books explain in detail the mathematical derivation of DFT equations [1] but this is out of the scope of this chapter and only a brief description of the main features will be presented here.

The basis of the DFT theory was born in 1964 with the seminal paper by Hohenberg and Kohn.[2] They reported the two theorems that provided the theoretical background for the DFT. The first one states that "the external potential $V_{ext}(\vec{r})$ is a unique functional of $\rho(\vec{r})$; since, in turn $V_{ext}(\vec{r})$ fixes $\widehat{H}$ we see that the full many particle ground state is a unique functional of $\rho(\vec{r})$". This theorem demonstrated that the electron density of a system determines the Hamiltonian operator uniquely and therefore all the properties of the system. The second one states that "$F_{HK}[\rho]$, the functional that delivers the ground state energy of the system, delivers the lowest energy if and only if the input density is the true ground state density". In other words, it is a reformulation of the variational principle because for a density that satisfies the boundary conditions, the functional gives the energy that represents an upper bound to the exact energy.

Therefore, while post-HF methods are based on the improvement of the wavefunction, DFT looks for the development of an accurate functional, since the exact functional for a general system is yet unknown. The ground state energy functional can be expressed as a sum of independent terms (Eq 2.2):

$$E[\rho_0] = T_S[\rho_0] + J[\rho_0] + E_{Ne}[\rho_0] + E_{XC}[\rho_0] \qquad \text{(Eq. 2.2)}$$

where $T_S[\rho_0]$ is the kinetic energy of non-interacting electrons, $J[\rho_0]$ is the classical Coloumb electron-electron repulsion, $E_{Ne}[\rho_0]$ is the nucleus-electron interaction and $E_{XC}[\rho_0]$ is the unknown exchange-correlation interaction, which includes the quantum mechanical affected potential energy terms (the self-interaction correction, the exchange and correlation of electrons) and the kinetic energy affected by the electron-electron interaction. This part of the functional is approximated in a variety of approaches, producing the "soup of functionals" available in the literature. The idea of regrouping the non-interacting term and building the density from a set of orbitals was put forward by Kohn and Sham in 1965, and it allowed to use the DFT for doing calculations of real systems.[3] With this approximation the self-consistent equations can be solved similarly to the Hartree-Fock method, using the "Kohn-Sham" orbitals.

As we mentioned above, the approximation to the exchange-correlation functional has produced a variety of density functionals. Usually, the functionals are also divided in two different parts, the exchange part and the correlation part (Eq 2.3):

$$E_{XC}[\rho_0] = E_C[\rho_0] + E_X[\rho_0] \qquad \text{(Eq. 2.3)}$$

In principle, both parts can be solved independently and depending on the approximation used to construct the functionals, we can classify the functionals into different groups, the Local Density Approximation functionals (LDA), the Generalized Gradient Approximation functionals (GGA), the Hybrid functionals and the Meta-GGA functionals. Additionally, other exotic functionals, called hyper-GGA and non-local functionals which are in principle the most accurate from the theoretical perspective, will not be discussed here as their applicability is still far from reality.

The simplest approach to the exchange-correlation functional is the local density approximation (LDA). It is based on the uniform electron gas model, which assumes that connection between energy and electron density is similar to the one that exists on such simple system. The exchange part is derived from the Thomas-Fermi-Dirac method [4,5,6] and the correlation part from highly accurate simulations of the uniform electron gas, such as in the VWN [7] or the PW92 correlation functionals.[8] However, these functionals, which give an accuracy below the HF method, are not appropriate for transition-metal catalyzed reaction mechanisms.

The next generation of functionals was based on the Generalized Gradient Approximation (GGA). This construction takes into account the non-homogeneity of the electron density, considering the gradient of this function both in the exchange and in the correlation functionals. There are two philosophies for the GGA exchange functional development. The first one is based on parameters derived from experimental or high-accurate quantum calculated data, such as the famous B correlation functional by Becke.[9] In contrast, the second one is based on quantum mechanical principles, as it happens in functionals by Perdew such as the PBE.[10,11] The correlation functionals are based on analytical equations, some important examples are the P86 [12] or the LYP functionals.[13] Quantum chemistry program packages usually allow the combination of any exchange functional with any correlation functionals, although some combinations are normally used together such as BLYP or BP86.

Eventually, the inclusion of both the gradient and the laplacian (the second derivative) of the electron density was proposed, leading to the meta-GGA functionals. One of the most used of this family is the M06-L functional,[16] which also includes parameterization as we will discuss on the subsection dealing with dispersion interactions.

A last improvement/modification worth mentioning in "traditional DFT" was the incorporation of some of the Hartree-Fock exact exchange into the DFT exchange functional. This produces the hybrid functionals. Probably, the most famous functional of this type is the B3LYP,[14,15] which uses the previously commented LYP correlation functional and the B3 exchange functional, which takes the name from its three different parameters. One of them is the amount of HF exchange (20%), and the other two represents the weight of LDA correlation and exchange functionals and GGA correlation (LYP) and exchange (B88) functionals. Exact exchange is also included in meta-GGA functionals, such as M06 (27% of HF exchange) and M06-2X (57 % of HF exchange).[17]

In this thesis, we will carry out the calculation with GGA, hybrid and meta-GGA functionals, doing benchmarking studies to ensure the validity of the method.

Dispersion interactions

Dispersion forces are non-covalent attractive interactions between two fragments at long-range distances based on quantum-induced instantaneous polarization. "Traditional DFT" calculations usually failed in the evaluation of these mid- or long-range interactions and two different approaches have been developed to accomplish the evaluation of these forces. The first one is based on the parameterization of the functional, implicitly including some of the dispersion interactions. The most representative example of this approach is the M06 family of functionals developed by Truhlar and co-workers.[16,17] However this overparameterization has been demonstrated to affect negatively the electron density description in some cases.[18]

The other alternative, which has been used along this Thesis, is based on the inclusion of a dispersion term based on the Becke-Johnson equation.[19] This function is controlled by a damping function, which only acts for mid- and long-range interactions (Eq 2.4).

$$E_{Disp} = -\sum i\, j\, f_{damping} \cdot \left(\frac{C_{6,ij}}{R_{ij}^{6}} + \frac{C_{8,ij}}{R_{ij}^{8}} + \ \dots \right) \qquad \text{(Eq 2.4)}$$

The most common equations applied to DFT calculations were developed by Grimme.[20,21] Depending on the number of parameters, he defined the D2 dispersion function (based only on C_6 parameters) with two parameters for the damping function (S_6, which depends on the functional and SR_6, which is fixed) and the D3 dispersion function (based on C_6 and C_8) which used four parameters (S_6, SR_6 and S_8 which depends on the functional and SR_8 fixed with a value of 1.0 and usually ignored).

Implicit solvation model

Chemical reactivity is strongly affected by the medium. The election of the proper solvent is always an essential feature in the optimization of reaction conditions, due to the stabilization (or destabilization) of intermediates and transition state along the reaction pathway. The polarity of the solvents affects indeed the solubility of the reactants, but also the mechanism of the reaction. For example, if there were a separation of charges in a transition state, a polar solvent would stabilize it and lower the barrier. For this reason, the modelling of the solvent is crucial to obtain accurate results.

The more intuitive idea to overcome the solvent influence in a specific mechanism is to include solvent molecules explicitly. However, this "explicit" solvent model is not so efficient because the number of atoms in the system increases dramatically and thus the computational cost becomes unaffordable. In addition, the optimization of an intermediate or a transition state with many explicit solvent molecules arises the problem of different spatial configurations or the question about how many solvent molecules are needed. Nevertheless, when a solvent molecule can be involved directly in the mechanism, the inclusion of explicit solvent is mandatory. We will consider this approach in the section 4.3.

Conveniently, these drawbacks may be avoided by considering the solvent as a continuous medium, which represents a dielectric environment. This approach is called "implicit" solvation model and the computational cost associated with solvent calculations is easily affordable. To compute energies in solution, the usual method is based on an iterative process, in which the solvent continuum medium is affected by a molecule and *vice versa*. The process is introduced in the normal convergence of the molecular orbitals, resulting in the Self-Consistent Reaction Field (SCRF) approach. The mathematical treatment of this methodology is based on non-homogeneous Poison equation for electrostatics, which is solved by the Integral-Equation-Formalism (IEF-PCM).[22]

There are several continuum solvation methods. We will use the Solvation Model based on Density (SMD) methodology along the Thesis. This method is a universal solvation method in which few descriptors are needed (dielectric constant, refractive index, bulk surface tension and acidity and basicity parameters). It is convenient to estimate free energies in solution. It separates the solution free energy in two terms, the bulk electrostatic contribution and the cavity dispersion solvent structure. The first one is based on the traditional Polarized Continuum Model (PCM) methodology while the second one considers the short-range effects of the solvent and the molecule.[23]

Open-shell systems in DFT

Redox reactions are based on electron transfers, for this reason the presence of unpaired electrons in different species and intermediates during the reaction pathways is very common. DFT methods are not multiconfigurational (only one Slater determinant is used) and this is why these electronic states, with unpaired number of electrons or unpaired electrons (multiplets) with opposite spin (open-shell electronic structures) are not well described. Proper description of multiconfigurational sates is still one of the most important challenges on quantum chemistry. The basis of the theory that is applied in the broken-symmetry approach can be consulted in the comprehensive tutorial review of Jacob and Reiher, which describes in detail the advantages (and disadvantages) of both the restricted and the unrestricted KS approaches.[24]

Until the problem is solved from a theoretical point of view, it is still possible to obtain accurate energies of these systems using the unrestricted Kohn-Sham formalism (UKS). Unrestricted means in this context that the α orbitals are not forced to be identical to the β orbitals. This produces a formally incorrect spin description of the system, as the resulting Kohn-Sham orbitals are not eigenfunctions of the spin operator. But it gives a reasonable approach to the energy of open-shell systems.

The unrestricted version of the orbitals does not constrain the spin symmetry and therefore, the solution can give a breaking symmetry spin state, usually contaminated with higher multiplicity spin states. This flexibility provides a much better energetic description than the restricted approach, which is poor in multiconfigurational electronic structures.

Selectivity calculation

The assembly of specific products is usually the goal of any chemical reaction. This is strongly related with the selectivity along the reaction pathway. Consequently, it is fundamental to understand where the selectivity comes from and how the selectivity of the process works. Computational chemistry can help in those questions, assisting in the development of more rational processes. In a complex reaction, such as the oxidative coupling, analyzing the factors controlling the chemo- or the regioselectivity is not always trivial, but from the calculations we can estimate the different barriers associated with the different reaction pathways.

Normally, a complex reaction consists on different consecutive steps but only some of them determine the selectivity, *i.e.* the regioselectivity determining step or the chemoselectivity determining step.[25] If different pathways have similar activation barriers and the reaction step is irreversible, the reaction outcome will follow a Boltzmann distribution of the energy barriers. The difference between the free energy barrier of selective transition states can be used to calculate the theoretical ratio of the reaction products using the following equation (Eq 2.5):

$$Product\ ratio = \frac{e^{-\Delta G_1^{act}/RT}}{e^{-\Delta G_2^{act}/RT}} \qquad \text{(Eq. 2.5)}$$

where ΔG_1^{act} represents the activation barrier of the pathway 1 and ΔG_2^{act} the activation free energy barrier of the pathway 2.

Reference state for free energy calculation

The computation of accurate free energies is mandatory when we compare experimental data with theoretical information. The reactions that we are going to study are carried out in solution and so, to compare thermodynamic and kinetic parameters, the reference state should be 1 M. However, the free energy correction that we compute directly from the quantum chemistry program package, in our case the Gaussian09, is calculated in ideal gas conditions. This corresponds with a concentration of 1/24.5 M (according to the Ideal Gas Law). As the translational entropy is affected by the volume, we should correct this term. In order to convert this free energy to the solution standard state 1 M, we must apply the conversion term of 1.89 kcal/mol. This factor can be easily calculated from the following equation (Eq. 2.6):

$$\Delta G_{1M} = -RT \ln\left(\frac{{}^{1}/_{24.5}\mathrm{M}}{1\mathrm{M}}\right) \qquad \text{(Eq. 2.6)}$$

where R is the ideal gas constant and T is the temperature. The demonstration of this equation is straightforward and can be found for instance in the computational chemistry book by Jensen.[26] This correction term does not have any effect if the number of molecules in a reaction step is the same for both the reactants and the products. Thus, it should be only applied when this number change using the formula variation number · 1.89 kcal/mol.

2.3 Theory Development

Goodvibes free code

The calculation of free energies in solution is essential to correlate the computational results with the experiments (selectivity, reaction rate, etc.). However, the accuracy of free energy correction is not always good enough and normally, this correction needs to be calculated using a “black box”, where different factors are not clear. One of the most used programs for *ab initio* calculations is Gaussian09.[27] In this program, the free energy correction is calculated using the ideal gas approximation for all the partition functions and a full tutorial of the different parameters used in the calculation can be found in the Gaussian web site.[28]

A serious problem for the practical application of the computational results is related with the presence of low-lying frequencies. In large systems, the existence of these small frequencies is very common, and must be taken into account to properly model the free energy. The vibrational entropy partition function is based on the harmonic oscillator and when vibrational frequencies are below to 50-100 cm^{-1}, this approximation leads to large correction values. The problem is those large values are wrong because the harmonic oscillator approximation cannot be applied properly in this low frequencies. To solve this mathematical problem, several corrections have been proposed in the literature.

Cramer and Truhlar proposed a quasi-harmonic approximation in which low-lying frequencies (below 100 cm^{-1}) are raised to the cut-off value. This conversion corrects the breakdown of the harmonic oscillator model for the lowest frequencies.[29] Another approximation was reported by Grimme in 2012. In this case, the low-lying frequency vibrational entropy is calculated using the rotational entropy, based on the free-rotor moment of inertia.[30] To avoid discontinuities between two models, the Head-Gordon damping function was used to interpolate between the two models, the rotational for low frequencies and the harmonic oscillator for large frequencies.[31] In both methods, the cut-off limit was placed on 100 cm^{-1}, which is about 1/2kT (k is the Boltzmann constant and T the temperature) at room temperature.

Additionally, the vibrations obtained from *ab initio* calculations are usually overestimated and depending on the method, different scaling factors can be used to obtain more accurate results. A list of this scaling correction factors can be found in the Truhlar group database and was reported in the literature.[32]

The application of those approximations in Gaussian09 calculations is not obvious and home-made scripts have to be programmed since there are not included in the traditional software. For this reason, we envisioned to open the "black box" of Gaussian thermochemistry calculations in a Python free code, the Goodvibes program.

I developed the program with Prof. Robert S. Paton (University of Oxford) during my international internship in his group. Fortunately enough, the program was successfully built and we included several features to help the computational chemistry community to apply quasi-harmonic correction for the free energy. All (electronic, translational, rotational and vibrational) frequencies are computed by the program and can be adjusted to any concentration, temperature or even to a temperature interval (allowing the easy calculation of a reaction mechanism at different temperatures). Furthermore, the quasi-harmonic corrections discussed above can be introduced by just selecting the method and the cut-off value. In addition, the frequencies can be scaled using the appropriate vibrational scaling factor. Finally, the Whitesides method to consider the "free volume" for translational entropy correction was also included for several solvents.[33] The Python code is included in this Thesis in the Appendix section. The tutorial, the code and some examples can be freely downloaded from the Git-Hub repository.[34] Interestingly, the program has been actively used by the computational chemists, especially in the field of organic chemistry mechanisms, where low-lying frequencies affect considerably to the enantioselectivity calculations.[35]

Redox potential calculations for metal oxidations

The Standard Redox Potential (SRP) is one of the most important thermodynamic parameters in electrochemistry. It reflects the capability of a chemical species to be oxidized or reduced. It would be helpful to use computational chemistry to estimate it in a reliable way. We used a thermodynamic cycle to split the SRP into different parameters that can be measured or computed. The development of accurate quantum chemistry calculations, and particularly the solvation description of species in solution, has increased the interest in redox potential calculations, for example in the research field of water oxidation.[36,37,38]

The computational estimation of redox potential of homogeneous species in solution has been successfully addressed,[39,40,41] but the computational estimation of SRP of the solid metals remains a challenge because a mixture of experimental parameters such us the cohesive energy and calculated parameters such us hydration free energy have to be used. The SRP of solid metals is important because of its role in any catalytic cycle in which one solid metal (usually as a powder) is used as a reductant. Recently, the development of reductive coupling reactions has brought up this problem because of the common use of Mn or Zn.[42,43,44] Accurate experimental data are often available in water, but not for the non-aqueous media where these reaction often take place. We thought that an exhaustive study of the thermodynamic cycle (Scheme 2.2) could be useful in order to estimate the SRP in these cases.

Scheme 2.2 Thermodynamic cycle for Standard Redox Potential (SRP) calculations in solid metal oxidation.

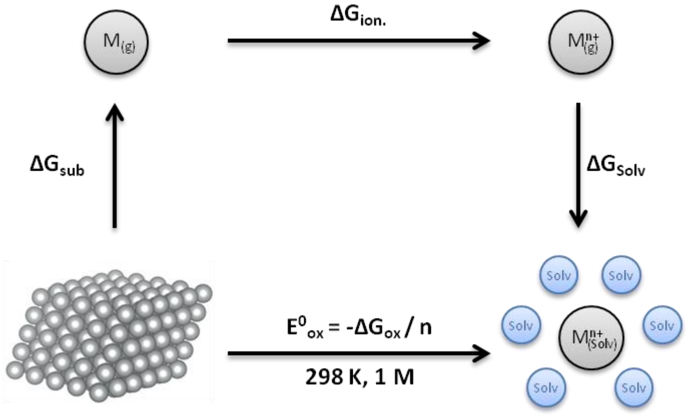

The thermodynamic cycle in Scheme 2.2 has been studied to understand where the error sources lay and to obtain a general methodology where experimental parameters and calculations could be used jointly to estimate the SRP with enough accuracy to study reaction mechanisms.

Standard redox potentials are always referred to the standard state, which is 1 M in solution and 298 K. Although simple at first sight, the literature in the field of redox potential calculations has struggled with this fact, especially in the calculation of the hydration free energies. Indeed different values have been reported for the proton reduction or the free energy of proton solvation.[45] Depending on the selected standard state for the gas phase (1 atm or 1 mol/L) this value changes by 1.89 kcal/mol.[46] In principle, to maintain the standard state the hydration of the proton should go from 1 atm in the gas phase to 1 M in the aqueous phase, and the most accepted value had been reported by Tissandier et al. (-1104.5 kJ/mol)[47] which was latter used to calculate the absolute reduction potential of the proton as 4.28 V.[48,49] We used this value in order to obtain the absolute values of hydration free energies of different metals from the experimental data (Table 2.1).

Table 2.1 Experimental (multiplicity, cohesive energy, ionization energy and hydration energy in water) data for the thermodynamic cycle. All values in eV.

Metal Ion	Multiplicity	Cohesive Energy	Ionization Energy	$\Delta G_{Hydr.}$
Li^+	2 → 1	1.63	5.39	-5.49
K^+	2 → 1	0.934	4.34	-3.65
Ca^{2+}	1 → 1	1.84	17.98	-16.67
Na^+	2 → 1	1.113	5.14	-4.39
Mg^{2+}	1 → 1	1.51	22.68	-20.01
Al^{3+}	2 → 1	3.39	53.26	-48.46
Mn^{2+}	6 → 6	2.92	23.07	-19.36
Zn^{2+}	1 → 1	1.35	27.36	-21.32
Cr^{3+}	7 → 4	4.1	54.21	-47.10
Fe^{2+}	5 → 5	4.28	24.09	-20.29
Co^{2+}	4 → 4	4.39	24.96	-20.90
Ni^{2+}	3 → 3	4.44	25.81	-21.72
Fe^{3+}	6 → 6	4.28	54.74	-45.91
Cu^{2+}	2 → 2	3.49	28.02	-21.86
Cu^+	2 → 1	3.49	7.73	-6.04
Ag+	2 → 1	2.95	7.58	-5.07

The reported experimental values laid on the conventional scale, and the hydration free energy of the proton should be added to obtain the absolute values.[50] We also display in the table the thermodynamic parameters of ionization energy[51] and cohesive energy[52] that will be used for the SRP calculation as well as the multiplicity change of the different electronic states of the metals.[53]

Table 2.2 Experimental and calculated SRP with the conventional approach and the associated error. All values in V. All data in water.

Metal Ion	Experimental SRP (vs NHE)	Calculated SRP (vs NHE)	Error ($SRP_{calc}-SRP_{Exp.}$)
Li^+	-3.040	-2.745	0.29
K^+	-2.931	-2.653	0.28
Ca^{2+}	-2.868	-2.702	0.17
Na^+	-2.710	-2.419	0.29
Mg^{2+}	-2.372	-2.193	0.18
Al^{3+}	-1.662	-1.550	0.11
Mn^{2+}	-1.185	-0.965	0.22
Zn^{2+}	-0.762	-0.584	0.18
Cr^{3+}	-0.744	-0.542	0.20
Fe^{2+}	-0.447	-0.239	0.21
Co^{2+}	-0.280	-0.054	0.23
Ni^{2+}	-0.257	-0.015	0.24
Fe^{3+}	-0.037	0.092	0.13
Cu^{2+}	0.342	0.546	0.20
Cu^+	0.521	0.891	0.37
Ag^+	0.800	1.181	0.38
ME[a]			0.23
MAE[b]			0.23

[a] Mean Error. [b] Mean Absolute Error.

According to the thermodynamic cycle (Scheme 2.2), the SRP can be represented as the sum of the free energies of sublimation, ionization and hydration. The conventional approximation, based on the previous work by Kobayashi and co-workers,[54] estimates the two first quantities as the cohesive energy (C.E) and the ionization energy (I.E.)

respectively, ignoring the entropic contribution to these terms. We reproduced the methodology just using the available experimental data of Table 2.1 using the equation 2.7 (Eq. 2.7) and we compared the obtained values with the experimental standard redox potential of the metals (Table 2.2).[55]

$$\mathrm{E^0_{red}} = -\mathrm{E^0_{ox}} = \frac{-\Delta \mathrm{G^0_{ox}}}{\mathrm{n}} = \mathrm{C.E.} + \mathrm{I.E} + \Delta \mathrm{G^0_{solv}} \qquad \text{(Eq 2.7)}$$

Interestingly, all the calculated SRP have a systematic error towards more positive potentials, with a mean absolute error of 0.23 eV. This error (about 5.3 kcal/mol) is high enough to reconsider a methodology problem.

Therefore, we performed an analysis of the different terms in the thermodynamic cycle to localize the origin of this systematic error. We started with the cohesive energy. This property is defined as the energy required to form separated neutral atoms in their ground electronic state from a solid at 0K and 1 atm.[56] According to the definition, this energy corresponds to the free energy of sublimation at this temperature, but the standard temperature for the SRP calculation is 298 K. For that reason, we included the entropy correction to the cohesive energy, based on the translational entropy of the gas atoms. We calculated that according to the Sackur-Tetrode equation (Eq 2.8) for each metal (M in g/mol, P in atm and T in K), which provides the translational entropy in cal/(mol·K).[57] In addition, we added the enthalpy change for this temperature of the gas phase atoms, which is 5/2RT.

$$\mathrm{S_{Trans(g)}} = 4.576\left(-\log \mathrm{P} + \frac{5}{2}\log \mathrm{T} + \frac{3}{2}\log \mathrm{M} - 0.5053\right) \qquad \text{(Eq 2.7)}$$

Then, the free energy of sublimation is calculated as the cohesive energy plus the enthalpy and entropy corrections (Eq 2.8). The correction factor is presented in table 2.3 as ΔG_{Sub}^{corr}.

$$\Delta G^0_{sub} = \Delta H^0_{sub} - T \cdot \Delta S^0_{sub} = C.E + \frac{5}{2}RT - T \cdot S_{Trans(g)} \quad \text{(Eq 2.8)}$$

Table 2.3 Experimental and calculated SRP with the revised approach and the associated error. All values in V. All data in water.

Metal Ion	**Experimental SRP (vs NHE)**	**$\Delta G_{Sub}{}^{corr}$**	**$\Delta G_{Ion}{}^{corr}$**	**Calculated SRP (vs NHE)**	**Error (SRP_{calc}-$SRP_{Exp.}$)**
Li^+	-3.040	-0.347	0.018	-3.074	-0.03
K^+	-2.931	-0.413	0.018	-3.048	-0.12
Ca^{2+}	-2.868	-0.414	0.000	-2.909	-0.04
Na^+	-2.710	-0.393	0.018	-2.794	-0.08
Mg^{2+}	-2.372	-0.394	0.000	-2.390	-0.02
Al^{3+}	-1.662	-0.399	0.018	-1.677	-0.02
Mn^{2+}	-1.185	-0.426	0.000	-1.178	0.01
Zn^{2+}	-0.762	-0.432	0.000	-0.800	-0.04
Cr^{3+}	-0.744	-0.424	0.014	-0.678	0.07
Fe^{2+}	-0.447	-0.427	0.000	-0.452	-0.01
Co^{2+}	-0.280	-0.429	0.000	-0.269	0.01
Ni^{2+}	-0.257	-0.428	0.000	-0.229	0.03
Fe^{3+}	-0.037	-0.427	-0.005	-0.052	-0.01
Cu^{2+}	0.342	-0.434	0.000	0.329	-0.01
Cu^+	0.521	-0.434	0.018	0.475	-0.05
Ag^+	0.800	-0.452	0.018	0.747	-0.05
ME[a]					-0.02
MAE[b]					0.04

[a] Mean Error. [b] Mean Absolute Error.

In addition, we analyzed the approximation of the ionization free energy as the ionization energy (IE). The experimental value represents the quantity of energy that an isolated, gaseous atom in the ground electronic state needs to release an electron. However, from a macroscopic point of view, this energy should be corrected in order to include the entropic change of this transformation. In that case, the partition function is the same for the neutral atom and the cation with the exception of the electronic partition function, in the cases where the multiplicity of the atom changes. In those cases, the electronic partition function change is equal to the difference of the cation multiplicity and the neutral atom multiplicity. Thus, we calculated the correction to the experimental ionization energy (Eq 2.9) (the correction term is also shown in the table 2.3 as $\Delta G_{\mathrm{Ion}}^{\mathrm{corr}}$). We recalculated the SRP using the correction factors on the cohesive free energy and the ionization free energy (Table 2.3).

$$\Delta G^0_{\mathrm{ion}} = \mathrm{IE} - \mathrm{T} \cdot \Delta S_{\mathrm{Elec}} = \mathrm{IE} - \mathrm{T} \cdot (S_{M^{n+}} - S_{M^0}) \qquad \text{(Eq 2.9)}$$

The obtained results clearly overcome the systematic error, providing a mean error of -0.02 V, very close to the exact value and the absolute error also decreases from 0.23 V to 0.04 V, below 1 kcal/mol. This methodology is now optimized and from this point onwards, it can be used for more interesting mechanistic calculations. In principle, instead of using all the experimental data, if the hydration solvation free energy is calculated in other solvents, this method may access very accurate values for SRP in other solvents, which is not obvious either experimentally or theoretically.

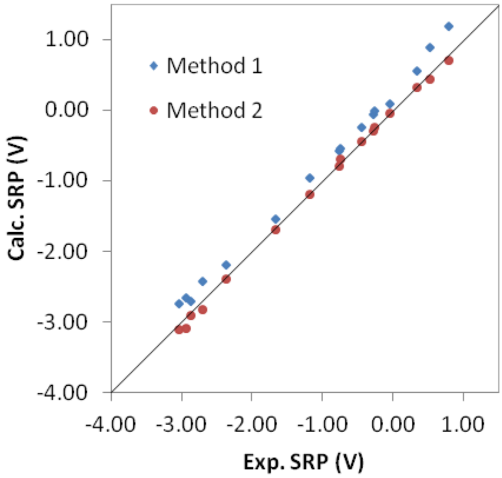

Figure 2.1 Representation of the calculated redox potentials using the conventional approach (method 1) and the redesigned approach (method 2) versus the experimental SRP.

The traditional and our revised method are compared in Figure 2.1. The systematic error of method 1 can be observed, while method 2 provides very precise data.

In conclusion, we have presented a revised approach to calculate the standard redox potentials of the bulk metals from the thermodynamic cycle. It is crucial to include the translational entropy in the gas phase to obtain the correct sublimation free energy, and the change in electronic entropy to obtain the ionization free energy. With these corrections, the SRP calculations have a mean absolute error of only 0.04 V. This method can be a useful tool to calculate the SRP of the metals in non-aqueous solvents for the determination of reaction mechanism where metal powders are used as reductants.

2.4 References

[1] Jensen, F. *Introduction to Computational Chemistry*, 2nd Edition, John Wiley & Sons Ltd.: Chichester, England, 2007.

[2] Hohenberg, P.; Kohn W. *Phys. Rev.* **1964**, *136*, B864-B871.

[3] Kohn. W.; Sham, L.J. *Phys. Rev.* **1965**, *140*, A1133-A1138.

[4] Thomas, L. H. *Proc. Camb. Phil. Soc.* **1927**, *23*, 542-548.

[5] Fermi, E. Rend. *Accad. Lincei.* **1927**, *6*, 602-607.

[6] Dirac, P. A. M. *Proc. Camb. Phil. Soc.* **1930**, *26*, 376-385.

[7] Vosko, S. H.; Wilk, L.; Nusair, M. *Can. J. Phys.* **1980**, *58*, 1200-1211.

[8] Perdew, J. P.; Wang, Y. *Phys. Rev. B* **1992**, *45*, 13244- 13249

[9] Becke, A. D. *Phys. Rev. A* **1988**, *38*, 3098-3100.

[10] Perdew, J. P.; Burke, K.; Ernzerhof, M. *Phys. Rev. Lett.* **1996**, *77*, 3865-3868.

[11] [*Erratum*] Perdew, J. P.; Burke, K.; Ernzerhof, M. *Phys. Rev. Lett.* **1997**, *78*, 1396.

[12] Perdew, J. P. *Phys. Rev. B* **1986**, *33*, 8822-8824.

[13] Lee, C.; Yang, W.; Parr, R. G. *Phys. Rev. B* **1988**, *37*, 785-789

[14] Becke, A. D. *J. Chem. Phys.* **1993**, *98*, 5648-5652.

[15] Stephens, P. J.; Devlin, F. J.; Chabalowski, C. F.; Frisch, M. J. *J. Phys. Chem.* **1994**,*98*, 11623-11627.

[16] Zhao, Y.; Schultz, N. E.; Truhlar, D. G. *J. Chem. Theory Comput.* **2006**, *2*, 364-382.

[17] Zhao, Y.; Truhlar, D. G. *J. Chem. Phys.* **2006**, *125*, 194101-18.

[18] Medvedev, M. G.; Bushmarinov, I. S.; Sun, J.; Perdew, J. P.; Lyssenko, K. A. *Science*, **2017**, *355*, 49-52.

[19] Becke, A. D.; Johnson, E. R. *J. Chem. Phys.* **2005**, *123*, 154101.

[20] Grimme, S. J. Comp. Chem. 2006, 27, 1787-1799.

[21] Grimme, S.; Antony, J.; Ehrlich, S.; Krieg, H. *J. Chem. Phys.* **2010**, *132*, 154104.

[22] Tomasi, J.; Mennucci, B.; Cammi, R. *Chem. Rev.* **2005**, *105*, 2999, 3093.

[23] Marenich, A. V.; Cramer, C. J.; Truhlar, D. G. *J. Phys. Chem.* B **2009**, *113*, 6378-6396.

[24] Jacob, C. R.; Reiher, M. *Int. J. Quantum Chem.* **2012**, *112*, 3661-3684.

[25] Asperger, S. *Chemical Kinetics and Inorganic Reaction Mechanisms*, Springer US: Boston, USA, 2003. pp. 3-103 (chapter 2).

[26] Jensen, J. H. *Molecular Modeling Basis*, CRC Press: Boca Raton, Finland, 2010. Page: 74.

[27] Gaussian 09, Revision **D.01**, Frisch, M. J.; Trucks, G. W.; Schlegel, H. B.; Scuseria, G. E.; Robb, M. A.; Cheeseman, J. R.; Scalmani, G.; Barone, V.; Mennucci, B.; Petersson, G. A.; Nakatsuji, H.; Caricato, M.; Li, X.; Hratchian, H. P.; Izmaylov, A. F.; Bloino, J.; Zheng, G.; Sonnenberg, J. L.; Hada, M.; Ehara, M.; Toyota, K.; Fukuda, R.; Hasegawa, J.; Ishida, M.; Nakajima, T.; Honda, Y.; Kitao, O.; Nakai, H.; Vreven, T.; Montgomery, J. A., Jr.; Peralta, J. E.; Ogliaro, F.; Bearpark, M.; Heyd, J. J.; Brothers, E.; Kudin, K. N.; Staroverov, V. N.; Kobayashi, R.; Normand, J.; Raghavachari, K.; Rendell, A.; Burant, J. C.; Iyengar, S. S.; Tomasi, J.; Cossi, M.; Rega, N.; Millam, J. M.; Klene, M.; Knox, J. E.; Cross, J. B.; Bakken, V.; Adamo, C.; Jaramillo, J.; Gomperts, R.; Stratmann, R. E.; Yazyev, O.; Austin, A. J.; Cammi, R.; Pomelli, C.; Ochterski, J. W.; Martin, R. L.; Morokuma, K.; Zakrzewski, V. G.; Voth, G. A.; Salvador, P.; Dannenberg, J. J.; Dapprich, S.; Daniels, A. D.; Farkas, Ö.; Foresman, J. B.; Ortiz, J. V.; Cioslowski, J.; Fox, D. J. Gaussian, Inc., Wallingford CT, 2009.

[28] Ochterski, J. *Thermochemistry in Gaussian*, Gaussian, Inc: Leeds, UK, 2000.

[29] Ribeiro, R. F.; Marenich, A. V.; Cramer, C. J.; Truhlar, D. G. *J. Phys. Chem. B* **2011**, *115*, 14556-14562

[30] Grimme, S. *Chem. Eur. J.* **2012**, *18*, 9955–9964

[31] Chaid, J.-D.; Head-Gordon, M. *Phys. Chem. Chem. Phys.* **2008**, *10*, 6615-6620.

[32] Alecu, I. M.; Zheng, J.; Zhao, Y.; Truhlar, D. G.; *J. Chem. Theory Comput.* **2010**, *6*, 2872-2887

[33] Mammen, M.; Shakhnovich, E. I.; Deutch, J. M.; Whitesides, G. M. *J. Org. Chem.* **1998**, *63*, 3821-3830

[34] https://github.com/bobbypaton/GoodVibes

[35] Some of selected references where Goodvibes was used: a) Li, Y.; Du, S. *RSC Adv.* **2016**, *6*, 84177-84186. b) Myllys, N.; Elm, J.; Kurtén, T. *Comp. Theor. Chem.* **2016**, *1098*, 1–12. c) Deb, A.; Hazra, A.; Peng, Q.; Paton, R. S.; Maiti, D. *J. Am. Chem. Soc.* **2017**, *139*, 763–775. d) Grayson, M. N. *J. Org. Chem.* **2017**.

[36] Ertem, M. Z.; Gagliardi, L.; Cramer, C. J. *Chem. Sci.* **2012**, *3*, 1293-1299.

[37] Liao, R. Z.; Li, X. C.; Siegbahn, P. E. M. *Eur. J. Inorg. Chem.* **2014**, 728-741.

[38] Acuña-Parés, F.; Codolà, Z.; Costas, M.; Luis, J. M.; Lloret-Fillol, J. *Chem. Eur. J.* **2014**, *20*, 5696-5707

[39] Marenich, A. V.; Ho, J.; Coote, M. L.; Cramer, C. J.; Truhlar, D. G. *Phys. Chem. Chem. Phys.* **2014**, *16*, 15068-15106.

[40] Winget, P.; Weber, E. J.; Cramer, C. J.; Truhlar, D. G. *Phys. Chem. Chem. Phys.* **2000**, *2*, 1231-1239.

[41] Baik M. –H. Friesner, R. A. *J Phys. Chem. A* **2002**, *106*, 7407-7412.

[42] Correa, A.; León, T.; Martin, R. *J. Am. Chem. Soc.* **2014**, *136*, 1062-1069.

[43] Yu, X.; Yang, T.; Wang, S.; Xu, H.; Gong, H. *Org. Lett.* **2011**, *13*, 2138-2141.

[44] Gu, J.; Wang, X.; Xue, W.; Gong, G. *Org. Chem. Front.* **2015**, *2*, 1411-1421.

[45] Mejias, J. A.; Lago, S. *J. Chem. Phys.* **2000**, *113*, 7306-7316.

[46] Kelly, C. P.; Cramer, C. J.; Truhlar, D.G. *J. Phys. Chem. B.* **2006**, *110*, 16066-16081.

[47] Tissandier, M. D.; Cowen, K. A.; Feng, W. Y.; Gundlach, E.; Cohen, M. H.; Earhart, A. D.; Coe, J. V. *J. Phys. Chem. A* **1998**, *102*, 7787-7794.

[48] Lewis, A.; Bumpus, J. A.; Truhlar, D. G.; Cramer, C. J. *J. Chem. Educ.* **2004**, *81*, 596-603.

[49] [Erratum] Lewis, A.; Bumpus, J. A.; Truhlar, D. G.; Cramer, C. J. *J. Chem. Educ.* **2007**, *84*, 934.

[50] Fawcett, W. R. *J. Phys. Chem. B.* 1999, *103*, 11181-11185.

[51] Ed. Lide, D. R. *CRC Handbook of Chemistry and Physics*, 84th ed. CRC Press, U.S.A. **2003-2004**, pp. 10(178-180)

[52] Kittel, C. *Introduction to Solid State Physic*, 8th ed. John Wiley & Sons, U.S.A. **2005**, p 50.

[53] Karplus, M.; Porter, R. N. *Atoms and Molecules*, W. A. Benjamin, U.S.A. **1970**, pp 202-207.

[54] Shimodaira, Y.; Miura, T.; Kudo, A.; Kobayashi, H. *J. Chem. Theory. Comput.* **2007**, *3*, 789-795.

[55] Lide, D. R. *CRC Handbook of Chemistry and Physics*, 84th Edition, CRC Press, Florida, USA, 2003, pp. 8.23-8.33.

[56] Glasser, L.; Sheppard, D. A. *Inorg. Chem.* **2016**, *55*, 7103-7110.

[57] Tawa, G. J.; Topol, I. A.; Burt, S. K.; Caldwell, R. A.; Rashin, A. A. *J. Chem. Phys.* **1998**, *109*, 4852-4863.

Chapter 3

Oxidative Coupling

3.1 Background

General introduction

Cross-coupling reactions catalyzed by transition metals revolutionized synthetic chemistry in the last decades of the past century.[1] The formation of C-C bonds or C-X bonds was successfully achieved for a wide variety of substrates. In fact, the development of cross-coupling reactions was recognized with the Nobel Prize in 2010 to Heck, Suzuki and Negishi,[2] demonstrating how far-reaching this advance was. However, these methodologies usually require a pre-functionalization of the substrate, as they operate on reactants containing relatively unusual heteroatoms such as boron, zinc, tin, silicon, etc. Therefore, a lot of waste byproducts are produced. Traditional cross-coupling reactions thus fit poorly with the urgent societal demand about minimizing the human impact on the environment. This has motivated the development of more sustainable and green approaches to organic synthesis,[3] trying to improve the atom economy of chemical reactions. In this context, discovering clean alternatives to cross-coupling reactions is a XXIst century challenge because the construction of new chemical structures is, and will be, a very important factor towards science progress.

Scheme 3.1 Classic cross-coupling *vs* oxidative and reductive coupling reactions.

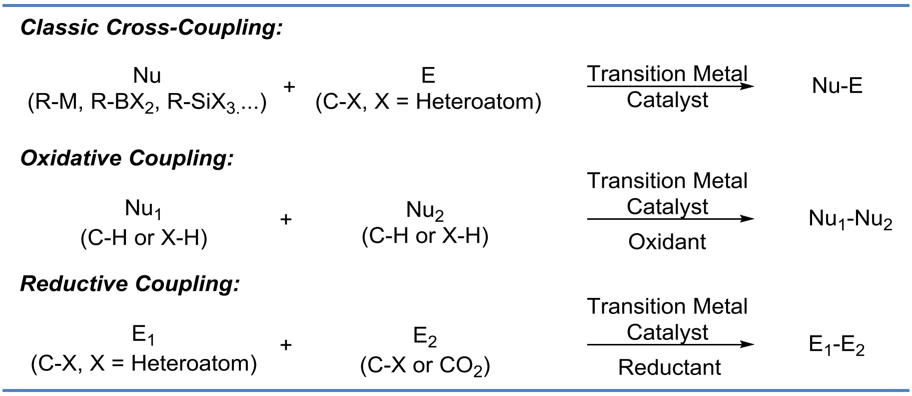

During the last years, oxidative coupling reactions have emerged as a clean alternative to the classic cross-coupling.[4] The aim of this methodology is the same, to build chemical complexity, but increasing the sustainability of the reactions. Comparing both methodologies (Scheme 3.1), classic cross-coupling consists on the reaction of a nucleophile with an electrophile, resulting in a redox-neutral catalytic cycle. In contrast, oxidative coupling is the coupling of two nucleophiles under oxidative conditions. This seemingly little change implies large advantages in terms of reaction atom economy, since no pre-functionalization is required and two C-H or X-H (where X is a heteroatom) can be coupled directly. In addition, the final oxidant to be used in oxidative coupling could be molecular oxygen, only producing water as waste product, which is non-toxic and very convenient to scale up the processes to the industrial level. Finally, reductive couplings, which are based on transition metals and a reductant, have also been developed, especially to introduce CO_2 as an electrophile.[5]

Scheme 3.2 Catalytic cycles of traditional cross-coupling (left) and oxidative coupling (right) reactions.

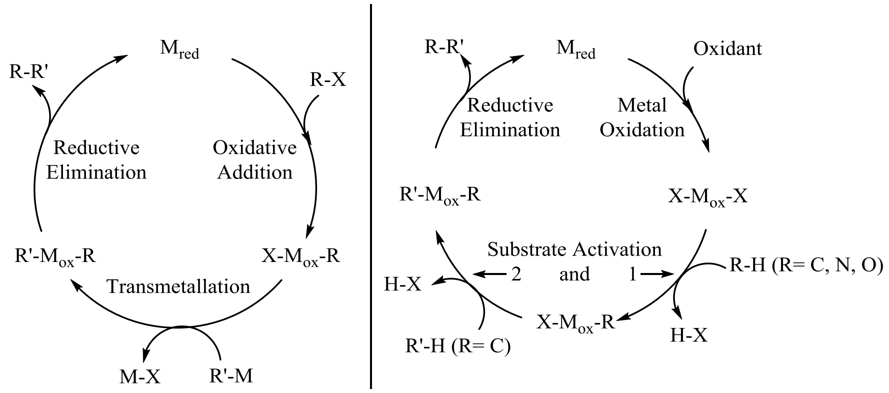

From a mechanistic point of view, the catalytic cycles of both methodologies have several differences (Scheme 3.2). In classic cross-coupling (Scheme 3.2, left), the reaction usually starts with the oxidative addition of an electropositive carbon atom (usually a C-halogen bond), oxidizing the metal by two electrons. Then, the transmetallation can occur with an electronegative carbon center (usually a C-Zn, C-B or C-Si bond), releasing the M-X derivative as waste product. Finally, the metal in high oxidation state undergoes the reductive elimination of both R residues to yield the final product and to regenerate the catalytic cycle. The reaction scope is usually very sensitive to the transmetallation partner, resulting in the wide variety of cross-coupling reactions that have been reported.[6]

On the other hand, in oxidative coupling the substrate usually reacts with the metal catalyst in a high oxidation state. This metal catalyst can activate efficiently a lot of different substrates, cleaving C-H, O-H or N-H bonds. This feature allows performing reactions without any pre-functionalization. A second substrate is activated in a similar way to yield the catalyst with both nucleophiles attached. Unlike in the oxidative addition step of cross-couplings, the metal does not change the oxidation state during these two steps. Then, the reductive elimination releases the product forming the bond between both R groups, reducing the metal to a low valence state. Finally, to regenerate the catalytic cycle, an extra step is needed, the reoxidation by an external oxidant, that can be metal based (copper(II) or silver(I)), or ideally molecular oxygen, which is the cheapest oxidant and minimizes the amount of waste by-products.[7,8,9] Nevertheless, it is important to remark that although cross-coupling reaction mechanisms are well described in the literature, the oxidative coupling mechanisms have still some uncertainties such as the role of the oxidant, the eventual role of the single electron transfer oxidations (especially when first row transition metals are used as catalysts) and the C-H activation mechanism.

Scheme 3.3 Common C-H activation mechanisms by transition metals.

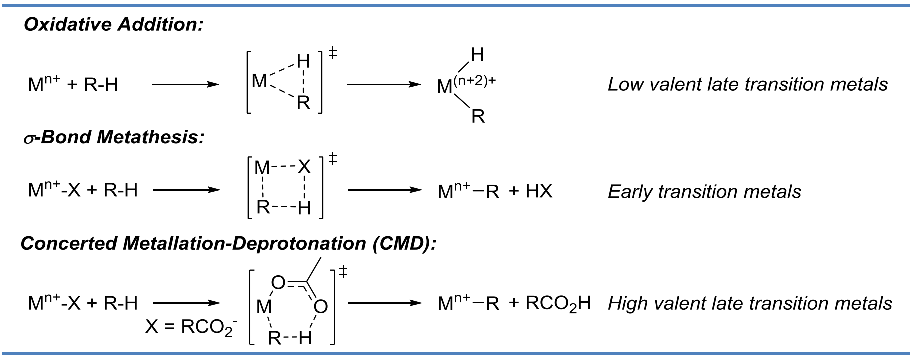

Oxidative coupling is strongly related to the activation of C-H bonds by transition metals, as this is the usual way to access the M-R species that makes possible the final coupling of the substrates (see Scheme 3.2, right). C-H activation has been exhaustively discussed in the literature.[10,11,12] Depending on the metal and substrates, several mechanisms have been proposed for the C-H activation. The most relevant ones are described in Scheme 3.3. If a metal can reach a higher oxidation state, the oxidative addition of C-H bond would be the most preferred mechanism. This is usually the case in low valent late transition metals, since the oxidation state of the metal increases by two units,[13] but it is not the normal case for oxidative couplings, in which high valent metals, such as Rh(III) or Pd(II) are commonly used as the catalyst. σ-Bond metathesis consists of the addition of the C-H bond to an activated M-C or M-H bond, typically on early transition metals. Finally, the most widely explored C-H activation mechanism for oxidative couplings is the concerted metallation-deprotonation mechanism (CMD).[14,15,16] In this case, an external base, most often a carboxylate attached to the metal, helps in the deprotonation of the activated C-H bond. There is a recent comprehensive review on the field that collects the large number of systems in which CMD is the C-H activation mechanism.[17]

Scheme 3.4 Oxidative couplings with copper(II) acetate as external oxidant. Activated C-H or X-H bonds are highlighted in red.

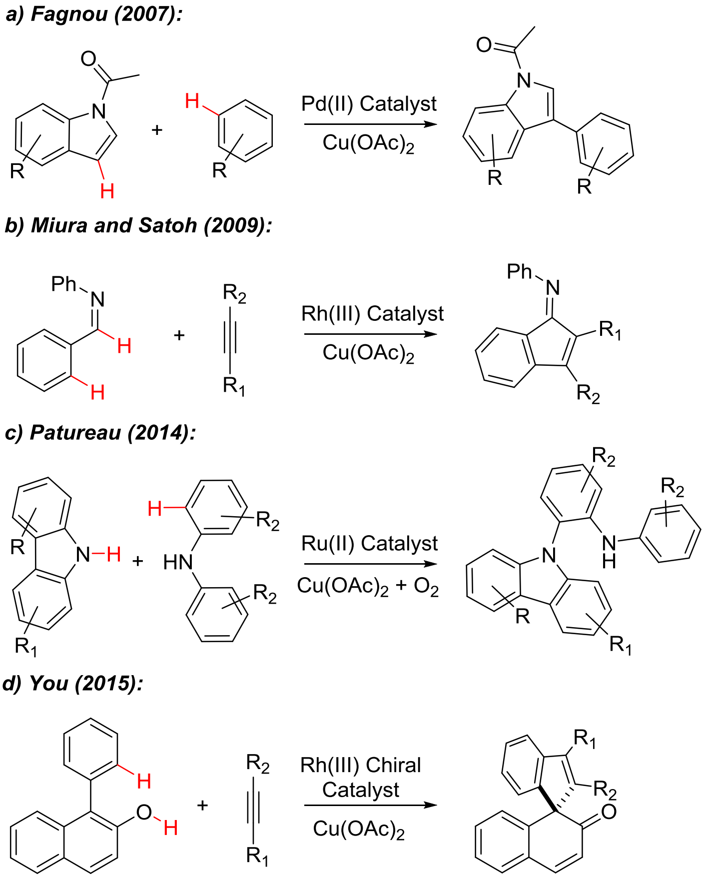

Regarding the catalyst for oxidative coupling reactions, several metals have been used, those more usual are probably rhodium,[18,19,20,21] palladium,[22,23] and ruthenium.[24,25] Recently, other non-noble metal centers, such as cobalt[26] or copper,[27] have also been developed as cheaper and less toxic alternatives, although the efficiency of these systems is still far from those based on precious metals. The nature of the external oxidant used on the process is also often a critical factor on the yield and even on the selectivity of the reaction. Remarkably, the most commonly used oxidant is copper(II) acetate, even though it is not particular cheap or easy to manipulate.

Some representative examples of oxidative coupling are depicted in Scheme 3.4: (a) the seminal example by Fagnou and co-workers on the Pd oxidative cross-coupling or arenes,[28] (b) one example of the large collection of rhodium catalyzed oxidative couplings reported by Miura and Satoh,[29] (c) the C-N oxidative coupling to form asymmetric secondary amines catalyzed by Ru complex reported by Patureau and co-workers, where the presence of molecular dioxygen increases the yield,[30] and (d) an impressive enantioselective oxidative coupling by a chiral rhodium catalyst discovered by You and co-workers, where the alkyne insertion is also regioselective.[31]

Oxidant different from copper acetate may be utilized too. This is the case of silver acetate [32,33,34] and Oxone® [35,36], but the scope is more limited. For this reason, one of the main objectives of this thesis is to understand the effect of the oxidant on the reaction. There are also examples where molecular oxygen is used as final oxidant (the ideal case),[37,38] producing only water as side product, but even in these cases, a co-catalyst is frequently needed, normally copper(II) acetate.[39] This fact is quite surprising as it indicates that copper species can have a more elaborate role during the catalytic cycle, beyond acting as an external oxidant.

As we mentioned before, CMD is usually the mechanism for C-H activation. Therefore, it is favored by the presence of a carboxylate attached to the catalyst. However, the catalyst precursors usually do not have this functional group as ligand (i. e. $[Cp^*RhCl_2]_2$ or $[(C_6H_6)RuCl_2]_2)$ and the ligand substitution with the acetate species is key to form the overall process. This topic has been extensively studied from an experimental point of view by Jones and co-workers in the case of Rh(III) species.[40] They demonstrated that only at higher concentrations of free acetate (with NaOAc as additive), the formation of $[Cp^*Rh(OAc)_2]$, which is assumed in most of the cases as the active catalyst, is achieved. For this reason, the exchange of acetates with the copper acetate dimer is not obvious, and can be the reason for an active role for this oxidant. On the contrary, silver acetate can trap the chloride atoms of the precursor forming the rhodium(III) diacetate species. This fact explains why sometimes little amounts of silver acetate are added to the reaction when copper acetate is used as the oxidant.[41,42]

All the questions regarding the formation of the active species and the specific role of oxidants in oxidative couplings are still a challenge from a mechanistic point of view. For this reason, we thought that a comprehensive computational study on these topics was and still is necessary to help in the rational design of new reactions, and to control all the factors that affect the reactivity.

Previous mechanistic studies

The rapid development of experimental advances in the field of oxidative coupling has derived in a lot of questions about the mechanism that should be answered to have a complete view of these methodologies. DFT calculations has been used previously to described many homogenous catalytic cycles with good accuracy, and since the development of modern DFT techniques, many advances in the field of computationally calculated mechanisms of cross-coupling reactions have been made by our group [43,44,45,46] and others.[47,48] However, considering the differences in the catalytic cycles of both reactions (see Scheme 3.2), the direct extrapolation of the cross-coupling mechanistic information to oxidative couplings is not obvious. In addition, the C-H activation mechanisms by transition metals have also been studied in depth, especially the concerted metallation-deprotonation mechanism, as discussed above. A representative example of the oxidative C-H functionalization was thoroughly studied by Schoenebeck and Sanford who focused on the reaction selectivity depending on the anion, demonstrating both computationally and experimentally the effect of the base in the site-selective functionalization of arenes.[49] Another mechanistic study by Morokuma and co-workers showed the possibility of external CMD activation, where the carboxylate is not attached to the rhodium center.[50] Also, mechanistic experiments of stoichiometric reactions have confirmed the CMD C-H activation mechanism, isolating different metallacycles.[51,52] However, computational studies on the full catalytic cycle of oxidative couplings are still very scarce.

In the case of oxidative couplings, different authors have recently reported several catalytic cycles for rhodium catalyzed reactions such as internal oxidant-controlled reactions,[53,54] an intramolecular version of alkyne coupling to a benzamide,[55] and a comprehensive study of heterocycles synthesis in which selectivity issues are also addressed.[56] [CpRh(OAc)$_2$] was assumed as the active species in all these cases, which we consider to be a significant simplification. Another remarkable example was reported by Lledós and co-workers on a ruthenium catalyzed oxidative coupling of primary amines and internal alkynes. In this case, the formation of [Ru(p-cymene)(OAc)$_2$] from the chloride precursor [Ru(p-cymene)Cl$_2$]$_2$ was also assumed to be the active species under copper(II) acetate oxidative conditions.[57] More recently, MacGregor and co-workers reported the first mechanistic study on a cobalt catalyzed oxidative coupling.[58] This first-row transition metal can operate in a variety of spin state and oxidation state, differing considerably to noble-metal catalyzed reactions.

We consider the study of full catalytic cycles as the best approach to analyze all the factors in oxidative couplings and to model *via* rational design these complex reactions, in which different transition metals influence the region-, the chemo- or the enantioselectivity.[59] In this chapter, we will describe the computational study of the catalytic cycle of two relevant reactions, the Rh(III) catalyzed oxidative coupling of benzoic acid and alkynes and the Ru(II)/Cu(II) co-catalyzed dehydrogenative homocoupling of carbazoles under air. The computational study of these reactions covers most of the factors outlined in this introduction, such as the C-H activation mechanisms, the effect of the oxidant, the influence of copper acetate in the catalytic cycle and the formation of the active species in oxidative couplings.

3.2 Computational details

Computational methods

All the calculations reported in this chapter were carried out with the Gaussian09 (revision D.01) program package [60] using density functional theory (DFT). For both sections 3.3 and 3.4, the B97D functional was selected to compute the reaction mechanisms.[61] The performance of other functionals such as B3LYP-D3,[62] M06-D3,[63] BP86-D3 [64] (D3 states Grimme-D3 dispersion corrections),[65] ωB97X-D,[66] TPSSh,[67] and B3LYP were tested for the oxidative coupling between benzoic acid and alkyne. All geometries were optimized without symmetry restrictions and vibrational frequency calculations were computed for all stationary points to establish their nature as minima (without imaginary frequencies) or transition states (with one imaginary frequency). In the case of transition state optimizations, relaxation to reactant and product was done in all the cases, confirming the connectivity between intermediates. In addition, when relaxation was inconclusive, IRC calculations were carried out to confirm the connectivity. Free energy corrections were calculated for all species at 298.15 K and 1 atm pressure, including zero point energy corrections (ZPE).

Solvent was considered implicitly in all the optimizations and single point corrections for both mechanistic studies through the SMD model,[68] using the experimental solvent in each case, *ortho*-xylene (ε = 2.5454) for section 3.3 and diphenylether (ε = 3.73) for section 3.4. Diphenylether was selected due to the dielectric constant value between those of chlorobenzene (ε = 5.6968) and tetrachloroethene (ε = 2.268) used as solvent mixture in the experimental reaction.

In order to minimize the basis set superposition error (BSSE), especially considering that dimeric species are involved in the catalytic cycles, we refined the energies by introducing an extended basis set. Firstly, we used basis set (I) for optimization and frequency calculations and then, all potential energies were recomputed using basis set (II) in single-point calculations. Basis set (I) was LANL2DZ and the associated pseudopotential for metals (Rh/Cu/Ag in section 3.3 and Ru/Cu in section 3.4)[69] and 6-31G(d) for the rest of atoms (C, H, O, N, Cl).[70] Basis set (II) was increased to triple-zeta level using LANL2TZ(f) (including the corresponding pseudopotential)[71] for metals and 6-311++G(d,p) for the rest of the atoms.[72] Additionally, we did a benchmarking with other two basis sets for the rhodium catalyzed reaction . We kept the same basis set in (II) for rhodium and copper (LANL2TZ(f) and the associated pseudopotential), changing the basis set for the other atoms to Def2TZVP and Def2TZVPP.[73]

Along the sections 3.3 and 3.4, several 3D structures were drawn with GaussView Program.[74] The legend of colors used in 3D structures is:

Carbon: ▨ Hydrogen: ⬜ Oxygen: 🟥 Nitrogen: 🟦

Chloride: 🟩 Rhodium: 🟦 Copper: 🟥 Silver: 🟦

Ruthenium: 🟦

Benchmarking of the computational method

The selection of the proper functional for density functional theory calculations is very important, especially when open-shell electronic structures are on the reaction pathway. For this reason, we analyzed different functionals to see where the differences are and to select the most appropriate for the oxidative coupling reactions that we have studied. In addition, we considered different basis set to minimize the basis set superposition without increasing substantially the computational cost. Finally, due to the presence of $[Cu(OAc)_2(H_2O)]_2$ in reaction mechanisms, we considered the relative stability of three different electronic structures (closed-shell singlet, open-shell singlet and triplet). We focused these benchmarking studies on the structures collected in Tables 3.1, 3.2 and 3.3. They correspond to the reductive elimination step of rhodium catalyzed oxidative coupling, the labels will be fully explained in section 3.3 (Figure 3.9). We chose this step because it determines the chemoselectivity of the reaction.

Table 3.1 Comparison of the performance of seven different functionals on the key steps of oxidative coupling. Free energies in kcal/mol related to **10**.

Functional	10	22	TS 22-23	23	TS 10-11	11	TS 10-12	12
B97D	0.0	-15.2	0.6	-20.1	13.0	-11.3	8.2	-14.6
M06-D3	0.0	-22.6	3.2	-28.2	12.8	-19.3	11.3	-11.0
B3LYP-D3	0.0	-23.2	10.2	-23.2	16.4	-9.2	12.2	-10.0
BP86-D3	0.0	-21.8	1.3	-17.6	14.0	-12.2	8.0	-7.6
ωB97X-D	0.0	-21.7	12.6	-17.5	17.6	-15.8	14.7	-9.0
TPSSh	0.0	-7.1	24.4	2.1	14.5	-13.5	10.6	-10.1
B3LYP	0.0	-4.9	29.1	-6.3	15.8	-8.4	12.9	-15.0

We calculated the chemoselectivity determining step with seven different functionals in order to analyze the influence of different parameters, such as Hartree-Fock exchange and empirical dispersion correction in the free energy profile of rhodium-copper catalyzed oxidative coupling (Table 3.1).

Basis set (II) was used in all these calculations. Although the absolute values change depending on the method, the critical ordering between **TS 22-23**, **TS 10-11** and **TS 10-12** is the same in most cases. The exception happens with TPSSh and B3LYP, where empirical dispersion is not included, so the energy of trimetallic structures (**22**, **TS 22-23** and **23**) is vastly overestimated. Regarding the use of pure (B97D and BP86-D3) or hybrid (B3LYP-D3 and M06-D3) functionals, there are not many differences, although hybrid ones predict barriers quite high for a thermal process. With these considerations and in order to reduce the computational cost, we chose to use B97D throughout the study.

Table 3.2 Comparison of the performance of four different basis sets for the key steps of oxidative coupling. Free energies in kcal/mol related to **10**.

Basis Set	**Number of Basis**[a]	**10**	**22**	**TS 22-23**	**TS 10-11**	**TS 10-12**
6-31G(d)/ LANL2DZ	618	0.0	-18.3	-6.1	12.1	7.5
6-311++G(d,p)/ LANL2TZ(f)	1101	0.0	-15.2	0.6	13.0	8.2
Def2TZVP/ LANL2DZ	1385	0.0	-12.2	4.1	13.3	8.5
Def2TZVPP/ LANL2DZ	1611	0.0	-12.2	4.3	13.3	8.5

[a] Number of basis functions for the largest calculations (**22**, **TS 22-23** and **23**)

We also studied the influence of the number of basis in the same step. The results of this analysis, always with the B97D functional, are collected in Table 3.2. The large difference in the number of atoms between the cooperative pathway and the rhodium catalyzed pathway is critical due to the basis set superposition error. We found that triple-zeta basis set are needed to minimize this error, but the energies among different triple-zeta basis set are not so different. In all the cases, the qualitative description remains the same, and for this reason, we decided to use the 6-311++G(d,p)/LANL2TZ(f) combination. This basis set provides a good description of the system while keeping a relatively low computational cost.

Table 3.3 Comparison of different electronic states for key steps of oxidative coupling. Free energies in kcal/mol referred to **10**..

Electronic State	10	22	TS 22-23	23
Triplet	0.0	-15.2	0.6	-20.1
Open-shell Singlet	0.1	-15.2	1.7	-19.9
Close-shell Singlet	6.2	-10.7	6.1	-13.5

Finally, we considered the different possibilities regarding the electronic structure of the system (Table 3.3). Closed-shell singlet structures are always higher in energy about 6.0 kcal/mol, and for this reason we discarded this multiplicity. In contrast, open-shell singlet and triplet states are almost equal in energy, although the triplet is more stable in the transition state by 1.1 kcal/mol. This is because both unpaired electrons do not interact among themselves, and the free energy correction is more favorable to the triplet structure due to the larger multiplicity. Therefore, we carried out our calculations on the triplet electronic state with the caveat that we admit that an open-shell singlet may be possible in some cases but with very similar energies involved.

3.3 Oxidative Coupling between Benzoic Acid and Alkynes. The Key Role of the Oxidant

Reaction overview

In 2007, Miura and Satoh reported a breakthrough oxidative coupling of benzoic acid and alkynes catalyzed by rhodium(III) species.[75,76] During the reaction, C-H and O-H bonds are activated, then one molecule of alkyne is inserted and finally there is a reductive elimination to yield an isocoumarin derivative. Consequently, the organic reactants formally lose two electrons during the process and for this reason, an oxidant is needed in the reaction. We selected this specific example because it is one of the well-characterized reactions where the oxidant clearly plays an active role during the process. There are three different possibilities: if $Cu(OAc)_2$ is used as the oxidant (Table 3.4, entry 1), the transformation is totally chemoselective to form isocoumarin compounds; if Ag(OAc) is selected as the oxidant, the reaction yields mixtures of compounds **3** and **4** (Table 3.4, entry 2); finally, O_2 can also be used as final oxidant but under the presence of catalytic copper diacetate, being also selective to compound **3** (Table 3.4, entry 3).

Table 3.4 Oxidative coupling of benzoic acid and alkynes catalyzed by Rh(III) under different oxidants.[776]

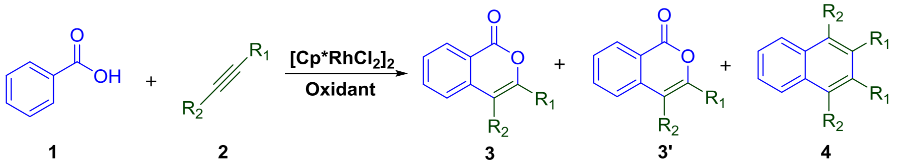

Entry	R₁	R₂	Oxidant (Eq.)	Solvent	T(ºC)	Yield (3; (3'); 4)
1	Ph	Ph	$Cu(OAc)_2 \cdot H_2O$ (2)	*o*-Xylene	120	95:5
2	Ph	Ph	AgOAc (4)	Mesitylene	180	40:60
3	Ph	Me	$Cu(OAc)_2 \cdot H_2O$ (0.05)/O_2 (air)	DMF	120	84:5:0
4	Ph	Me	$Cu(OAc)_2 \cdot H_2O$ (2)	*o*-Xylene	120	89:9:0
5	Ph	Bu^n	$Cu(OAc)_2 \cdot H_2O$(2)	*o*-Xylene	120	86:14:0

Since one of the most intriguing features of oxidative coupling is the influence of the oxidant, we found this work inspiring. We envisioned that a computational study on the mechanism of this reaction could help to understand how the experimental conditions of these copper assisted dehydrogenative couplings could be modified and improved.

Another interesting feature of this reaction is the regioselectivity of the alkyne insertion. When asymmetric alkynes are used (Table 3.4, entries 3, 4 and 5), the regioselectivity is up to 10:1, favoring the formation of the isocoumarin **3**, with the phenyl group always near to the oxygen in the isocoumarin ring, even if large alkyl groups such as n-butyl are used.

Scheme 3.5 Mechanistic proposal reported in the original paper.[76]

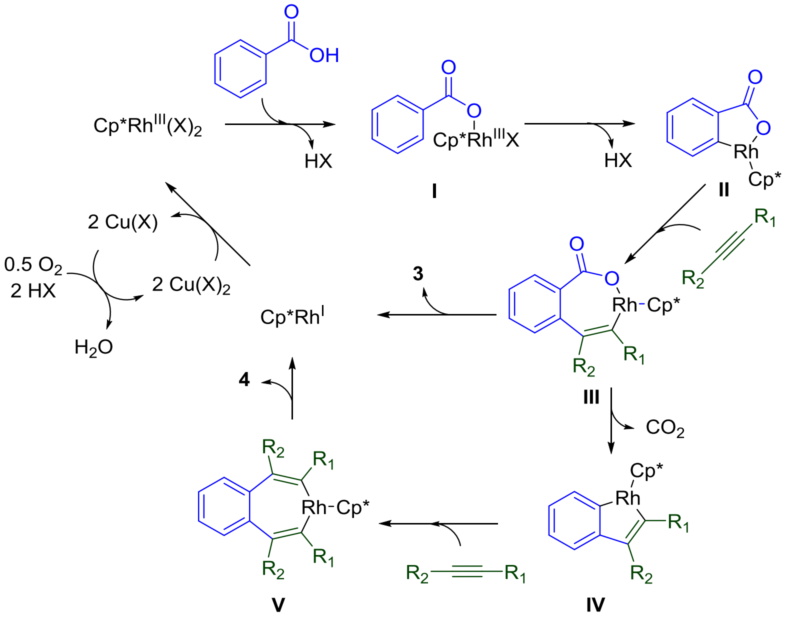

According with the experimental data, the authors reported a mechanistic proposal (Scheme 3.5) based on Rh(III)/Rh(I) catalytic cycle. A general [$Cp^*Rh(III)X_2$] species was proposed although following other reports in the literature, [$CpRh(OAc)_2$] is more likely to be the active catalyst.

The reaction starts with the activation of benzoic acid through O-H bond, forming rhodium benzoate derivative **I**. Then, ortho-rodation occurs through C-H activation, forming rodacycle **II**, which has been detected in similar stoichiometric reactions with Rh(III) species.[77] Once both O-H and C-H bonds are activated, the alkyne insertion takes place regioselectively forming intermediate **III**. From this point, there are two different options: the major product **3** can be formed *via* reductive elimination, closing the ring by C-O bond formation and generating Rh(I) or minor product **4** can be generated by CO_2 extrusion (intermediate **IV**), followed by the second alkyne insertion (intermediate **V**), and yielding the naphthalene derivative **4** by C-C bond formation through reductive elimination, reducing Rh(III) to Rh(I). Thus, both pathways would form Rh(I), which can be reoxidized by copper(II) diacetate to restart the catalytic cycle giving copper(I) acetate as side product. In turn, Cu(I) can be also reoxidized by molecular oxygen in the co-catalytic version of the reaction, forming water as side product and regenerating the initial copper(II) diacetate.

Although the proposed mechanism is plausible as it is in line with other Rh(III) reaction mechanistic proposals, it neglects the effect of the oxidant in the chemoselectivity and this fact prompted us to analyze the reaction mechanism in detail by means of density functional theory (see Section 3.2 for computational details). For the computational study, we specifically selected the entry 4 of table 3.4 to cover also the alkyne insertion regioselectivity. We used this system for all the study, including the Rh-based catalytic cycle (as the mechanistic proposal), the Rh/Cu cooperative pathway and also Rh/Ag to understand the differences in reaction outcome. In all the calculations, we replaced Cp* moiety by Cp to reduce the computational cost, as Cp is always far from reactive sites.

[CpRh(OAc)$_2$] catalytic cycle

As starting point of the mechanistic study, we followed the proposed reaction mechanism, assuming [CpRh(OAc)$_2$] as active catalyst (Figure 3.1). Surprisingly, the generation of this active species from rhodium precursor and copper(II) diacetate dimer is, in terms of free energy, not so favorable (**5**, +20,3 kcal/mol). This result is in agreement with previous stoichiometric studies about [CpRhCl$_2$]$_2$/OAc$^-$ mixture, where the concentration of free acetate (under this reaction conditions, there is almost no free acetate when $[Cu(OAc)_2H_2O]_2$ is used) is critical in the formation of rhodium diacetate species, as we discussed in the introduction.

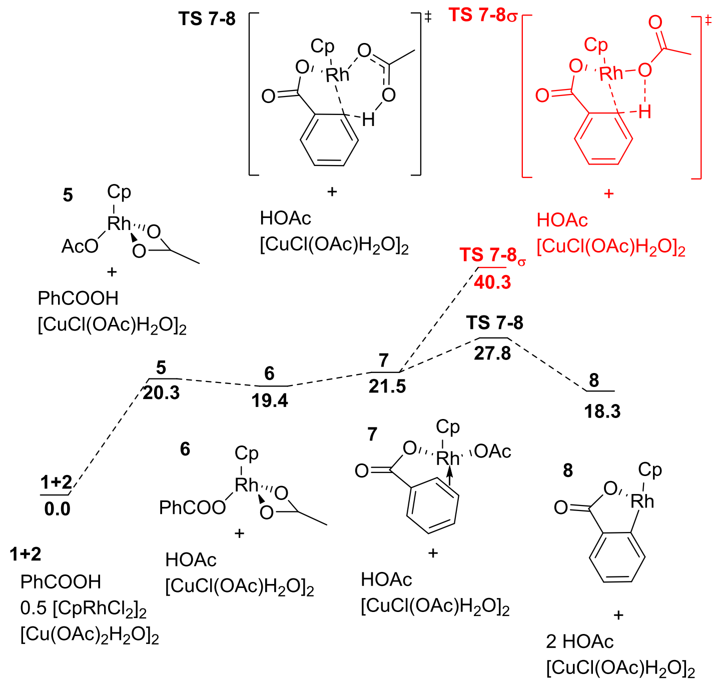

Figure 3.1 Free energy profile of $[CpRh(OAc)_2]$ catalyzed C-H activation. Energy in kcal/mol.

The mechanism starts with the substitution of one acetate of $[CpRh(OAc)_2]$ by benzoate, forming acetic acid and intermediate **6** exergonically by 0.9 kcal/mol. This is consistent with the relative acidities of both acids (pK_A 4.204 for PhCOOH and 4.756 for CH_3COOH).[78] Then, one Rh-O bond of the bidentate Rh-OAc is broken and the vacancy is occupied in **7** by the double bond *ortho* to carboxylate in the benzoic acid. This specific conformation activates the *ortho* carbon selectively, with the carboxylate group acting as directing group. Furthermore, the pending acetate on intermediate **7** is directed towards C-H bond, facilitating the activation *via* a Concerted Metallation-Deprotonation transition state (CMD), which is very common in transition metal mediated C-H activations as we described in the introduction. **TS 7-8** is only 6.3 kcal/mol higher in energy than **7**, but the overall barrier with respect to the reactant is considerably high, 27.8 kcal/mol, suggesting that $[CpRh(OAc)_2]$ is not the active catalyst for this reaction. After this transition state, the rodacycle **8** is formed. **8** is quite stable even containing a vacancy in the Rh(III) center coordination sphere. **TS 7-8$_\sigma$**, the σ-bond metathesis transition state was also calculated, but it is much higher in energy (12.5 kcal/mol) than CMD.

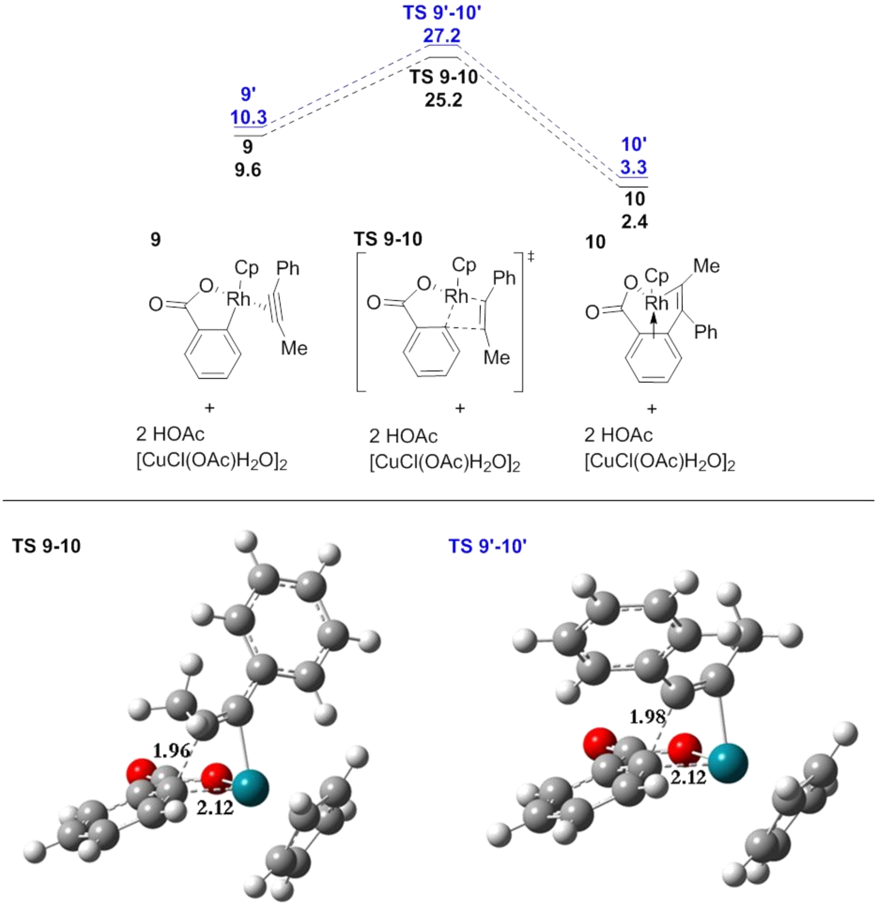

Figure 3.2 Free energy profile for alkyne insertion into Rh-C bond. Main pathway in black, and minor pathway in blue (rotating alkyne 180º). Energy in kcal/mol. (top) 3D structures of **TS 9-10** and **TS 9'-10'** highlighted. Bond lengths in Å. (bottom)

Once the O-H and C-H bonds have been activated, the rodacycle **8** can coordinate 1-phenyl-1-propyne in two different ways (Figure 3.2, left), with the methyl group pointing away from the aromatic ring of benzoic acid (**9**) or towards to this ring (**9'**). Both conformations can promote the alkyne insertion in the Rh-C bond through concerted transition states. The energies of the regioselective transition states **TS 9-10** and **TS 9'-10'** are in agreement with the experimentally observed selectivity (93% of **3** and 7% of **3**'), having an energy difference of 2.0 kcal/mol. The structure of both transition states is strongly correlated with this energy difference (Figure 3.2, bottom). While **TS 9-10** does not have any steric hindrance between alkyne and benzoate, in **TS 9'-10'** both phenyl groups are almost perpendicular, obstructing the π-stacking interaction, and increasing the associated energy. This fact implies an elongation of C-C interaction in the transition states of 0.02 Å. The resulting 7-member rings **10** and **10'** have energies of 2.4 and 3.2 kcal/mol, more stable than previous intermediates. The following steps are lower in energy and for this reason, these are the regioselective determining transition states. We continued the study only from the more stable intermediate **10**.

According to the proposed mechanism by the experimental group, there are two different possibilities from intermediate **10**, the reductive elimination and the CO_2 extrusion pathways. This step defines then the outcome of the reaction, yielding the isocoumarin product **3** or the naphthalene derivative **4**, respectively. Remarkably, the relative barriers in the calculated pathways (Figure 3.3) are in strong disagreement with the experimental outcome (no product **4** is observed when 1-phenyl-1-propyne is used). In this reaction pathway, reductive elimination has a barrier 4.8 kcal/mol higher than CO_2 extrusion, which implies that only **4** would be obtained. Moreover, the stability of the following intermediates **11** (-8.8 kcal/mol) and **12** (-12.2 kcal/mol) prevents the reaction from going back. Regarding the TS geometries (Figure 3.3), the rhodium center is strongly coordinated to the benzoic aromatic ring, favoring the CO_2 extrusion rather than the reductive elimination. For this reason, we considered also an alternative mechanism with saturation of the Rh(III) coordination sphere with free acetic acid (that is present in the reaction media), but this transition state **TS 10-11**$_{\mathbf{HOAc}}$ was even higher. These facts, in conjunction with the absence of oxidant effect in the proposed mechanism of scheme 3.5, led us to discard this reaction pathway.

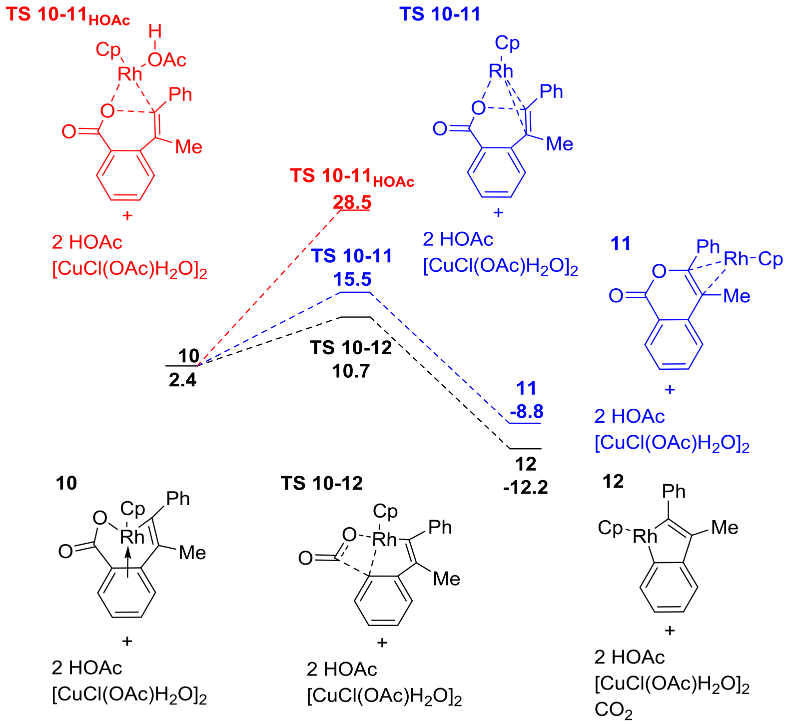

Figure 3.3 Free energy profile for reductive elimination and CO_2 extrusion. Energy in kcal/mol.

Although the $[CpRh(OAc)_2]$ mechanism is discarded for the general reaction conditions with $[Cu(OAc)_2]_2$, this active species can be effectively formed if AgOAc is used as an oxidant because Ag can efficiently trap the Cl^- from the rhodium precursor. For this reason, the formation of the naphthalene product from the rodacycle intermediate **12** was also investigated (Figure 3.4). Again, two possible isomers can be formed after alkyne coordination, **13** and **13'**. Now, the energy difference between them is even higher (4.7 kcal/mol). The associated transition states **TS 13-14** and **TS 13'-14'** keep this trend with an energy difference of 7.0 kcal/mol, suggesting that only final isomer **4** will be formed selectively with the phenyl groups in positions 2 and 3 of the naphthalene, which is consistent with the observed product when formed (Table 3.4 entry 2 for example).

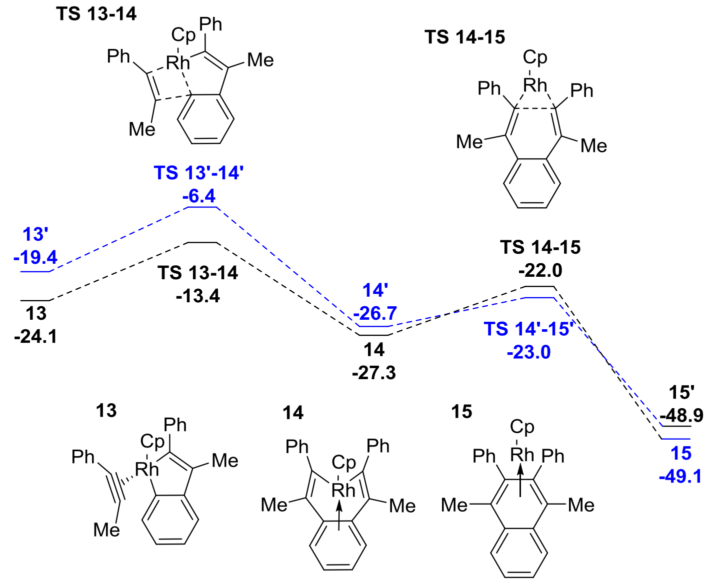

Figure 3.4 Free energy profile for naphthalene formation from 5-member rodacycle **13**. The major isomer is depicted in black and the minor isomer in blue (rotating alkyne 180°). Energy in kcal/mol.

Finally, when both alkynes have been inserted, the reductive elimination step yields Rh(I)-naphthalene compounds **15** and **15'**. This step is both kinetically and thermodynamically very favorable and it does not affect the regioselectivity of the product formation, even if the barrier for 2,4-methyl-1,3-phenylnaphthalene is slightly lower (by 1.0 kcal/mol) than for 1,4-methyl-2,3-phenylnaphtalene, due to the steric hindrance between phenyl groups in the transition state. This pathway shows that after CO_2 extrusion, the formation of compound **4** is very rapid, with low barriers from **13** to **15**.

The active role of $[Cu(OAc)_2(H_2O)]_2$ on the catalytic cycle

Bearing in mind that the oxidant has a strong effect in the chemoselectivity of the reaction, we considered including explicitly copper(II) diacetate dimer along the catalytic pathway. In the presence of a non-coordinating solvent (*o*-xylene), the dimeric copper species is the most stable form of the complex (8.9 kcal/mol more stable). It has a similar structure to that in the solid state.[79] It is well known that $[Cu(OAc)_2]_2$ has magnetic properties and depending on the temperature it can be a singlet, an open-shell singlet or a triplet. We evaluated the relative stability of the three electronic states in the reductive elimination process (see section 3.2 for details), and according to the results, we decided to maintain the triplet state along our computed reaction pathway.

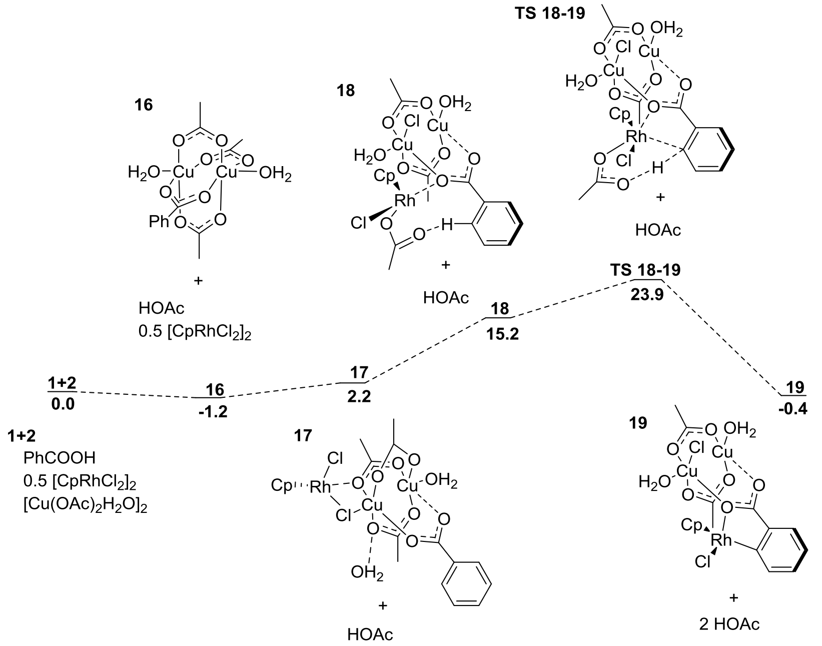

Figure 3.5 Free energy profile of Rh/Cu cooperative C-H activation. Energies in kcal/mol.

We firstly evaluated the C-H activation step in order to check if this step was feasible in a cooperative manner (Figure 3.5). The reaction starts with an exchange of one OAc^- of copper species by benzoate. Again, the relative acidity of both acetic and benzoic acid makes this step slightly exergonic by -1.2 kcal/mol. Then, [$CpRhCl_2$] coordinates the system through the apical position of copper and one oxygen of the cooper dimer interacts strongly with the rhodium vacancy forming intermediate **17**. These two steps and almost thermoneutral indicating that this approach makes more sense than assuming directly [$CpRh(OAc)_2$] as active species. Afterward, an acetate ligand is transferred from copper diacetate to the rhodium center in exchange for a chloride ligand. The resulting intermediate **18** has the proper geometry to activate the *ortho*-C-H bond of benzoic acid. Finally, Rh(III) activates C-H bond and it is deprotonated by an acetate assisted concerted metallation-deprotonation transition state forming the rodacycle intermediate **19**. Critically, the overall barrier of **TS 18-19** is 23.9 kcal/mol, 3.9 kcal/mol lower than **TS 7-8** (Figure 3.1). This confirms the idea of the non-innocent behavior of oxidant in the catalytic cycle.

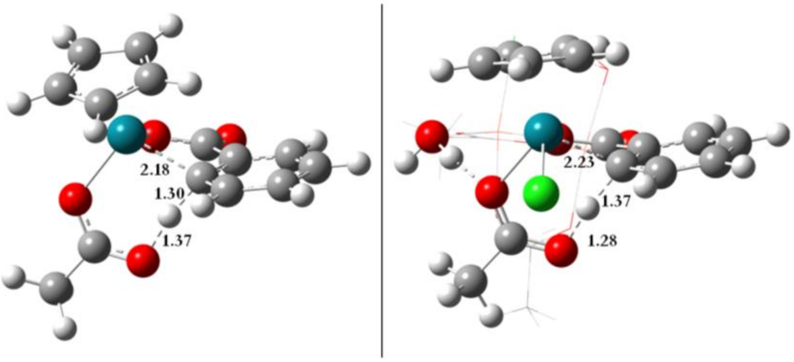

Figure 3.6 3D structures of **TS 7-8 (left)** and **TS 18-19** (right, copper dimer is depicted in wireframe for clarity). Bond lengths in Å.

In order to analyze both competing transition states in detail, 3D structures are shown in Figure 3.6. Although they share similarities in the C-H---Rh---OAc scaffold, the C-H bond is more activated in the Rh/Cu cooperative transition state, with a bond distance of 1.37 Å respect to 1.30 Å in **TS 7-8**. Interestingly, Rh-C bond is longer in the cooperative system, probably due to the coordination sphere of Rh, with three strong interactions (Cl, OAc and C) and one weak interaction with the oxygen of OBz (at 3.00 Å). On the contrary, the rhodium center in **TS 7-8** is only three-coordinated forming stronger interaction with *ortho* carbon. These facts decrease the free energy despite the entropic penalty of bringing an extra fragment into the system.

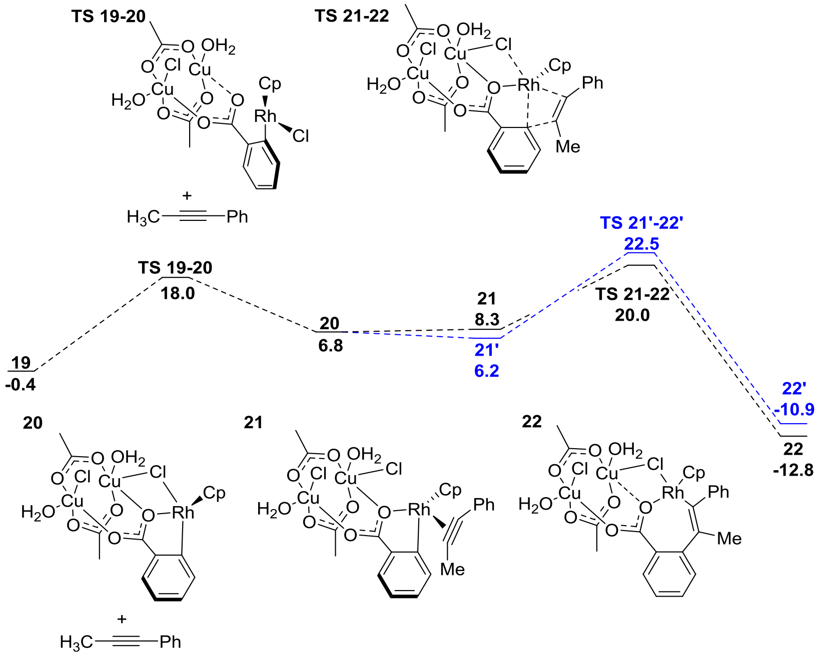

Figure 3.7 Free energy profile of Rh/Cu cooperative alkyne insertion. Energies in kcal/mol. Main pathway in black and minor pathway in blue (rotating alkyne 180º).

Following the formation of rodacycle **19**, isomerization by dihedral rotation occurs in order to form a chloride bridge between the rhodium and copper centers. This step is needed because in intermediate **19,** the adjacent Rh and Cu are fully saturated and therefore, there is no space for alkyne coordination. The rotation around the dihedral angle has a barrier of 18.4 kcal/mol. This value is quite high due to the breaking of both the Rh-O bond and the resonance between the phenyl and carboxylate groups. The resulting product **20** can transfer the Cl$^-$ bridge to copper, leaving space for the alkyne to enter into the coordination sphere. Analogously to what happened in the rhodium-alone pathway, 1-phenyl-1-propyne can be attached in two different ways, with the phenyl group pointing away from (**21**) or towards the benzoic aromatic ring (**21'**). This time, the latter is more stable by 2.1 kcal/mol, as the phenyl group of alkyne is closer to copper dimer in **21**. Yet, the energy difference between the associated transition states is reversed and in good agreement with the experimental outcome of the reaction (93% of **3** and 7% of **3'**). According to the calculated mechanism, $\Delta\Delta G^\ddagger$ is equal to 2.5 kcal/mol and it corresponds to a predicted ratio of 96:4 of **3** and **3'** respectively. Both pathways yield irreversibly 7-member ring rodacycles **22** and **22'**, which are very stable due to the reformation of the chloride bridge again.

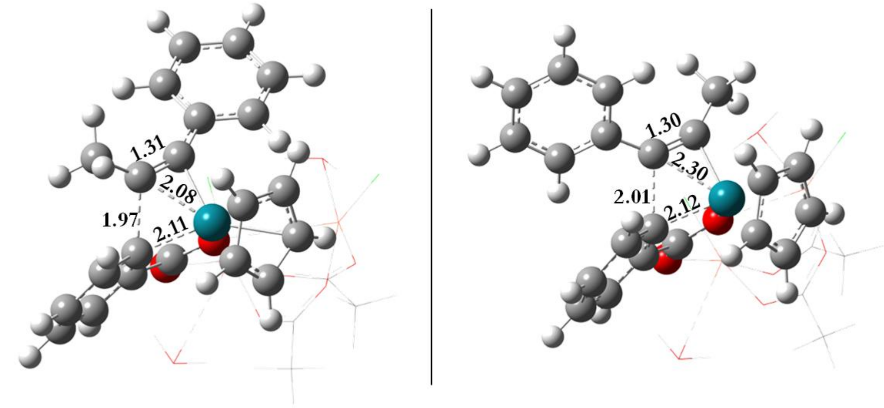

Figure 3.8 3D structures of **TS 21-22** (left) and **TS 21'-22'** (right). The copper dimer fragment is depicted in wireframe for clarity. Bond lengths in Å.

Looking into the 3D structures of the triple bond insertion transition states (Figure 3.8), we see that the phenyl group of alkyne is also the key to understand the selectivity. The rigid conformation of alkyne during the insertion blocks the π-π stacking between both phenyl rings, that are almost perpendicular in **TS 21'-22'**. The structure of this TS is very deformed, the week interaction between the β-alkyne carbon and the Rh center causes the energy barrier to increase. In contrast, **TS 21-22** is much less strained and the interaction between alkyne and Rh-C bond is stronger (2.11 Å), In addition, the alkyne is more activated in this isomer, with the C-C bond formation at 1.97 Å and a strong interaction between both alkyne carbon atoms and rhodium. All of these differences explain the stability of **TS 21-22** respect to **TS 21'-22'**.

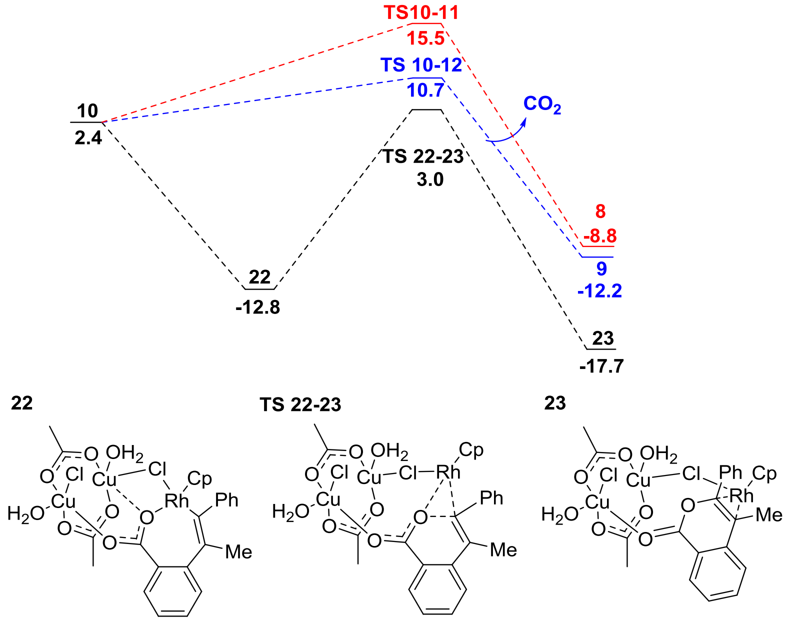

Figure 3.9 Free energy profile of Rh/Cu cooperative reductive elimination and comparison with [CpRh(OAc)$_2$] pathway (reductive elimination in red and CO_2 extrusion in blue). Energies in kcal/mol.

Once the alkyne has been inserted into Rh-C bond, intermediate **22** can evolve to the isocoumarin product formation through reductive elimination (Figure 3.9). This step defines the chemoselectivity of the reaction because it is irreversible. The cooperative pathway has a barrier of 15.8 kcal/mol (**TS 22-23**), due to the stabilization of the intermediate **22** respect to **10**. More significantly, the energy of the cooperative transition state is lower than that of the [CpRh(OAc)$_2$] pathway transition states **TS 10-12** and **TS 10-11** by more than 7.0 kcal/mol, explaining the observed selectivity since only isocoumarin product is obtained experimentally when 1-phenyl-1-propyne is used as reactant. Moreover, the

CO_2 extrusion pathway is blocked in the cooperative pathway because there is a direct interaction between one of the benzoate oxygen atoms and one copper of the dimer. Also, the chloride bridge between Rh and Cu prevents the rhodium attack to the benzoic acid *ipso* carbon and stabilizes the structure favoring the electronic connection between metal centers. Additionally, intermediate **23** is also more stable than the related compounds **8** and **9**. We also calculated this step in the open-shell singlet and close-shell singlet electronic structures but both barriers were higher in energy by 1.1 and 5.5 kcal/mol, respectively.

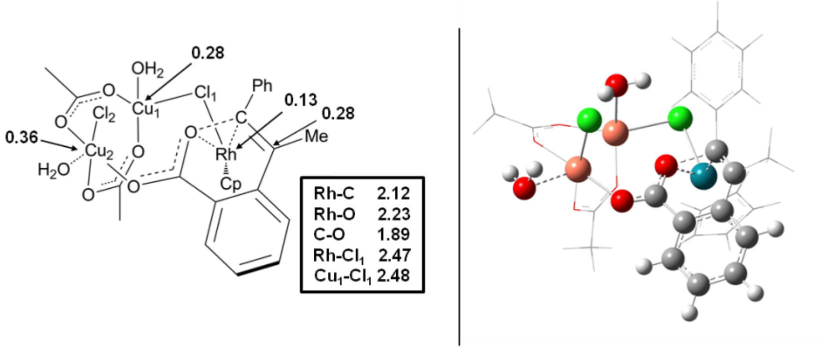

Figure 3.10 Detailed 2D structure with spin densities (on the draw) and relevant bond lengths (in inset) and the corresponding 3D structure of **TS 22-23**.

When **TS 22-23** is analyzed in detail (Figure 3.10), spin densities confirms that the two electrons released from the organic moiety do not go directly to the rhodium center (reducing Rh(III) to Rh(I)). Instead, the rhodium center has 0.13 spin density, which may be indicative of the formation of Rh(II). This is noteworthy, as Rh(II) has not been proposed before in similar reactions. At the same time, copper centers are also reduced, confirming collaboration between different metals in the transition state. The bridging position of chloride, which is at the same distance from Rh (2.47 Å) and Cu (2.48 Å), allows this electron transfer from the organic part to the copper centers. In the TS, β-carbon has 0.28 spin density, demonstrating that the organic moiety is opening its closed-shell electronic structure. This unprecedented feature can define this step as a cooperative reductive elimination (CRE). Although substantially different, the metal cooperation and the additive effect are reminiscent of previous theoretical study,[80,81] demonstrating that reactions are usually more complicated than they seem to be, especially when they are very sensitive to additives, such as the oxidant in our case.

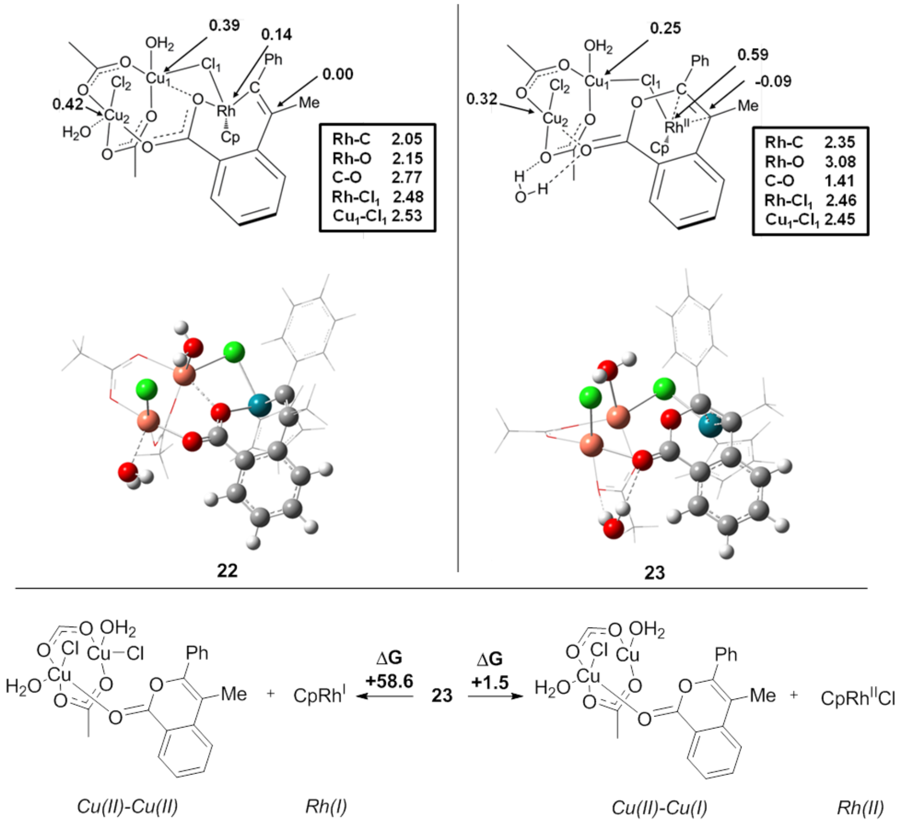

Figure 3.11 Detailed 2D structures with spin densities (on the draw) and relevant bond lengths (in inset) and the corresponding 3D structures of **22** and **23**. (Top) Separation of intermediate **23** in fragments with different electronic structures (Bottom).

The large delocalization along acetates and chlorides ligands makes the overall spin distribution complicated to study, especially in the transition state. For this reason, we made the same analysis for intermediates **22** and **23**. Figure 3.11 (top) describes the spin density and the relevant bond distances before and after reductive elimination. Intermediate **22** shows higher spin density than **TS 22-23** in the copper dimer, but also some delocalization on the rhodium center. The organic moiety is also in closed-shell electronic structure, since Rh-O (2.05 Å) and Rh-C (2.15 Å) bond are largely unchanged. However, after C-O bond formation, intermediate **23** is clearly a Rh(II) species, with an spin density on rhodium center of 0.59, indicating the one electron reduction of this metal after the cooperative reductive elimination. Concurrently, one electron reduces the copper dimer, decreasing the electron spin density considerably from 0.81 to 0.57. Unfortunately, the delocalization along the copper ligands makes it difficult to assign with certainty the Cu(I) or Cu(II) electronic distribution of each copper, but the trend is clear. This reduction of copper is also shown in the shortening of Cu-Cl bond (from 2.53 Å in **22** to 2.45 Å in **23**). In order to confirm the electronic structure of rhodium in complex **23**, we carried out a computational experiment. We separated the rhodium fragment from this intermediate in two different ways, as CpRh(I) and as CpRh(II)Cl. The free energies associated with this process are 1.5 and 58.6 kcal/mol respectively, conclusively demonstrating for Rh(II) formation in the CRE mechanism.

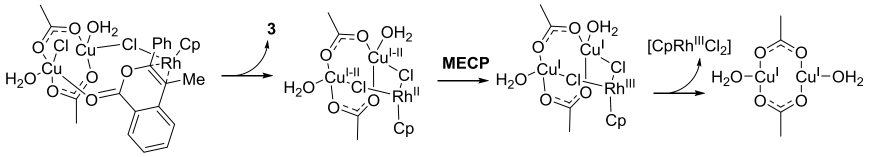

23
-17.7

$24_{Triplet}$
-29.0

$24_{Singlet}$
-33.1

25
-38.0

Figure 3.12 Free energies of regeneration of Rh(III) initial catalyst from **23**. Energies in kcal/mol.

The last step, which regenerates the catalyst, is the release of isocoumarin **3** from intermediate **23** (Figure 3.12) forming species **24**, in the triplet state. This species has two unpaired electrons, one on the copper centers and the other on rhodium. However, the close-shell singlet state is lower in energy by 4.1 kcal/mol, indicating that the formation of

Rh(III) and Cu(I)-Cu(I) system is favorable. We did not compute the minimum energy crossing point (MECP) because the energy and the structure of both systems are close enough to assume this step to be easily affordable under reaction conditions. Finally, [CpRh(III)Cl_2] can be separated exergonically from the reduced copper dimer, to restart the catalytic cycle. $[Cu(OAc)(H_2O)]_2$ is produced as side product, which can be in principle reoxidized to copper(II) diacetate with molecular oxygen.

$[Ag(OAc)]_2$ influence on the chemoselectivity

The formation of isocoumarin by the oxidative coupling of benzoic acid and alkyne is successfully explained when rhodium and copper are used in the reaction. However, if silver acetate is used, the reaction yields a mixture of both products, the isocoumarin and the naphthalene (Table 3.4, entry 2). In order to cover all the possibilities of the reaction mechanism and to have a useful overview of the oxidant effect in oxidative couplings, which can help for the development of new reaction in the future, we aim to understand why silver produces mixtures. We keep 1-phenyl-1-propine as the reactant in order to facilitate the comparison between different pathways, although 1-2-diphenylethyne was the alkyne used in silver acetate experiments.

The main differences between both oxidants, silver and copper acetates, is that silver can effectively act as a chloride abstractor, generating [CpRh$(OAc)_2$] in the reaction media. However, silver acetate is used in large excess and after rhodium precursor activation, it should have other effects in the catalytic cycle. We know that because when we studied the catalytic cycle of [CpRh$(OAc)_2$] (red and blue pathways of Figure 3.13), the energy difference between reductive elimination and CO_2 extrusion transition states (of 4.8 kcal/mol) implies that only naphthalene derivative product would be observed, which is in disagreement with the experimental outcome (about 40:60 of naphthalene-isocoumarin ratio).

For this reason, we analyzed the chemoselectivity determining step including the silver acetate dimer in the calculations (Figure 3.13).

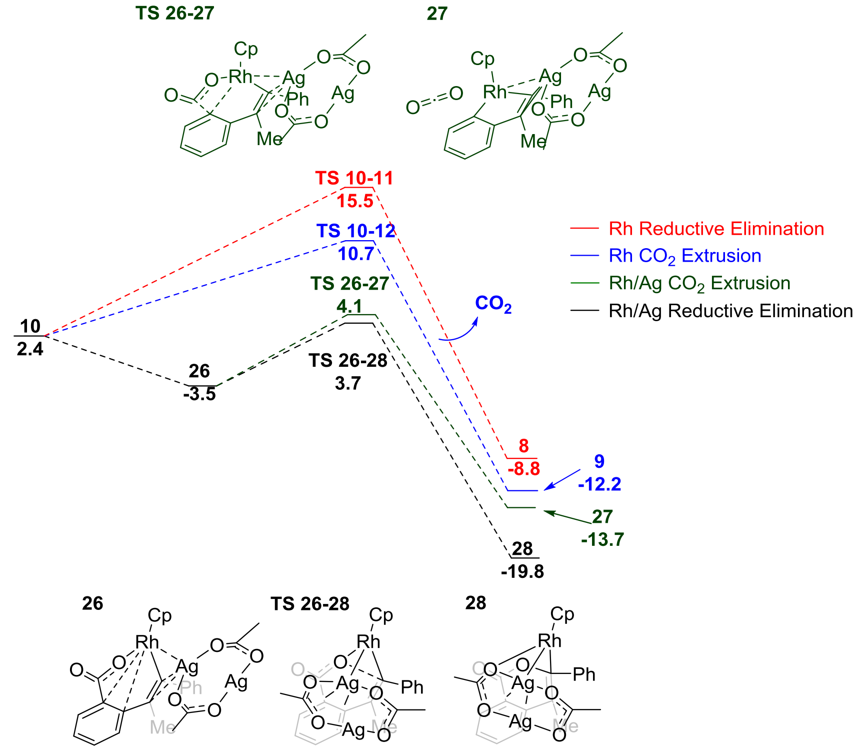

Figure 3.13 Free energy profile of Rh/Ag cooperative reductive elimination and comparison with [CpRh(OAc)$_2$] pathway. Energies in kcal/mol.

Interestingly, the planar structure of the silver acetate dimer,[82] which is 31.1 kcal/mol more stable than the monomer structure, allows the calculation of both pathways. This differs considerably from the Cu-cooperative pathway, where the 3D structure of copper dimer blocked the CO_2 extrusion. The cooperative reductive elimination (in black) is again the most stable pathway, at 3.7 kcal/mol. In this transition state, there is a strong Rh-Ag interaction, suggesting the reduction of silver during the transition state. Nevertheless, the CO_2 extrusion pathway is also lower in energy than Rh-alone pathways, at 4.1 kcal/mol (in green). The energy difference between both transition states in only 0.4 kcal/mol, which is associated with a predicted ratio of 61:39 (at 180ºC), isocoumarin and naphthalene respectively. Even though different alkyne is used in the experiment, the observed product ratio (40:60) is close to the predicted one, considering that the alkyne hardly affects the relative proportion of both chemoselective products.

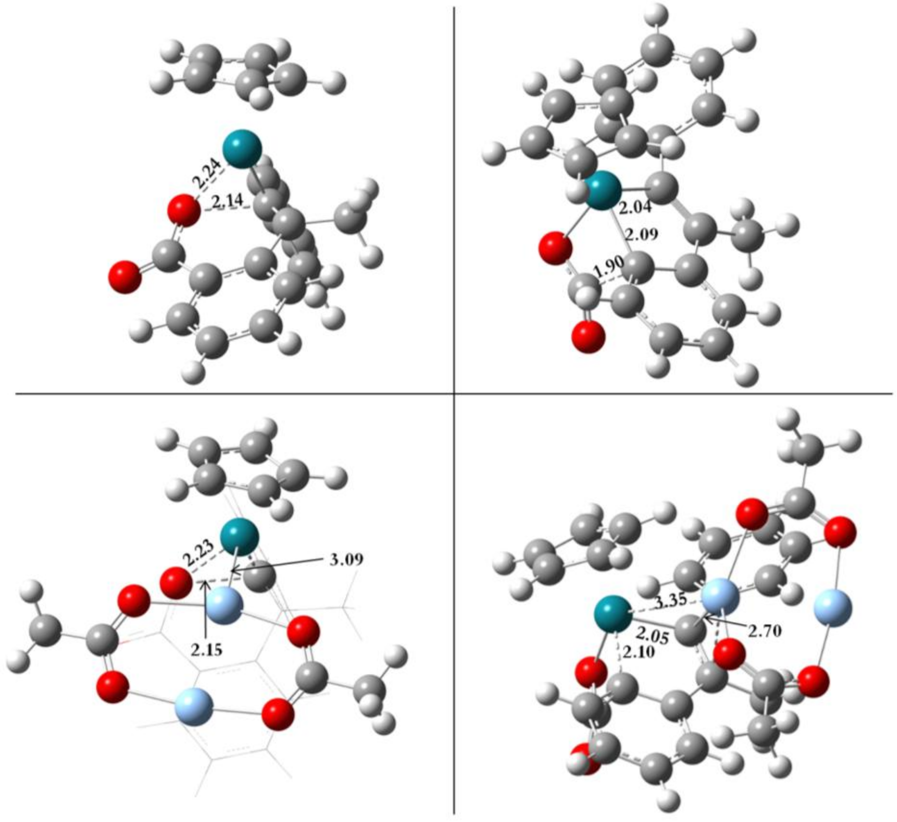

Figure 3.14. 3D views of **TS 10-11** (top, left), **TS 10-12** (top, right), TS **26-28** (bottom, left), and **TS 26-27** (bottom, right). Relevant bond distanced are depicted in Å.

Finally, we have a closer look to the transition state structures (Figure 3.14). **TS 10-11** and **TS 10-12** are structurally very different, the CO_2 extrusion is more stable probably due to the saturation of the rhodium valence in the transition state (with two Rh-C and one Rh-O bonds). With regard to the silver transition states, both **TS 26-28** and **TS 26-27** are saturated at the rhodium center, and in the case of **TS-26-28**, there is a strong Rh-Ag interaction at 3.09 Å. On the contrary, the Rh-Ag interaction in **TS 26-27** is much weaker, at 3.35 Å, due to the crowded situation of rhodium center. Additionally, silver interacts with the double bond of the organic part as a Lewis acid (2.70 Å). Comparing the cooperative pathways with the Rh-catalyzed pathways, silver can substantially stabilize both, elongating the Rh-C and Rh-O interactions by 0.01 Å approximately. Therefore, all the calculations suggest that the cooperative pathway is also the most plausible when silver acetate is used as oxidant.

Conclusion

Oxidative couplings have emerged as an effective and sustainable way to build complexity in organic synthesis. The mechanism for these reactions is puzzling, as usually one metal is used as catalyst and another metal as oxidant. For this reason, developing a wide understanding of reaction mechanisms is the key to promote the rational design of new reactions.

In this context, we have used Density Functional Theory (DFT) calculations to consider the reaction mechanism of one of the seminal examples of rhodium(III)-catalyzed oxidative coupling. In this specific case, benzoic acid and alkynes are combined to yield chemoselectively isocoumarins when copper(II) acetate is used as oxidant. In addition, when silver acetate acts as the oxidant, the reaction gives mixtures of isocoumarin and naphthalene derivatives. We fully explained the catalytic cycle and analyzed the chemoselectivity determining step without oxidant, with $[Cu(OAc)_2(H_2O)]_2$ and with $[Ag(OAc)]_2$. Moreover, this reaction is also regioselective regarding the alkyne insertion. Our model explains successfully this selectivity in terms of steric hindrance of phenyl group versus alkyl group. The catalytic cycle is summarized in Scheme 3.6.

Scheme 3.6 Catalytic cycle of Rh/Cu co-catalyzed oxidative coupling of benzoic acid and 1-phenyl-1-propyne.

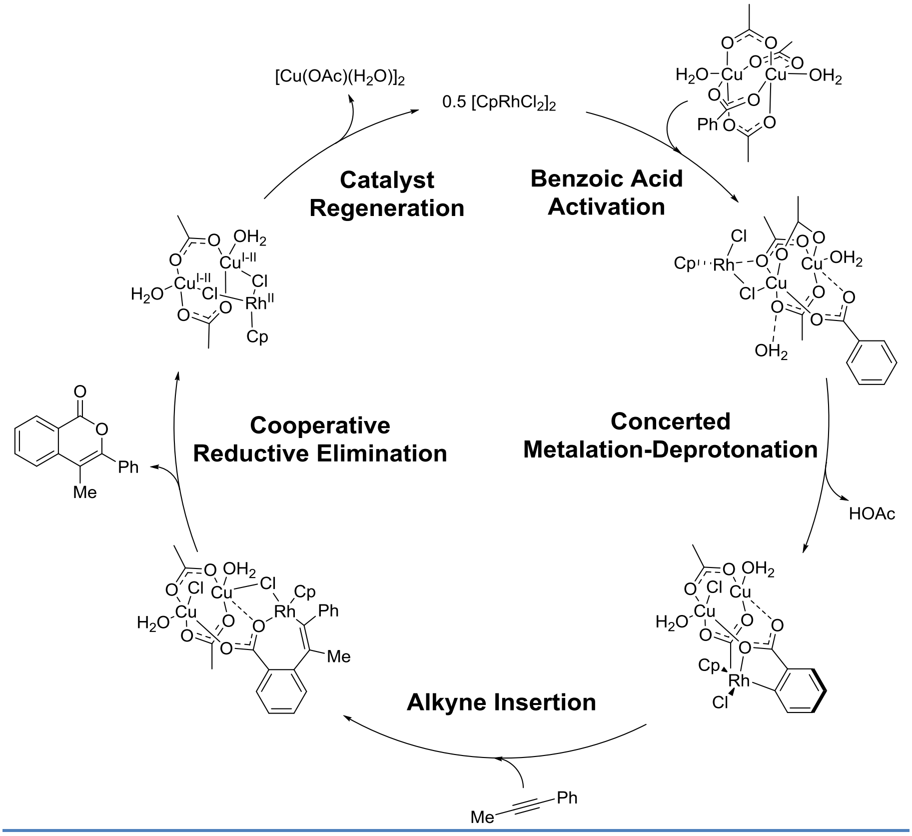

The results on the oxidant-dependent chemoselectivity have demonstrated that the cooperative effect between rhodium and copper (or silver) is essential to understand the isocoumarin formation. That is because Rh(III) is not reduced to Rh(I) as it had been proposed. On the contrary, the cooperation between both metals allows the one electron reduction of rhodium (forming Rh(II)) while the copper dimer can receive the other electron released during the reductive elimination (Scheme 3.7, top). This fact contrasts with the classical Rh(III)-Rh(I)-Rh(III) catalytic cycle (Scheme 3.7, bottom). Furthermore, in this specific reaction, the CO_2 extrusion pathway (which leads to naphthalene formation) is blocked when copper is the oxidant, due to the tridimensional structure of the dimer. It explains the very high observed selectivity. The use of silver acetate, which has planar structure, can stabilize both pathways, the reductive elimination and the CO_2 extrusion, giving reaction mixtures.

Scheme 3.7 Comparison between Rh/Cu cooperative reductive elimination (top) and the conventional reductive elimination plus reoxidation (bottom).

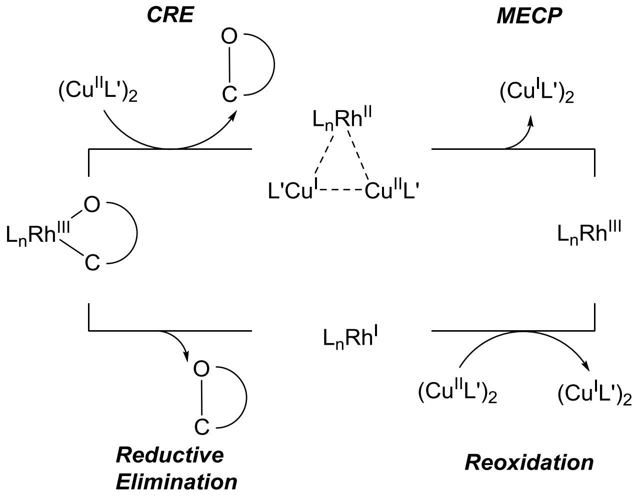

We believed that this theoretical study will support the rational design of new oxidative couplings, especially those in which the oxidant can play an active role in the selectivity. In addition, our calculations show the cooperation between different metals in the reductive elimination, facilitating the electron transfer and lowering the overall reaction barriers.

3.4 Oxidative Homocoupling of Carbazole by O_2 Co-Catalyzed by Ruthenium and Copper Complexes

Reaction overview

Following our interest in oxidative coupling reactions, we shifted our focus to a dehydrogenative C-N bond formation catalyzed by ruthenium and copper species using oxygen as final oxidant.

Scheme 3.8 Dehydrogenative homocoupling of carbazole *via* C-N bond formation catalyzed by ruthenium and copper under air.[83]

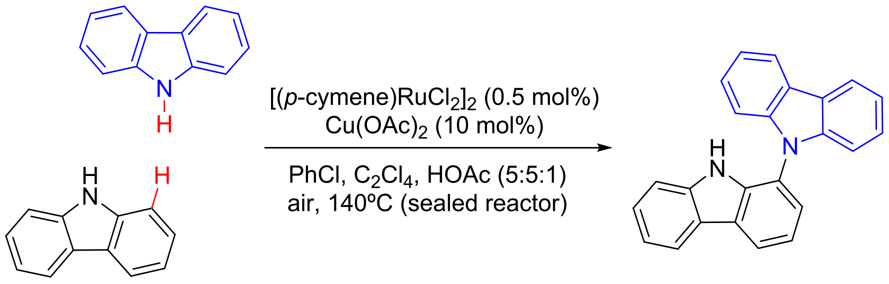

This reaction was reported in 2013 by Patureau and co-workers[83] and we decided, in conjunction with Prof. Patureau, to start a collaboration to analyze the reaction mechanism. The synthetic methodology yields selectively the homocoupling of carbazoles at carbon one although C1, C2 and C3 are activated through C-H bond activation (Scheme 3.8). This reaction fulfills highly desired parameters in an organic reaction: it does not require prefunctionalization of the substrate, the atom economy is almost ideal (only water is produced as by-product) and it is very selective towards the formation of the main product. Moreover, the catalysts loading is very low in ruthenium (1 mol%) and quite low in copper (10 mol%).

Regarding reaction mechanism, the authors made a remarkable effort to clarify experimentally the C-H activation mechanism and the kinetic order of the catalysts. Interestingly, deuterium scrambling experiments (Figure 3.15) demonstrated that C-H activation step is reversible under reaction conditions and that not only the C1 center of carbazole is activated; C2 and C3 are also deuterated in high yields (18-44 %) although no C2 or C3 coupling products are formed during the reaction. This fact suggests that the rate determining step of the reaction is the reductive elimination. Furthermore, the combination of ruthenium catalyst, copper(II) diacetate and oxygen is required for the C-H activation, suggesting that molecular oxygen is involved in the formation of the active catalytic species.

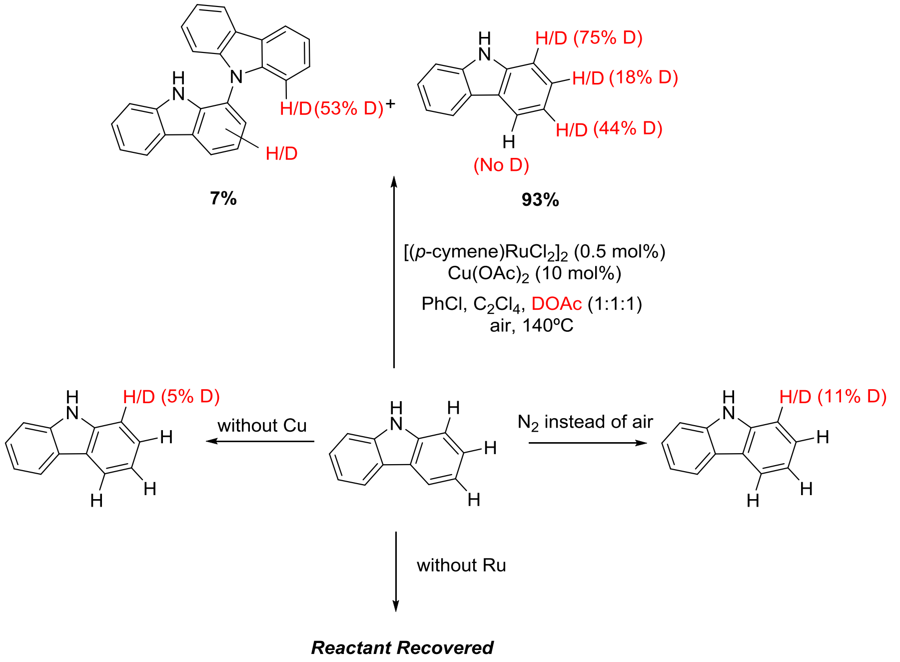

Figure 3.15. Deuterium scrambling experiments on C-N homocoupling of carbazoles. Percentage of deuterium incorporation in red.

Probably, the most intriguing aspect of this reaction is the kinetic profile. Under catalytic conditions ([Ru] >> [Cu]), the reaction has a kinetic order of 0.7 for ruthenium and zero for copper. The non-integer value for ruthenium can be explained by the ruthenium dimer dissociation-association equilibrium, and the zero order for copper can be explained by its high excess (10:1) with respect to ruthenium in the original reaction conditions. As the presence of the copper co-catalyst is mandatory for the reaction to take place, reactivity-based Job plot experiment were carried out by changing the relative concentrations of both copper and ruthenium species. This experiment provided valuable information about the kinetic orders when one metal is in high concentrations with respect to the other and allowed to identify the optimal ratio between both metals. Interestingly, when ruthenium is in high concentration (pseudo-zero order), the kinetic order in copper is about 1.6, which is surprisingly higher than 1, indicating the presence of more than 1 copper center in the rate determining step. This is confirmed by the optimal ratio between both metals, 1:2 of Ru/Cu respectively. It indicates that one ruthenium and two coppers are involved in the rate limiting step. This fact is hints to the Cooperative Reductive Elimination described in section 3.3, in which one rhodium and two copper centers were involved in the chemoselectivity determining step.

Herein, we calculated the reaction mechanism for the simplest carbazole (see Scheme 3.8). We also replaced p-cymene by benzene as ligand in the ruthenium catalyst to reduce the computational cost and to avoid conformational issues. In the following figures, acetate bridges between copper centers are represented with a line to improve the clarity in the draws.

The full catalytic cycle

The reaction mechanism of the dehydrogenative coupling of carbazoles is very complex because two catalyst and molecular oxygen are needed from the beginning of the catalytic cycle. This has been demonstrated experimentally through deuterium scrambling experiments (Figure 3.15). For this reason, we only considered the possibilities in which all species are involved. The catalytic cycle can be divided in four steps, described separately across this subsection.

Firstly, one molecule of carbazole is activated by copper(II) diacetate (Figure 3.16, left). The N-H bond is quite easy to deprotonate due to the delocalization of electron density along the aromatic cycles. One acetate gives space for the substrate to coordinate, forming intermediate **30**, with an energy increase of 3.4 kcal/mol. The cleavage of the N-H bond occurs easily in this intermediate *via* an acetate assisted deprotonation with a barrier of only 2.1 kcal/mol. Interestingly, once the carbazole is deprotonated (**31**), one electron is transferred from the aromatic ring to the copper centers.

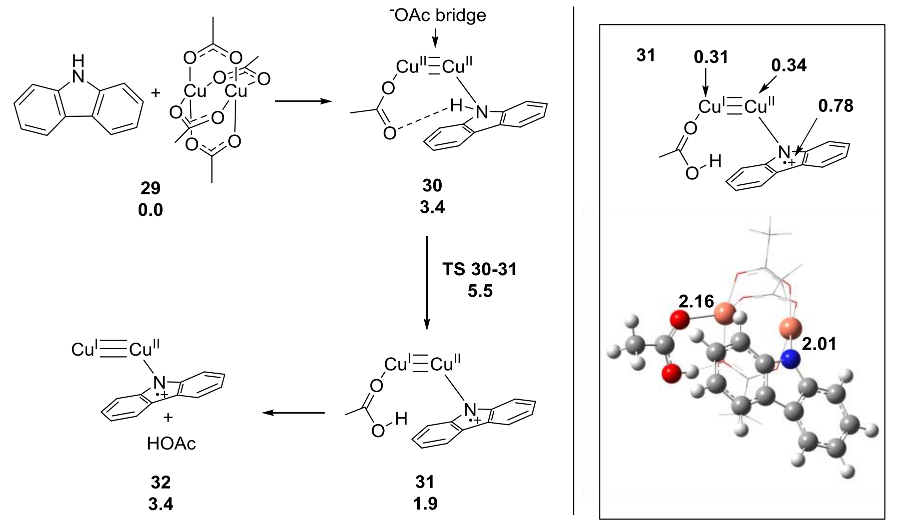

Figure 3.16. Free energy profile of N-H activation of carbazole by [Cu(OAc)$_2$]$_2$. Energy in kcal/mol (left). 3D structure of intermediate **31** (right). Spin densities are showed above and relevant bond distances in Å are showed below.

Analyzing the electronic structure of this intermediate (Figure 3.16, right), the spin density located on the aromatic ring is near 1, indicating the oxidation of the ring. In addition, the spin densities on the two copper centers decrease to 0.31 and 0.34, with some of spin density delocalized along the acetate ligands. In the next step, the acetic acid is lost in the media, leading to intermediate **32**, with an overall energy increase of 3.4 kcal/mol.

Once the first carbazole molecule had been activated, we explored the more challenging C-H activation of the second carbazole (Figure 4.17). Considering that oxygen, ruthenium and copper must be present in this step, we took into account different possibilities such as copper-oxygen interaction, or the direct oxidation of the ruthenium precursor. The last option was the most likely because the oxidation of [(C$_6$H$_6$)RuCl$_2$] by oxygen to yield the corresponding Ru(IV) structure **33** is exergonic by 3.7 kcal/mol. Although we did not focus on the kinetic profile of this specific step, Ru(IV)=O species are well-established in the literature.[84] Moreover, there are precedents of molecular dioxygen breaking by a metal dimmer.[85] Thus, we considered the participation of the resulting species on the following steps. Interestingly, the oxidation of the catalyst occurs at the beginning of the catalytic cycle, in agreement with the experimental findings. This species can interact with the copper dimer forming adduct **34**. The oxo bridge between Ru and Cu can be protonated by acetic acid in the media, resulting in intermediate **35**.

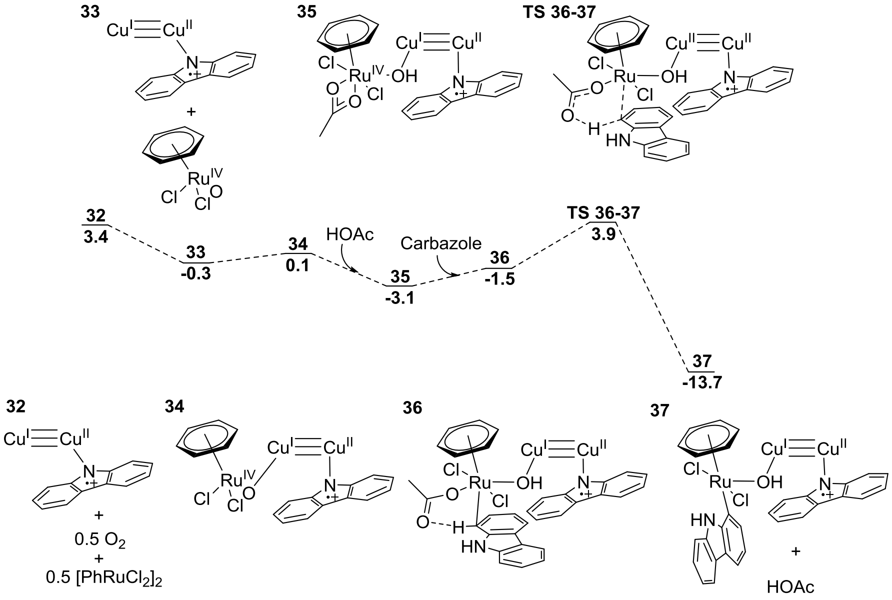

Figure 3.17. Free energy profile of cooperative C-H activation of carbazole by ruthenium and copper under molecular oxygen. Energy in kcal/mol.

Then, the second carbazole molecule is coordinated to ruthenium center forming an interaction with the C-H bond of carbazole at C1. Intermediate **36** is activated towards the C-H activation, with an associated transition state at 5.4 kcal/mol. The formation of Ru-C bond is exergonic, producing the stable intermediate **37** at -13.7 kcal/mol. Nevertheless, this step is reversible (the following step has a higher barrier), in agreement with experimental observation. In the next subsection, the selectivity of C-H activation will be discussed in detail.

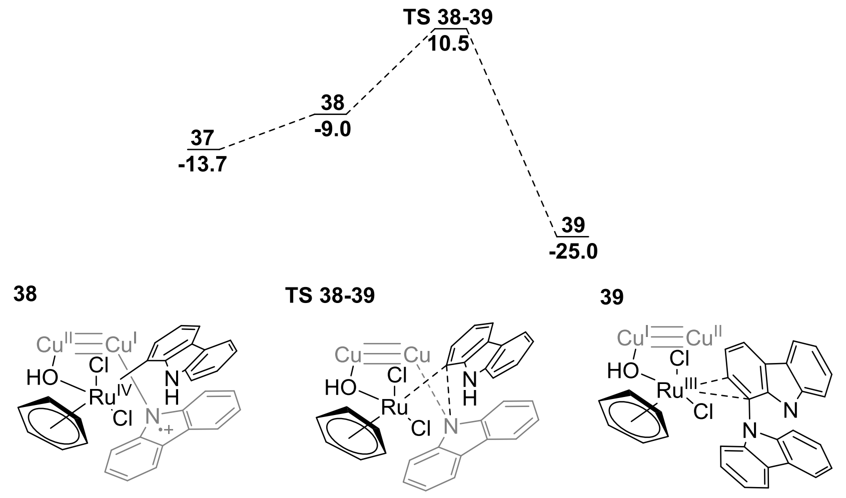

Figure 3.18. Free energy profile of cooperative reductive elimination of C-N coupling product promoted by ruthenium and copper. Energy in kcal/mol.

After C-H and N-H activation, intermediate **37** can isomerize to intermediate **38** in which the carbazole groups are pointing to each other. Attending to the spin densities, the carbazole attached to copper is partially oxidized and the copper partially reduced (Figure 3.18). During the transition state **TS 38-39**, there is a large electronic reorganization, to form compound **39**, which is very stable (-25.0 kcal/mol) and makes this step irreversible. As in section 3.3, this cooperative reductive elimination implies the release of two electrons from the organic moiety, one of them goes to ruthenium and the other one to the copper dimer. Transition state **TS 38-39** is quite high in energy, with an overall barrier of 24.2 kcal/mol, being the rate determining step of the reaction mechanism. This is in agreement with experimental findings. In the next subsection, the selectivity of the reductive elimination only towards C1 functionalization will be discussed.

Finally, the homocoupling product is released to the media forming intermediate **40** (Figure 3.19). Then, acetic acid coordinates to the copper dimer exothermically, to form **41**. After electron reorganization, the initial ruthenium catalyst, $[(C_6H_6)RuCl_2]$ is liberated and the basic OH group on copper is protonated by the acetic acid to form water and acetate. Water formation is the driving force to close the catalytic cycle and this H_2O is released to close the copper dimer $[Cu(OAc)_2]_2$ with an overall energy liberation of 35.6 kcal/mol.

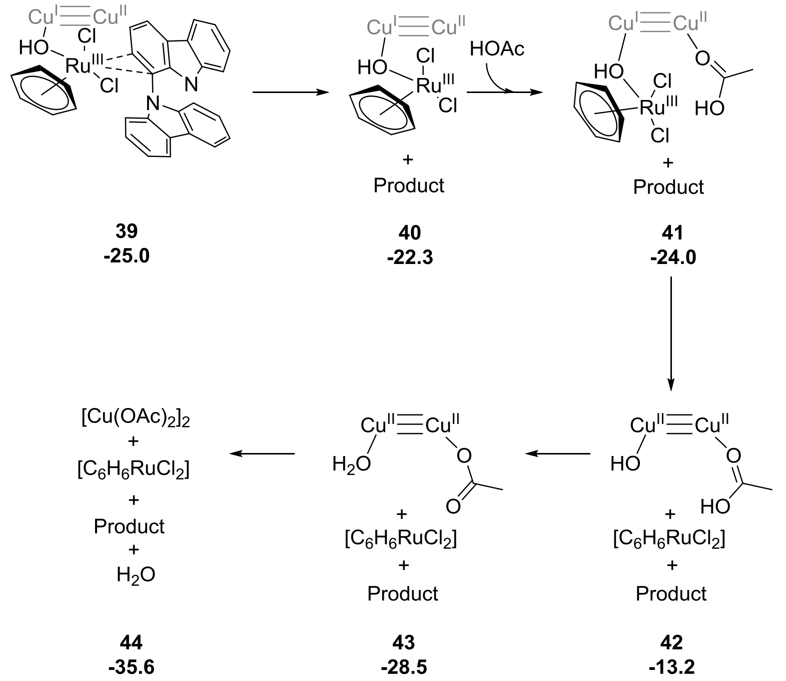

Figure 3.19. Regeneration of the catalytic cycle by copper-ruthenium electron transfer. Energy in kcal/mol.

Analyzing reaction selectivity

Once we calculated the catalytic cycle, we checked if the mechanism could explain the complex selectivity of the reaction. According to the experimental results, three carbazole C-H bonds are activated under reaction conditions, at position 1, 2 and 3. In addition, deuterium scrambling experiments (Figure 3.15) showed that the deuteration occurs easier according to the following order: C1 > C3 > C2 >> C4. Moreover, although three carbons can be activated, only the C1-coupling product is obtained, suggesting that the rate determining step is the reductive elimination and the barrier should be lower for C1 than for C2 or C3. For this reason, we calculated the transition states of C-H activation for the other carbons as well as the reductive elimination.

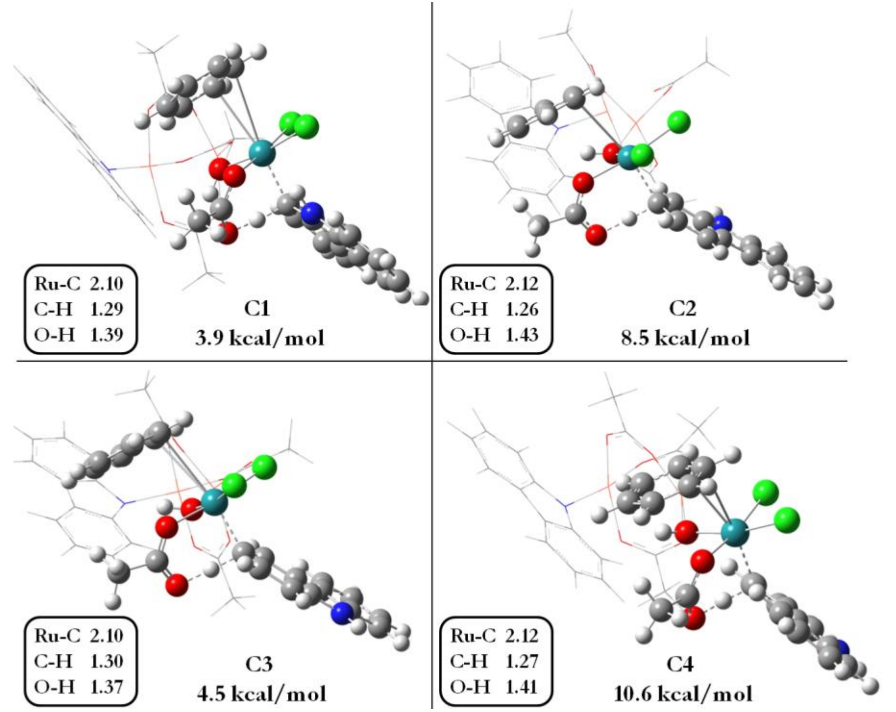

Figure 3.20. 3D views of the CMD C-H activation transition states (**TS 36-37**) of positions C1, C2, C3 and C4 of carbazole by cooperation of ruthenium and copper catalysts. The copper dimer fragment is in wireframe for clarity reasons. Bond distances are depicted in Å and energies in kcal/mol referred to the reactants.

Gratifyingly, the energies of the different C-H activation transition states are in very good agreement with the experimental observations (Figure 3.20). The C1 activation has the lowest energy at 3.9 kcal/mol (with respect to the reactants). C3 is also low in energy, at 4.5 kcal/mol, followed by C2, which is at 8.5 kcal/mol. Finally, C4 has the highest barrier at 10.6 kcal/mol. This barrier is even higher than the C1-reductive elimination (**TS 38-39**, 10.5 kcal/mol), explaining why C4 C-H activation is negligible. The 3D structures of these transition states show that the relative position of C-H bond during the activation is strongly related with the distortion of the system. C1 and C3 transition states have the shortest Ru-C bonds (2.10 Å), while C2 and C4 bond lengths increase up to 2.12 Å, showing a worse activation of the C-H bond. The same tendency is observed for C-H bond lengths while the contrary is true for O-H bonds, since the three interactions are strongly correlated in the transition state.

Finally, in order to explain the C1 selectivity for the C-N bond formation, we also calculated the cooperative reductive elimination of C2 and C3. Again, our model can explain successfully the experimental observation of the C1 selective amination. The barrier of **TS 38-39$_{C1}$** is 3.7 kcal/mol lower than **TS 38-39$_{C3}$** and 6.4 kcal/mol lower than **TS 38-39$_{C2}$**. These results are associated with the ratio of observed products of >99.8 % for C1 and <0.2% for C3+C2 products.

Alternative mechanism

The computational evaluation of the catalytic cycle was quite restricted by the experimental evidences about the participation of all the species since the C-H activation. We fulfill the explanation of these experiments with the mechanism that we proposed above. However, in order to be sure of our proposal, we also calculated other possible pathway that may fulfill these requirements. From intermediate **33**, it is possible to generate a ruthenium(III) complex that activates the C-H bond alone. This possibility is shown in the Figure 3.21.

The reduction of $[(C_6H_6)RuCl_2(O)]$ by chloride transfer to the copper dimer produces **45**, which is less stable by 6.1 kcal/mol. From here onwards, the coordination vacancy of Ru can be filled by acetic acid in the media, protonating the oxo group and generating **46**. Then, the carbazole is coordinated through the aromatic ring in order to activate the C-H bond. We explored the acetate assisted deprotonation (CMD transition state) and the OH^- mediated deprotonation. The energies of **TS 46-47$_{OAc}$** and **TS 46-47$_{OH}$** are 24.4 and 32.3 kcal/mol, respectively. If we compare these results with the Ru/Cu cooperative C-H activation (**TS 36-37**, at 3.9 kcal/mol), it is evident that this pathway is much hindered. In addition, the reductive elimination based on Ru(III) is also higher in energy, at 21.4 kcal/mol. For all of this, we discarded this alternative mechanism for the Ru/Cu co-catalyzed homocoupling of carbazoles.

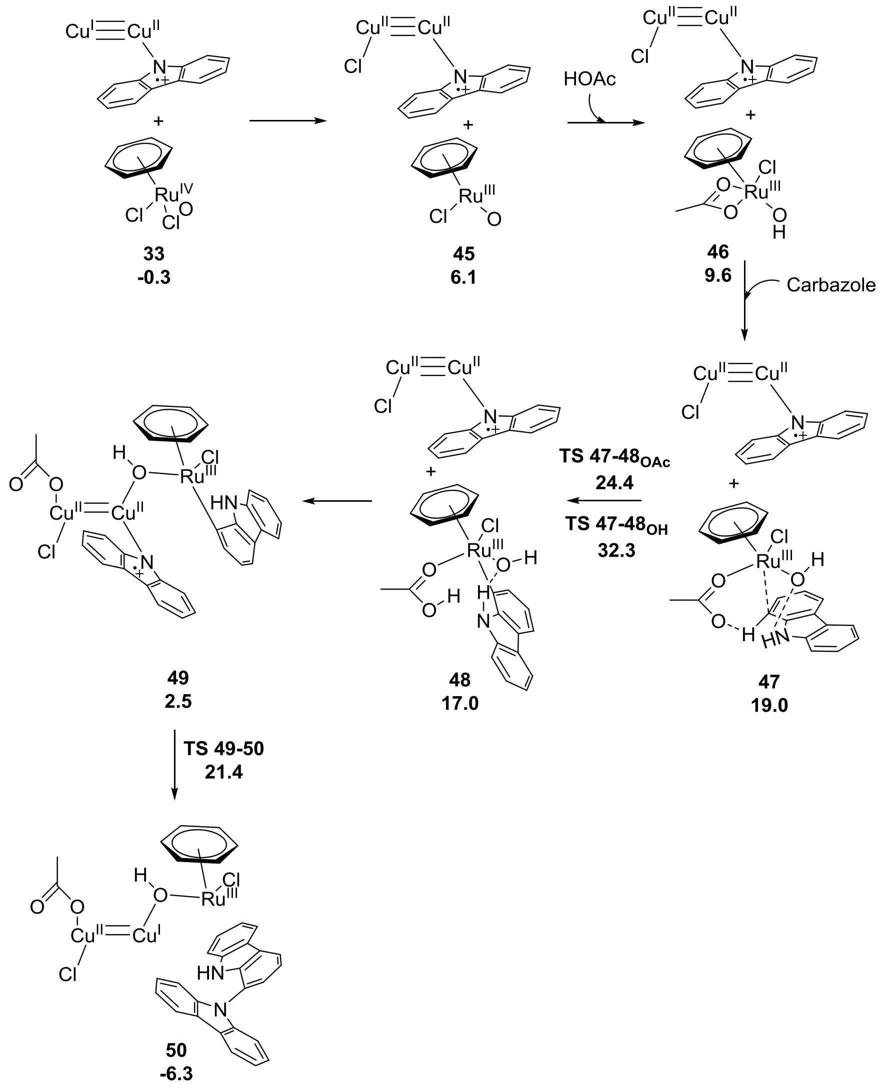

Figure 3.21 C-H activation and reductive elimination of Ru(III) based alternative mechanism. Free energies in kcal/mol.

Conclusion

The mechanism of dehydrogenative homocoupling of carbazoles co-catalyzed by ruthenium and copper under air has been successfully characterized by density functional theory calculations. As in section 3.3, the cooperation between two different transition metals, Cu and Ru in this case, is crucial to understanding the reactivity and the selectivity. In this case, we have demonstrated that C-H activation of carbazoles can be produced reversibly at different positions, in agreement with deuterium scrambling experiments, but only the cooperative reductive elimination at C1 position is productive towards the product, yielding selectively the C-N coupling.

Scheme 3.9 Catalytic cycle of Ru/Cu co-catalyzed dehydrogenative homocoupling of carbazole under air.

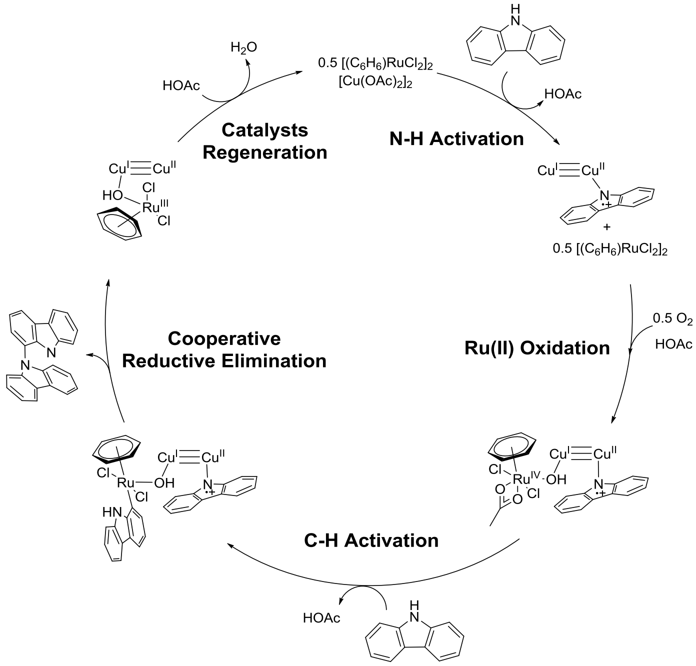

An overview of the catalytic cycle is shown in Scheme 3.9. The reaction starts with N-H activation of carbazole by copper(II) acetate dimer (N-H Activation). Then, oxygen can oxidize the initial ruthenium(II) catalyst to form the Ru(IV)-O moiety. Again, the external oxidant (O_2 in this case) takes part in the mechanism in an active way (Ru(II) Activation). From this point, ruthenium(IV) intermediate can interact with the copper dimer and can activate the carbazole *via* CMD transition state (C-H Activation). The product formation is achieved by the cooperative reductive elimination (CRE) between Ru and Cu dimer, which yields exclusively the homocoupling product at carbon one. Finally, the initial Cu and Ru catalysts are regenerated by protonation of the OH group, releasing only water as by-product. Our mechanistic description can also predict the activation of the other C-H bonds in agreement with deuteration experiments, showing that the rate of C-H activation concerning the carbon position is: C1 > C3 > C2 >> C4.

This complex mechanism expands our initial idea of additive cooperation in oxidative couplings and it could be useful for the development of new reactions. We are now collaborating actively with Prof. Patureau group to expand the scope of this reaction to other substrates based on *in silico* design.

3.5 References

[1] Nishihara, Y. *Applied Cross-Coupling Reactions*, 1st Edition, Springer-Verlag: Berlin, Germany, 2013.

[2] *"The Nobel Prize in Chemistry 2010"* web visited on*:* 31 May 2017. http://www.nobelprize.org/nobel_prizes/chemistry/laureates/2010/

[3] Li, C.-J. *Handbook of Green Chemistry*, Wiley-VCH: Weinheim, Germany, 2012; Vol. 7.

[4] Lei, A.; Shi, W.; Liu, C.; Liu. W.; Zhang, H.; He, C. *Oxidative Cross-Coupling Reactions*, 1st Edition; Wiley-VCH: Weinheim, Germany, 2017.

[5] Moragas, T.; Correa, A.; Martin, R. *Chem. Eur. J.* **2014**, *20*, 8242-8258.

[6] De Meijere, A.; Diederich, F. *Metal-Catalyzed Cross-Coupling Reactions*, 2nd Edition; Wiley-VCH: Weinheim, Germany, 2004.

[7] Zhang, G.; Yang, L.; Wang, Y.; Xie, Y.; Huang, H. *J. Am. Chem. Soc.* **2013**, *135*, 8850-8853.

[8] Warratz, S.; Kornhaaβ, C.; Cajaraville, A.; Niepötter, B.; Stalke, D.; Ackermann, L. *Angew. Chem. Int. Ed.* **2015**, 54, 5513-5517.

[9] Shi, Z.; Zhang, C.; Li, S.; Pan, D.; Ding, S.; Cui, Y.; Jiao, N. *Angew. Chem. Int. Ed.* **2009**, *48*, 4572-4576.

[10] Labinger, J. A.; Bercaw, J. E. *Nature* **2002**, *417*, 507-514.

[11] Bergman, R. G. *Nature* **2007**, *446*, 391-393.

[12] Godula, K.; Sames, D. *Science* **2006**, *312*, 67-72.

[13] Jones, W. D. *Inorg. Chem.* **2005**, *44*, 4475-4484.

[14] Lapointe, D.; Fagnou, K. *Chem. Lett.* **2010**, *39*, 1118-1126.

[15] García-Cuadrado, D.; Braga, A. A. C.; Maseras, F.; Echavarren, A. M. *J. Am. Chem. Soc.* **2006**, *128*, 1066-1067.

[16] García-Cuadrado, D.; de Mendoza, P.; Braga, A. A. C.; Maseras, F.; Echavarren, A. M. *J. Am. Chem. Soc.* **2007**, *129*, 6880-6886.

[17] Davies, D. L.; Macgregor, S. A.; McMullin, C. L. *Chem. Rev.* **2017**, *117*, 8649-8709.

[18] Satoh, T.; Miura, M. *Chem. Eur. J.* **2010**, *16*, 11212-11222.

[19] Colby, D. A.; Tsai, A. S.; Bergman, R. G.; Ellman, J. A. *Acc. Chem. Res.* **2012**, *45*, 814-825.

[20] Song, G.; Wang, F.; Li, X. *Chem. Soc. Rev.* **2012**, *41*, 3651-3678.

[21] Patureau, F. W.; Wencel-Delord, J.; Glorius, F. *Aldrichimica Acta* **2012**, *45*, 31-41.

[22] Lyons, T. W.; Sanford, M. S. *Chem. Rev.* **2010**, *110*, 1147-1169.

[23] Le Bras, J.; Muzart. J. *Chem. Rev.* **2011** ,*111*, 1170-1214.

[24] Arockiam, P. B.; Bruneau, C.; Dixneuf, P. H. *Chem. Rev.* **2012**, *112*, 5879-5918.

[25] Ackermann, L. *Acc. Chem. Res.* **2014**, *47*, 281-295.

[26] Moselage, M.; Li, J. Ackermann, L. *ACS Catal.* **2016**, *6*, 498-525.

[27] Guo, X.-X.; Gu, D.-W.; Wu, Z.; Zhang, W. *Chem. Rev.* **2015**, *115*, 1622-1651.

[28] Stuart, D. R.; Fagnou, K. *Science* **2007**, *316*, 1172-1175.

[29] Fukutani, T.; Umeda, N.; Hirano, K.; Satho, T.; Miura, M. *Chem. Commun.* **2009**, 5141-5143.

[30] Louillat, M.-L.; Biafora, A.; Legros, F.; Patureau, F. W. *Angew. Chem. Int. Ed.* **2014**, *53*, 3505-3509.

[31] Zheng, J.; Wang, S.-B.; Zheng, C.; You, S.-L. *J. Am. Chem. Soc.* **2015**, *137*, 4880-4883.

[32] Du, Y.; Hyster, T. K.; Rovis, T. *Chem. Commun.* **2011**, *47*, 12074-12076.

[33] Neely, J. M.; Rovis, T. *J. Am. Chem. Soc.* **2013**, *135*, 66-69.

[34] Liu, B.; Hu, P.; Zhou, X.; Bai, D.; Chang, J.; Li, X. *Org. Lett.* **2017**, *19*, 2086-2089.

[35] Guan, Z.-H; Ren, Z.-H.; Spinella, S. M.; Yu, S.; Liang, Y.-M.; Zhang, X. *J. Am. Chem. Soc.* **2009**, *131*, 729-733.

[36] Iturmendi, A.; Iglesias, M.; Munárriz, J.; Polo, V.; Pérez-Torrente, J. J.; Oro, L. A. *Chem. Commun.* **2017**, *53*, 404-407.

[37] Zhang, G.; Yang, L.; Wang, Y.; Xie, Y.; Huang, H. *J. Am. Chem. Soc.* **2013**, *135*, 8850-8853.

[38] Warratz, S.; Kornhaaβ, C.; Cajaraville, A.; Niepötter, B.; Stalke, D.; Ackermann, L. *Angew. Chem. Int. Ed.* **2015**, 54, 5513-5517.

[39] Biafora, A.; Patureau, F. W. *Synlett* **2014**, *25*, 2525-2530.

[40] Li, L.; Brennessel, W. W.; Jones, W. D. *Organometallics* **2009**, *28*, 3492-3500.

[41] Stuart, D. R.; Bertrand-Laperle, M.; Burgess, K. M. N.; Fagnou, K. *J. Am. Chem. Soc.* **2008**, *130*, 16474-16475.

[42] Martínes, A. M.; Echavarren, J.; Alonso, I.; Rodríguez, N.; Gómez Arrayás, R.; Carretero, J. C. *Chem. Sci.* **2015**, *6*, 5802-5814.

[43] García-Melchor, M.; Braga, A. A. C.; Lledós, A.; Ujaque, G.; Maseras, F. *Acc. Chem. Res.* **2013**, *46*, 2626-2634.

[44] Braga, A. A. C.; Ujaque, G.; Maseras, F. *Organometallics* **2006**, *25*, 3647-3658.

[45] Braga, A. A. C.; Morgon, N. H.; Ujaque, G.; Maseras, F. *J. Am. Chem. Soc.* **2005**, *127*, 9298-9307.

[46] Nova, A.; Ujaque, G.; Maseras, F.; Lledos, A.; Espinet, P. *J. Am. Chem. Soc.* **2006**, *128*, 14571-14578.

[47] Sperger, T.; Sanhueza, I. A.; Kalvet, I.; Schoenebeck, F. *Chem. Rev.* **2015**, *115*, 9532-9586.

[48] Xue, L.; Lin, Z. *Chem. Soc. Rev.* **2010**, *39*, 1692-1705.

[49] Sanhueza, I. A.; Wagner, A. M.; Sanford, M. S.; Schoenebeck, F. *Chem. Sci.* **2013**, *4*, 2767-2775.

[50] Jiang, J.; Ramozzi, R.; Morokuma, K. *Chem. Eur. J.* **2015**, *21*, 11158-11164.

[51] Li, L.; Brennessel, W. W.; Jones, W. D. *J. Am. Chem. Soc.* **2008**, *130*, 12414-14219.

[52] Han, Y.-F.; Jin, G.-X. *Chem. Soc. Rev.* **2014**, *43*, 2799-2823.

[53] Xu, L.; Zhu, Q.; Huang, G.; Cheng, B.; Xia, Y. *J. Org. Chem.* **2012**, *77*, 3017-3024.

[54] Semakul, N.; Jackson, K. E.; Paton, R. S.; Rovis, T. *Chem. Sci.* **2017**, *8*, 1015-1020.

[55] Quiñones, N.; Seoane, A.; García-Fandiño, R.; Mascareñas, J. L.; Gulías, M. *Chem. Sci.* **2013**, *4*, 2874-2879.

[56] Davies, D. L.; Ellul, C. E.; Macgregor, S. A.; McMullin, C. L.; Singh, K. *J. Am. Chem. Soc.* **2015**, 137, 9659-9669.

[57] Ruiz, S.; Villuendas, P.; Ortuño, M. A.; Lledós, A.; Urriolabeitia, E. P. *Chem. Eur. J.* **2015**, *21*, 8626-8636.

[58] Mei, R.; Wang, H.; Warratz, S.; Macgregor, S. A.; Ackermann, L. *Chem. Eur. J.* **2016**, *22*, 6759-6763.

[59] Ye, B.; Cramer, N. *Acc. Chem. Res.* **2015**, *48*, 1308-1318.

[60] Gaussian 09, Revision **D.01**, Frisch, M. J.; Trucks, G. W.; Schlegel, H. B.; Scuseria, G. E.; Robb, M. A.; Cheeseman, J. R.; Scalmani, G.; Barone, V.; Mennucci, B.; Petersson, G. A.; Nakatsuji, H.; Caricato, M.; Li, X.; Hratchian, H. P.; Izmaylov, A. F.; Bloino, J.; Zheng, G.; Sonnenberg, J. L.; Hada, M.; Ehara, M.; Toyota, K.; Fukuda, R.; Hasegawa, J.; Ishida, M.; Nakajima, T.; Honda, Y.; Kitao, O.; Nakai, H.; Vreven, T.; Montgomery, J. A., Jr.; Peralta, J. E.; Ogliaro, F.; Bearpark, M.; Heyd, J. J.; Brothers, E.; Kudin, K. N.; Staroverov, V. N.; Kobayashi, R.; Normand, J.; Raghavachari, K.; Rendell, A.; Burant, J. C.; Iyengar, S. S.; Tomasi, J.; Cossi, M.; Rega, N.; Millam, J. M.; Klene, M.; Knox, J. E.; Cross, J. B.; Bakken, V.; Adamo, C.; Jaramillo, J.; Gomperts, R.; Stratmann, R. E.; Yazyev, O.; Austin, A. J.; Cammi, R.; Pomelli, C.; Ochterski, J. W.; Martin, R. L.; Morokuma, K.; Zakrzewski, V. G.; Voth, G. A.; Salvador, P.; Dannenberg, J. J.; Dapprich, S.; Daniels, A. D.; Farkas, Ö.; Foresman, J. B.; Ortiz, J. V.; Cioslowski, J.; Fox, D. J. Gaussian, Inc., Wallingford CT, 2009.

[61] Grimme, S. *J. Comp. Chem.* **2006**, *27*, 1787-1799.

[62] Becke, A. D. *J. Chem. Phys.* **1993**, *98*, 5648-5652.

[63] Zhao, Y.; Schultz, N. E.; Truhlar, D. G. *J. Chem. Theory Comput.* **2006**, *2*, 364-382.

[64] Perdew, J. P. *Phys. Rev. B* **1986**, *22*, 8822-8824.

[65] Gimme, S. Antony, J. Ehrlich, S.; Krieg, H. *J. Chem. Phys.* **2010**, *132*, 154104-19.

[66] Chai, J. D.; Head-Gordon, M. *Phys. Chem. Chem. Phys.* **2008**, *10*, 6615-6620.

[67] Tao, J. M.; Perdew, J. P.; Staroverov, V. N.; Scuseria, G. E. *Phys. Rev. Lett.* **2003**, *91*, 146401-4.

[68] Marenich, A. V.; Cramer, C. J.; Truhlar, D. G. *J. Phys. Chem.* B **2009**, *113*, 6378-6396.

[69] Hay, P. J.; Wadt, W. R. J. Chem. Phys. 1985, 82, 270-283.

[70] a) Hehre, W.J.; Ditchfield, R.; Pople, J.A. *J. Chem. Phys.* **1972**, 56, 2257-2261. b) Hariharan, P.C.; Pople, J.A. *Theoret. Chimica Acta* **1973**, *28*, 213-222. c) Francl, M.M.; Petro, W.J.; Hehre, W.J.; Binkley, J.S.; Gordon, M.S.; DeFrees, D.J.; Pople, J.A. *J. Chem. Phys.* **1982**, *77*, 3654-3665.

[71] Roy, L. E.; Hay, P. J.; Martin, R. L. *J. Chem. Theory Comput.* **2008**, *4*, 1029-1031.

[72] a) Krishnan, R.; Binkley, J.S.; Seeger, R.; Pople, J.A. *J. Chem. Phys.* **1980**, *72*, 650-654. b) McLean, A. D.; Chandler, G.S. *J. Chem. Phys.* **1980**, *72*, 5639-5648.

[73] Weigend, F.; Ahlrichs, R. *Phys. Chem. Chem. Phys.* **2005**, *7*, 3297-3305.

[74] GaussView, Version 5, Dennington, R.; Keith, T.; Millam, J. *Semichem Inc.*, Shawnee Mission KS, 2009.

[75] Ueura, K.; Satoh, T.; Miura, M. *Org. Lett.* **2007**, *9*, 1407-1409.

[76] Ueura, K.; Satoh, T.; Miura, M. *J. Org. Chem.* **2007**, *72*, 5362-5367.

[77] Wang, N.; Li, B.; Song, H.; Xu, S.; Wang, B. *Chem. Eur. J.* **2013**, *19*, 358-364.

[78] Lide, D. R. *CRC Handbook of Chemistry and Physics*, 84th Edition, CRC Press: Florida, USA, 2003. pp.8.48-8.53

[79] Brown, G. M.; Chidambaram, R. *Acta Cryst.* **1973**, *B29*, 2393-2403

[80] Powers, D. C.; Benitez, D.; Tkatchouk, E.; Goddard III, W. A.; Ritter, T. J. *J. Am. Chem. Soc.* **2010**, *132*, 14092-14103.

[81] Anand, M.; Sunoj, R. B.; Schaefer, H. F. *J. Am. Chem. Soc.* **2014**, *136*, 5535-5538.

[82] Olson, L. P.; Whitcomb, D. R.; Rajeswaran, M.; Blanton, T. N.; Stwertka, B. J. *Chem. Mater.* 2006, *18*, 1667-1674.

[83] Louillat, M.-L.; Patureau, F. W. *Org. Lett.* **2013**, *15*, 164-167.

[84] Ray, R.; Chandra, S.; Maiti, D.; Lahiri, K. L. *Chem. Eur. J.* **2016**, *22*, 8814-8822.

[85] Jover, J.; Spuhler, P.; Zhao, L.; McArdle, C.; Maseras, F. *Catal. Sci. Technol.* **2014**, *4*, 4200-4209.

Chapter 4

Copper-Catalyzed Water Oxidation

4.1 Background

General introduction

Among all the problems humanity is facing in the new century, global warming has positioned itself as one of the most urgent. There is a prompt need of change to preserve the environment for current and future generations. In the search for the causes of global warming, the energy and transport industry sectors have been singled out because of the common factor they share: the use of fossil fuels as raw material. Nowadays, fossil fuels (oil, natural gas and coal) provide approximately the 86% of the energy consumption, thus showing our huge dependence on them (Scheme 4.1). They are the main source of the energy needed to keep the living standards we have reached as a society.

Scheme 4.1 Distribution of the energy consumption depending on the energy source. Data taken from BP statistical review.[1]

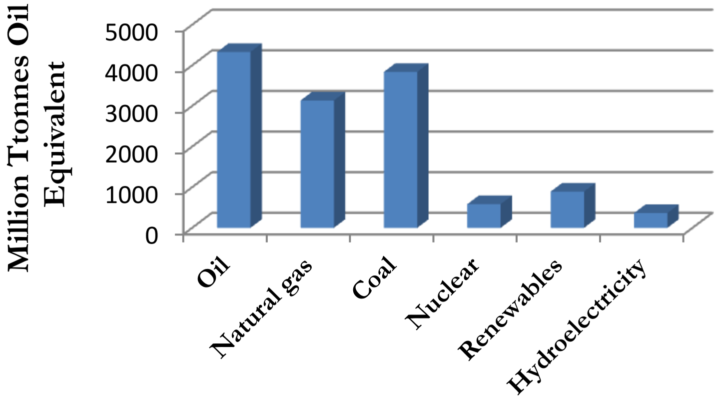

The use of these fuels has led over time to an increase of the CO_2 concentration in Earth's atmosphere with the concomitant increase in temperature, due to the greenhouse effect.[2]

Institutions, governments and other organizations have been proposing strategies and actions to slow down global warming. Several agreements, such as the Kyoto protocol or the Paris agreement, establish methods based on a better use of already available technology and a reduction of energy consumption. However, more drastic changes will be required to reach a real sustainable development and they necessarily have to be based on research and innovation.

Scheme 4.3 Schematic representation of natural photosynthesis versus artificial photosynthesis.

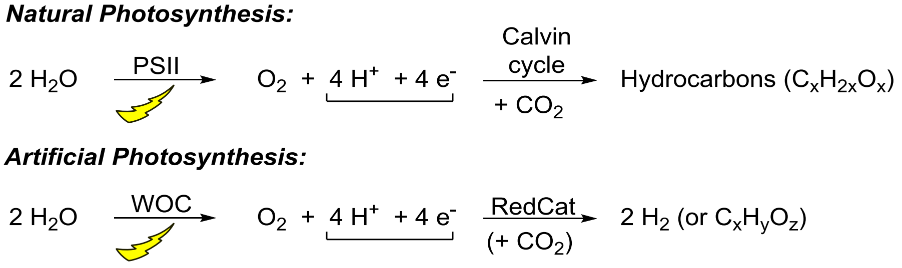

Artificial photosynthesis is currently one of the most promising approach for non-fossil-based energy production.[3,4] It owes its name to similarities with the natural photosynthesis carried out by green plants and algae, where water and sunlight are used as feedstock for the synthesis of molecules with a higher energy content. The general process of artificial photosynthesis is depicted in Scheme 4.2 and consists of using the solar energy to oxidize the water molecule releasing oxygen and protons and further using these protons to produce either molecular hydrogen or hydrocarbons (if CO_2 is also employed). Those last products harvest the solar energy in their chemical bonds and can be used as fuels for energy production, being called "solar fuels".[5] The important benefits of this approach are mainly the use of solar energy, which is a renewable and harmless source of energy, and the absence of net emission of CO_2.

Scheme 4.3 Photochemical cell to produce solar fuels from the water splitting reaction.

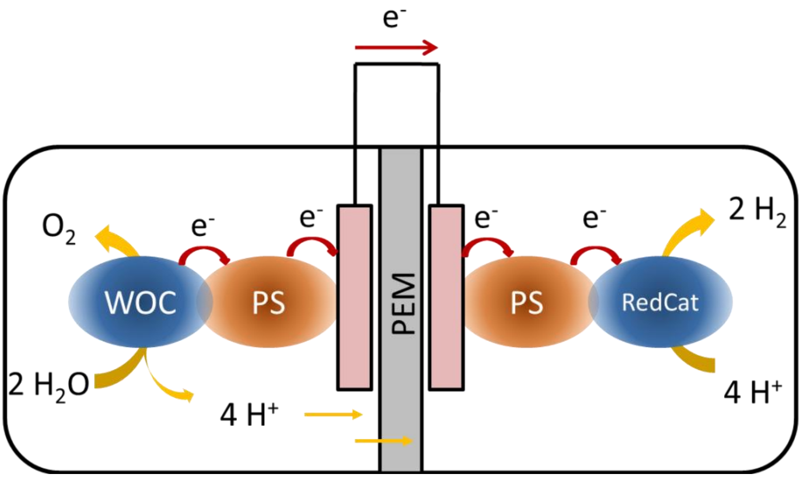

A potential industrial design for artificial photosynthesis would involve the incorporation of both redox reactions in different compartments of a single device (Scheme 4.3). In the anodic compartment, the water would be oxidized to molecular oxygen with the subsequent release of protons. The latter would travel through a proton exchange membrane (PEM) to the cathodic compartment where they would be reduced to hydrogen (or hydrocarbons). This architecture offers an easy way to separate both products from the reaction as well as a way to avoid undesired recombination reactions that would reduce the overall performance.

An economically competent device would also require both reactions to take place with sufficient efficiency. This is not trivial as those reactions are thermodynamically disfavored and kinetically complex because they require the breaking of 4 H-O bonds and the subsequent formation of O-O and H-H (or C-H in the case of CO_2 reduction) bonds. The unfavorable thermodynamics may be solved through the use of a photosensitizer (PS) (molecule or semiconductor) to capture the sunlight as energy input. The kinetic problems may be solved through the use of catalysts: a water oxidation catalyst (WOC) and a proton or CO_2 reduction catalyst (RedCat).[6] The requirements are more difficult to achieve for the water oxidation half reaction, which has led to a deep study of its mechanism during the last decades.[7,8]

Scheme 4.4 Three different approaches for water oxidation catalysis: materials, hybrid materials and molecular catalysts.

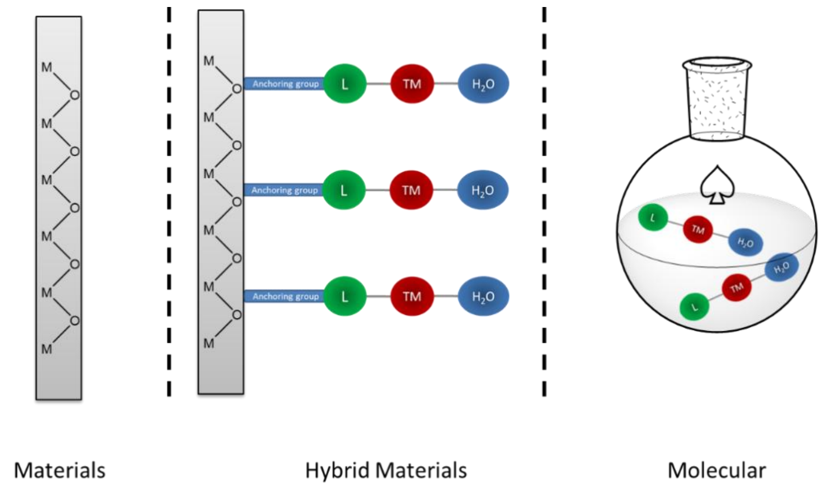

In a first approach, water oxidation catalysts can be divided in two wide groups according to their chemical nature: materials and molecular species (Scheme 4.4). The first group mainly consists of transition metal oxides containing in most cases Ru, Ir, Mn, Ni, Fe, Co and Cu.[9] From a practical point of view, materials benefit from the easy handling for the inclusion in commercial photosynthetic devices. Moreover, metal oxides are in general physically and chemically robust as is needed for long-lived systems under the stringent conditions that water oxidation requires. However, progress in the application of material for this purpose is slowed down by the difficult rationalization of the factors that contribute to their catalytic activity, which hinders the complex tuning of their properties.

In contrast, molecular water oxidation catalysts, which are mainly based on transition metal complexes, offer a wider range of spectroscopic and analytical techniques that help to isolate the influence of structural and chemical factors such as geometry, coordination number, character of coordinating atoms, etc.[10] This makes easier the rational design of more active catalysts by the relatively simple tuning of the ligand properties. This group also includes other fully inorganic molecular species such as molecular oxides and polyoxometalates but their behavior as catalyst is often closer to that observed for materials.

Finally, a third group has recently emerged from the application of hybrid materials coming from the anchoring or immobilization of molecular catalyst on electrode surfaces.[11,12] This strategy could benefit from the advantages of the two previous ones, but is still under development.

Molecular water oxidation catalysis

The field of molecular water oxidation catalysis started back in 1982 with the synthesis of the first molecular catalyst that was named "blue dimer", *cis,cis*-$[(bpy)_2(H_2O)Ru^{III}(\mu\text{-}O)Ru(H_2O)(bpy)_2]^{4+}$.[13] This complex consisted of a dinuclear ruthenium catalyst where both metal centers were bonded through an oxygen bridge (Scheme 4.5). Although its activity as a catalyst was quite limited, its discovery constituted the beginning of an active research field that has grown exponentially over time.

Scheme 4.5 First molecular water oxidation catalyst based on a ruthenium dimer ("blue dimer").

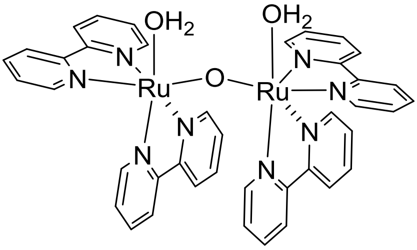

Blue dimer

After the "blue dimer" was reported, the attention focused on Ru complexes. In fact, most of the current examples in the literature are based on dinuclear and mononuclear complexes bearing Ru as metal center. The activity and stability of those catalysts were progressively improved by the rational design of more robust and stabilizing ligands. After several generations of Ru based catalyst, the development has resulted in several examples that first matched and then exceeded the rate of the natural process taking place in Photosystem II (PSII).[14,15] Although more recent, the development of Ir based catalysts has also provided some highly active catalysts. Kärkäs and Akermark summarized most of the research activity on ruthenium and iridium examples in a comprehensive review of molecular based water oxidation.[16]

Although high activities have been reached by these second and third row transition metal complexes, it is worth noting that they display the severe drawback of the expensive and toxic character of those precious metals. Therefore, first row transition metals have started to be considered as potential molecular catalysts because of their abundance, relatively low price and environmentally friendliness. In the last few years, examples containing iron,[17] cobalt,[18,19] nickel [20] and copper [21,22,23] have been reported that efficiently catalyze water oxidation. Although less active than the Ru and Ir based catalysts, they are currently one of the focal points in water oxidation catalysis.

Scheme 4.6 Water nucleophilic attack (WNA) and Intramolecular/Intermolecular coupling of Two Metal-oxo units (I2M) mechanisms.

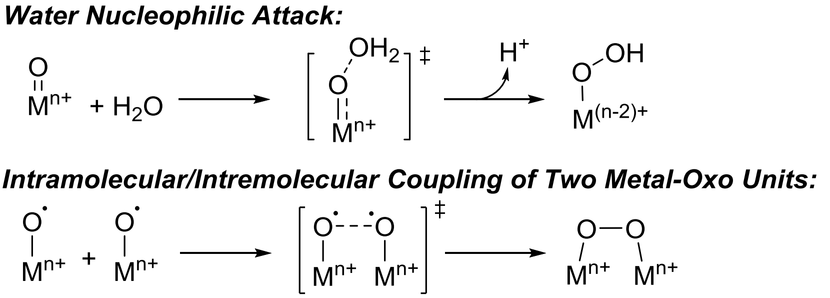

Despite the different nature of the metal centers used in this reaction, they all share similar features in their catalytic mechanism.[24] First, at least one water molecule is coordinated to the metal center and is oxidatively activated by the release of electrons from the metal moiety leading to higher oxidation states. These oxidations are often accompanied by proton release in a process named Proton Coupled Electron Transfer (PCET). These concerted transfers of electrons and protons lead usually to an intermediate where an oxo center is bound to a metal in a high oxidation state. This oxidative activation process results in the formation of an activated oxygen atom with an electron deficit. Thus, the oxygen center has a certain electrophilic character and is able to receive nucleophilic attacks from external oxygen centers, resulting in the formation of an O-O bond. This step is currently accepted to proceed through two alternative mechanisms mainly based on the knowledge generated for Ru catalysts: Water Nucleophilic Attack (WNA) and Intramolecular/Intermolecular coupling of two metal-oxo units (I2M). As can be deduced from the names, the main difference between both mechanisms lies on the involvement of an external water molecule in the O-O bond formation.

In the case of WNA, the highly oxidized metal center in the aquo-complex is susceptible to a nucleophilic attack on the activated oxygen by an external water molecule. This mechanism involves a concerted two electron transfer from the oxygen in the external water molecule to the oxidized metal center with the concomitant O-O bond formation. In the case of the I2M mechanism, the metal-oxygen bond of the aquo group is largely polarized to the metal center providing the oxygen atom with a radical character. Therefore, the coupling of two metal-oxo radicals ends up forming the O-O bond with low kinetic barrier. In both cases, once the O-O bond has been formed, oxidation of the peroxo group results in the release of molecular oxygen and the regeneration of the catalyst.

The identification and control of the water oxidation mechanism has proved to be essential for the design of more active catalysts.[25,26] In this sense, computational methods provide a powerful tool to elucidate those mechanisms and identify the factors that determine the reactivity of the catalysts. DFT methodologies have long been applied to molecular Ru complexes [27,28] but, in contrast, first row transition metal catalysts lack of complementary computational studies. Some examples in the literature show computed catalytic cycles for Fe [29,30] and Cu [23,31,32] catalysts but they are often based on Ru chemistry and preliminary.

Therefore, there is an underlying need to undertake more detailed computational studies on this new generation of first row transition metal catalysts to facilitate a rational design of promising system that eventually could be employed in practical devices. We will focus in this chapter in the computational study on copper-based water oxidation, including a new family of catalysts developed in collaboration with Prof.

Llobet and co-workers and a wider study on other reported copper complexes.

4.2 Computational Details

Computational methods

In this chapter 4, we carried out all the calculations with the Gaussian09 (D.01) program package.[33] Density Functional Theory has demonstrated its effectiveness in the study of water oxidation reactions,[34] and for this reason, we based our study on DFT methodology. The functional that we have used mainly is the hybrid-GGA B3LYP,[35] including D3 empirical dispersion correction developed by Grimme.[36] This functional was selected due to the accurate reproduction of direct experimental measurements, the oxidation potential in cyclic voltammetry, which will be discussed in the next subsection. The solvation was introduced implicitly in all the optimizations using the SMD model with the experimental solvent, water ($\varepsilon = 78.3553$).[37] Considering the presence of different charged structures in the mechanism, we included diffuse functions in the basis set, even in the optimizations. We combined the LANL2TZ(f) basis set for copper (a triple-zeta basis set, including f-type polarization functions and the associated pseudopotential),[38] and the 6-31+G(d) for the rest of the atoms.[39]

All geometry optimizations were carried out without symmetry restrictions and the nature of the stationary point was confirmed by vibrational frequency calculations. The transition states were proved to have one imaginary frequency, while the minima had zero imaginary frequencies. In addition, free energy correction were calculated at 298.15 K and 105 Pa pressure, including Zero Point Energy (ZPE) corrections. To have better comparison with direct experimental measurements, which were made in solution, we corrected the standard state for all the calculations, from gas phase at 1 atm to solvent phase at 1M, using the correction term of 1.89 kcal/mol (see Chapter 2 for details).

Unlike in other fields of homogeneous catalysis, most of the experimental data that we can use to compare with the mechanistic calculations come from electrochemistry. For this reason, we should convert our energy units (usually kcal/mol or Hartrees) to electrochemical magnitude such as redox potential (Volts) or pH units. We took from the chemical literature the values of 4.28 V for the absolute potential of the standard hydrogen electrode (SHE)[40,41] and -11.72 eV for the energy of the proton in aqueous solution at pH = 1.[42] Additionally, the experimental pH was taken in account, correcting the free energy of the proton by the term of -0.059*pH, following the procedure reported by others.[43]

For benchmarking calculations, other functionals were used under similar conditions (same basis set and solvent model). The list of functionals used is: M06, M06-D3, M062X,[44] M06L,[45] B97D [46] and ωB97X-D.[47]

Along the sections 4.3 and 4.4, several 3D structures were drawn using the following legend of colors:

Carbon: ■ Hydrogen: □ Oxygen: 🟥 Nitrogen: 🟦

Copper: 🟧 Ruthenium: 🟩

Benchmarking of the computational method

In water oxidation, four protons and electrons are released from two water molecules in order to make the dioxygen molecules. This fact implies that several oxidation states and spin states are present during the mechanism. For this reason, this reaction is very challenging from a computational perspective, as the amount of Hartree-Fock exchange in hybrid functionals affects considerably the relative energy of the different spin states.. Thus, the selection of the proper functional is essential for a correct description of the system, balancing the accuracy of the method and the computational cost.

To select the functional, we performed a benchmark calculation in the single electron oxidation of initial catalysts [OPBA-Cu(II)]$^{2-}$ to form the copper(III) species, [OPBA-Cu(III)]$^{-}$. This step is representative of the problems that we mentioned above: the initial spin state is a double and the final is a singlet while the total charge goes from -2 to -1. Moreover, the reversible wave of the cyclic voltammetry, which is obtained experimentally, allows the direct comparison of the computed energy with an observable. In this case, the experimental magnitude is 0.56 V.

Table 4.1 Calculation of the Cu(II)-Cu(III) oxidation potential with different functional and the error in kcal/mol respect to experimental value of 0.56 V.

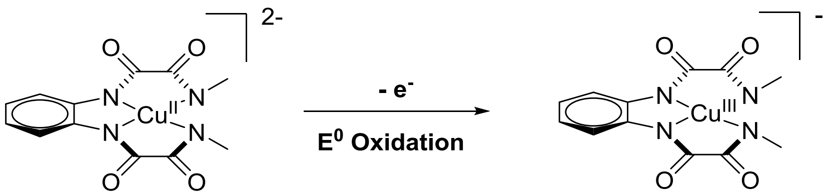

Functional	E^0 Oxidation (V)	Associated Error (ΔG^0_{calc} - ΔG^0_{exp}) (Kcal/mol)
B3LYP-D3	0.53	-0.7
M06	0.58	0.5
M06-D3	0.57	0.2
M06-L	-0.05	-14.1
M06-2X	1.66	25.4
B97D	-0.05	-14.1
ωB97X-D	0.80	5.5

We computed this step with several functionals, covering a wide range of HF exchange proportion, from pure functionals (M06-L and B97D) to standard hybrid functionals (B3LYP-D3 and M06), including also a long-range corrected functional (ωB97X-D) and M06-2X, which includes more than 50% of HF exchange.

The results are shown in Table 4.1 and they indicate that standard hybrid functionals, B3LYP and M06, with 20% and 27% of HF exchange respectively, give the best results with an error about 1 kcal/mol. Empirical dispersion brings a minor improvement to the results, as seen by the comparison between M06 and M06-D3. In contrast, pure DFT functionals (M06-L and B97D) underestimates the oxidation potential by 0.6 eV and M06-2X (54%HF exchange) overestimates it by 1 V. Finally, ω-B97xD, which has a short-range HF exchange of 22% and a long-rate of 100%, with a range separation parameter of 0.2, also overestimates the oxidation potential by 0.24 V. Therefore, we found a strong correlation between the percentage of HF exchange and the relative energies, demonstrating the necessity of doing benchmark calculations in redox reactions.

4.3 Water Oxidation Catalyzed by Tetraamidate-Copper Complexes

Experimental overview of the reaction

Following our interest in redox-catalyzed reactions, we moved to water oxidation catalysis. In 2015, we initiated an experimental/theoretical collaboration with Prof. Antoni Llobet and his group at the ICIQ to develop a new family of first-row transition metal water oxidation catalyst.

They prepared a promising compound (Scheme 4.7) based on a tetraanionic tetradentate amidate ligand (N1,N1'-(1,2-phenylene)bis(N2-methyloxalamide), from now L_1) that showed interesting electrochemical behavior. The synthesized dianionic copper(II)-L_1 complex was designed to stabilize high oxidation states in copper. In addition, the ligand structure suggest a redox-active character.[48] However, the basic character of the ligand restricts the applicability to basic pH (around 11.5).

Scheme 4.7 Water oxidation by mononuclear Cu-based water oxidation catalyst.

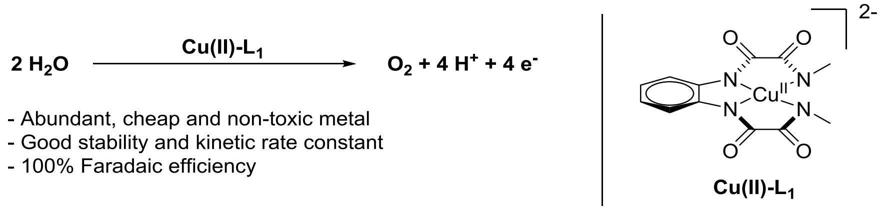

- Abundant, cheap and non-toxic metal
- Good stability and kinetic rate constant
- 100% Faradaic efficiency

The redox properties of compound [Cu(II)-L$_1$] were studied by cyclic voltammetry (CV) using the mercury sulphate reference electrode saturated with potassium sulphate (MSE). They ran a series of pH dependent CV to analyze the effect of the pH in the electrochemistry (Figure 4.1).

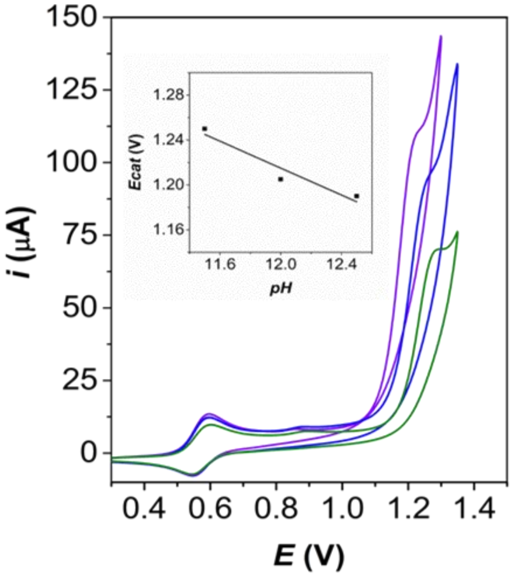

Figure 4.1 Cyclic voltammetry (phosphate buffer, scan rate = 100 mV/s) of Cu(II)-L$_1$ at different pH values (green at 11.5, blue at 12 and purple at 12.5). The potentials are shown versus NHE electrode. The inset represents the variation of the catalytic wave potential versus the pH.

Interestingly, there are two oxidation waves, the first one is clearly pH independent at 0.56 V, while the second one is the catalytic wave and decreases the oxidation potential when pH is increased. The correlation between this potential and the pH is shown in the inset of Figure 4.1, and the slope is near -0.059 V/pH, which is consistent with the involvement of one proton or hydroxo group during the oxidation. In addition, the presence of copper oxide nanoparticles deposited on the electrode was excluded by Energy Dispersive X-ray Spectroscopy (EDX). This was further confirmed by CV of the electrode after Controlled Potential Electrolysis (CPE) in a fresh buffer solution, showing that the behavior is comparable to that before CPE and no active material that could be responsible for the catalysis was deposited. Moreover, only the initial species remains in solution phase after one hour of bulk electrolysis. This is deduced by CV experiments and the absence of nanoparticles confirmed by Dynamic Light Scattering (DLS) analysis.

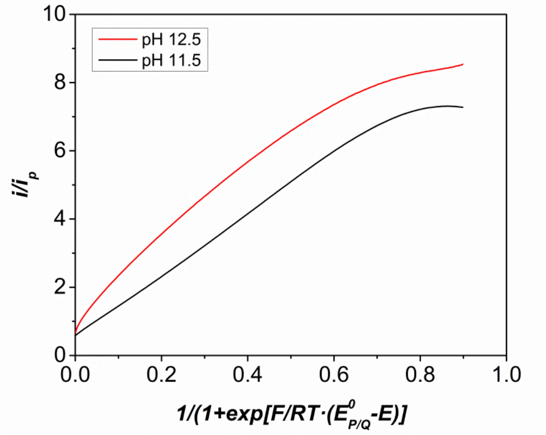

Figure 4.2. FOWA analysis of [Cu(II)-L_1] catalyst in the water oxidation reaction at two different pH. Data were obtained from background corrected CV responses in phosphate solutions (1mM [cat], 0.1M ionic strength) at 100 mV/s using GC as working electrode.

To gain valuable mechanistic information, our experimental colleagues also analyzed the kinetics of the reactions by Foot Of the Wave

Analysis (FOWA), which allows the calculation of the rate constant at the initial stages of the catalysis,[49] investigating the slope of the catalytic wave at the beginning of the catalytic process. Representing the anodic peak relative intensity versus a term based on the difference of the standard potential and the used potential (Figure 4.2), and upon mathematical treatment, the obtained rate constants were 3.56 s^{-1} at pH 11.5 and 11.96 s^{-1} at pH 12.5. This rate is independent of the scan rate, suggesting that the rate determining step is the electron transfer of the second oxidation.

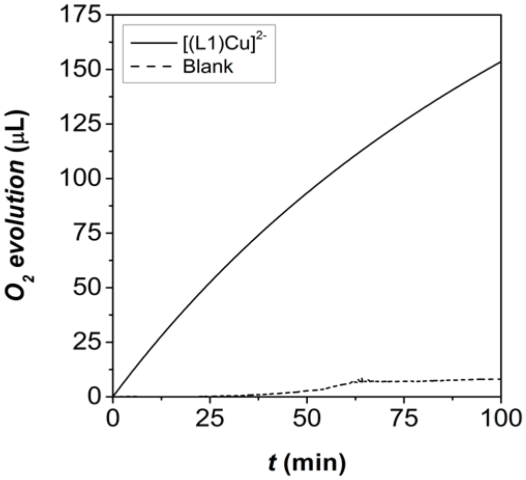

Figure 4.3 Oxygen evolution in electrolysis experiment of solution of 1mM Cu(II)-L_1 catalyst in a phosphate solution buffered to pH 11.5 (0.1 M of ionic strenght). Indium Tin Oxide (ITO) was used as working electrode, together with Mercurous sulfate reference and Pt mesh counter electrodes.

Finally, a bulk electrolysis experiment in conjunction with oxygen detection by Clark electrode was carried out to confirm the oxygen evolution and the effective water oxidation by the molecular copper catalysts (Figure 4.3). The faradaic efficiency was found to be close to 100% and if the pH is maintained by base addition during the electrolysis, the catalyst activity remains almost intact during long period of times (1 h), confirming the stability of the system.

These data demonstrated that a new copper-based water oxidation catalyst had been synthesized, and since only few complexes of copper had been discovered and almost no mechanistic information had been obtained, we decided to investigate the catalytic cycle by means of density functional theory, in order to understand the oxygen-oxygen bond formation mechanism.

SET-WNA mechanism

According with the experimental data, the electrochemical water oxidation catalyzed by [Cu(II)-L_1] has two waves in the CV, one at 0.56 V and the other at 1.25 V. Moreover, the first one is pH-independent and the second one shows a pH dependence around 0.059 V/pH. After the second activation, the catalysis starts and is associated with the large increase of the current at the anode. We started the computational study from this point, trying to discover the nature of these oxidations, using DFT calculations.

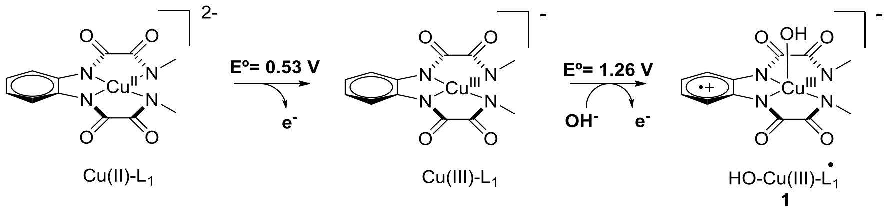

Figure 4.4 Calculation of the active species formation by two consecutive oxidations of Cu(II)-L_1. Redox potentials in Volts versus NHE.

The Cu(II) complex cannot coordinate water or hydroxo groups in the apical positions, and this coordination is also very endergonic in Cu(III). For this reason, the first oxidation is associated with the one electron release from the initial complex [Cu(II)-L_1] to yield [Cu(III)-L_1]. The calculated value is 0.53 V respect to the NHE (Figure 4.4), in perfect (maybe fortuitous) agreement with the experimental value. Then, the second wave is calculated from [Cu(III)-L_1] to "Cu(IV)-L_1-OH", which is the active species and is responsible of the catalytic O-O bond formation. We labeled this species as **1** and it is produced after the coordination of an hydroxo group, which stabilized the high oxidation state of the complex. The OH^- coordination explains the pH dependency of the catalytic wave. Again, the calculated potential is also in agreement with the experimental value, 1.26 V and 1.25 V, respectively.

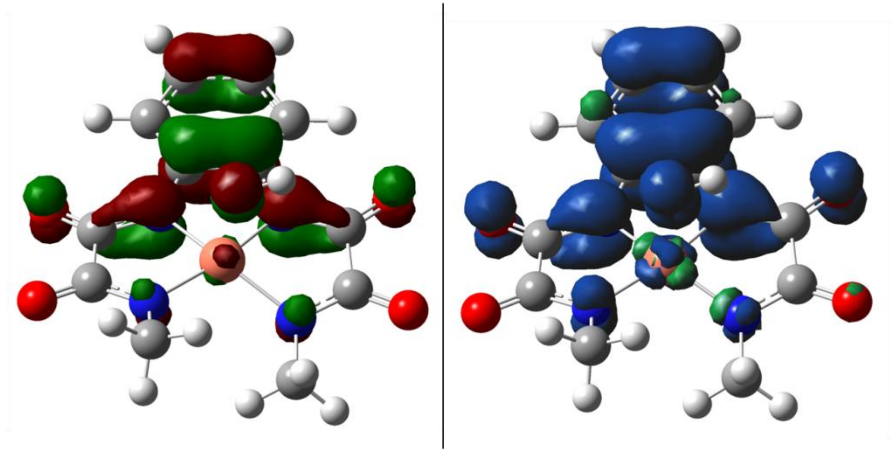

Figure 4.5 3D representation of the SOMO orbital (left) and the spin density distribution (right) for the active species $[(OH)Cu(III)L_1^{+\cdot}]$ (**1**).

Interestingly, the second oxidation does not form Cu(IV). Instead, the electron is removed from the redox active ligand, producing the cation radical on the ligand, with the electron density mainly located on the phenyl ring (Figure 4.5, right). The SOMO orbital (Figure 4.5, left) is correlated with the spin density distribution and shows the typical delocalized structure of organic aryl radicals. This fact suggests that the stability of the radical is strongly related with the electronic structure of the ligand and can be modified in an easy way, an aspect that we will discuss in detail in the following section.

Once the active species is formed, the next step is the oxygen-oxygen bond formation, which is usually the crucial step in water oxidation. Due to the radical character on the ligand, we discarded the I2M mechanism for this reaction and our first effort was to discover the Water Nucleophilic Attack (WNA) mechanism.

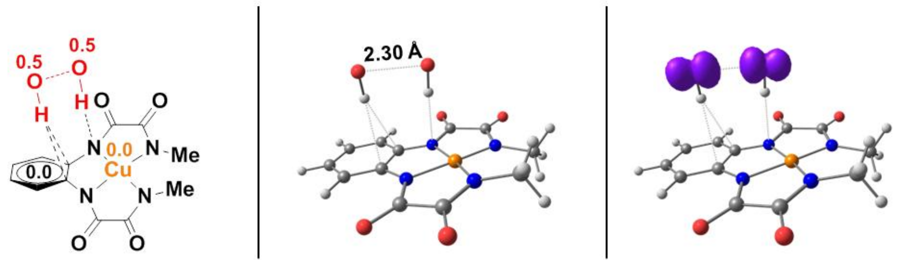

Figure 4.6 Representation of 2c3e HO---OH-Cu(III) structure **2**. 2D molecule with spin densities (left), 3D structure with the O-O bond length interaction in Å (center) and 3D structure with spin density distribution.

Surprisingly, when, we approach a hydroxo group (since we are in basic media) to intermediate **1**, we cannot find the transition state for this WNA. Instead, the optimization always falls on an unexpected species, **2**, where the unpaired electron is shared the two oxygen atoms (see Figure 4.6). In this species **2**, one electron from the hydroxo groups has been released to the ligand, reducing it and forming an O---O interaction with three electrons between two centers, two in the bonding orbital and one in the antibonding orbital, forming a 2c3e bond. This type of bonding had been discussed previously in the literature,[50] but had not ever been reported in the water oxidation mechanism. This species **2** is more stable than the separated initial species by 4.4 kcal/mol. This suggests it is actually formed during the reaction (Figure 4.6).

To connect the initial active species **1**, with the hydroperoxide species **3**, we performed a relaxed scan connecting the different structures (Figure 4.7). We could not find the transition state of the first single electron transfer. The reaction coordinate is complicated. There is a reorientation of the entering hydroxo group, from the hydrogen bonded structure **1-OH$_{\text{adduct}}$**, to the O---O 2c3e species **2**. At the same time, the Cu-OH bond is broken and one electron is released from the hydroxo group to the ligand. We could nevertheless estimate the energy of this step from the potential energy relaxed scan, with a potential energy barrier near 0. The free energy associated to the process was estimated by the difference between the separated structures **1** and the adduct **1-OH**$_{\mathbf{adduct}}$, and it is only 5.5 kcal/mol.

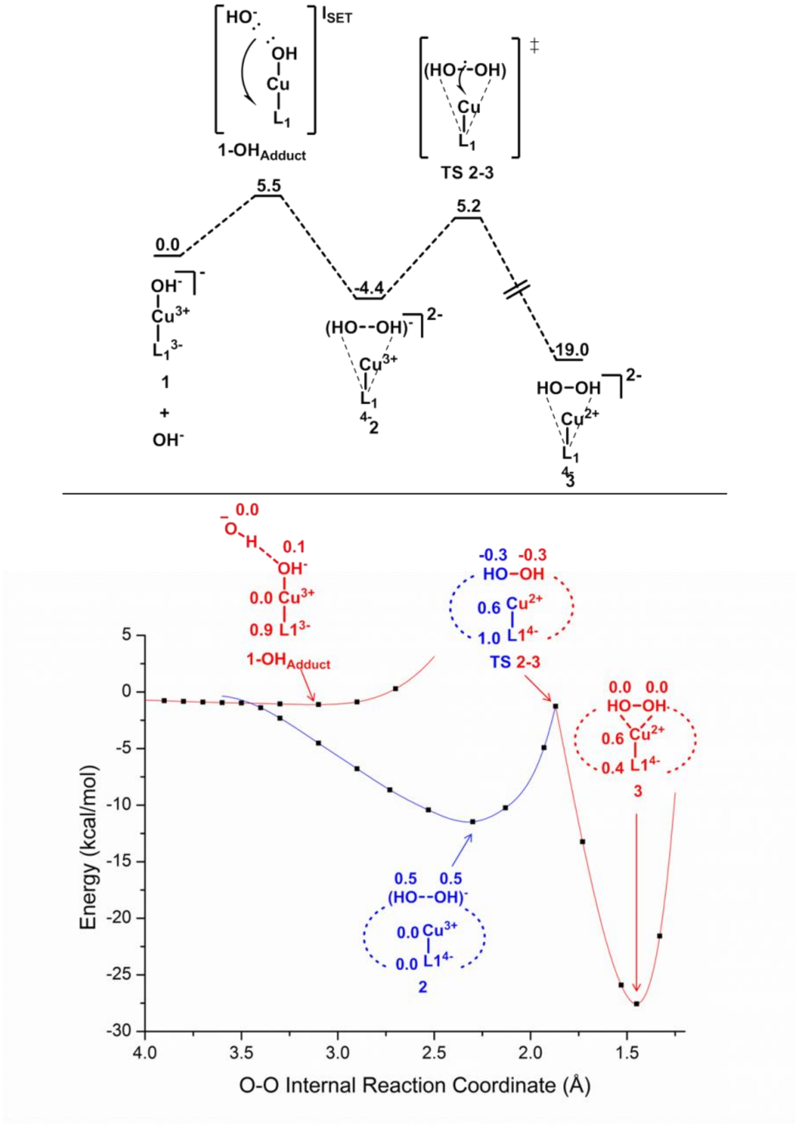

Figure 4.7 Free energy profile of the O-O bond formation step through SET-SNA mechanism from active species **1** (top). Energies in kcal/mol. Potential energy relaxed scan of O-O internal reaction coordinate with spin densities in key structures (bottom).

Finally, the reaction goes from **2** to **3** through a second single electron transfer, from the O---O antibonding orbital to Cu(III), forming the oxygen-oxygen bond (resulting in each oxygen center oxidized to -1 oxidation state) and copper reduced to Cu(II). We found the transition state **TS 2-3** at 5.2 kcal/mol, with an overall barrier of 13.9 kcal/mol, calculated from the most stable point, the species **2** separated in the Cu(III) and the HO---OH fragment (which is more stable than the associated species **2** by 4.3 kcal/mol).

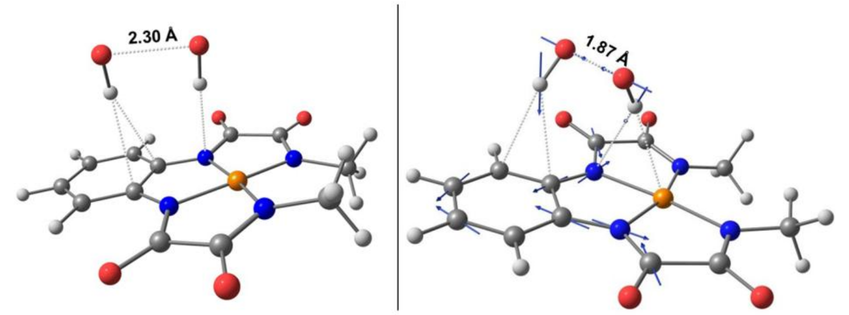

Figure 4.8 Comparison between optimized structures of **2** (left) and TS **2-3** (right). Arrows indicate the displacement vectors of the normal mode associated with the imaginary frequency in **TS 2-3**. Distances are in Å.

The spin density in **TS 2-3** demonstrates that this transition state has extra open shells beyond the necessary one associated to a doublet. The S^2 value is 1.3262, higher than the expected 0.75 for a “normal” doublet electronic structure. During the transition state, one ligand-copper bonding orbital has mostly α spin, opening the electronic structure to allow the electron transfer from the oxygen-oxygen moiety to the ligand. This is confirmed by the displacement vector of the imaginary frequency associated with the transformation (Figure 4.8, right), where the ligand is involved in the electron transfer when the oxygen-oxygen bond is forming. From this transition state, the peroxo species **3** is formed exothermically, at the free energy of -19.5 kcal/mol, with copper in oxidation state 2.

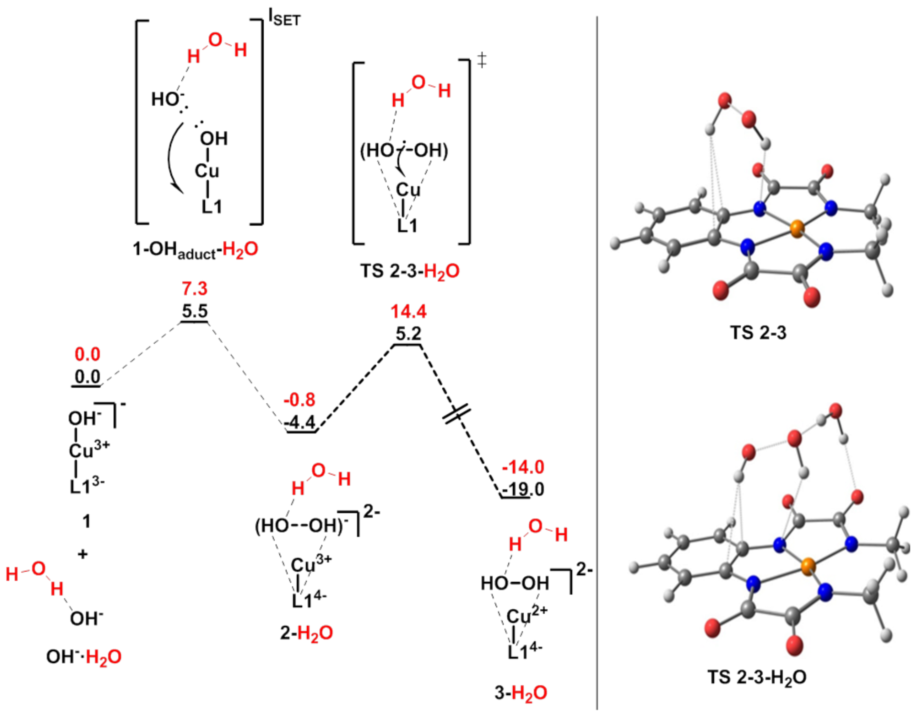

Figure 4.9 Free energy profile of SET-WNA mechanism in black versus the water-assisted mechanism in red (left). Energies in kcal/mol. 3D structures of transition states **TS 2-3** and **TS 2-3-H₂O** (right).

Including explicit water molecules in the O-O bond formation step has been demonstrated to be crucial in WNA mechanisms. For this reason, we repeated the calculations above adding one extra water molecule. We kept the core frozen, letting the water molecule to optimize obtaining the free energy profile of Figure 4.9. In all the cases, the water molecule is attached through hydrogen bonds to the oxygens that are being coupled. The enthalpy change associated with this interaction is not too exothermic and does not stabilize the system to overcome the entropy loss, suggesting that water does not play an important role in our mechanism. This result was further confirmed by the optimization of the transition state **TS 2-3**$_{\mathbf{H2O}}$ without constraints. The free energy is 1.8 kcal/mol above **TS 2-3**, thus corroborating the lack of influence of explicit water molecules in the SET-WNA mechanism. We also evaluated the transition state with two explicit water molecules, but the barrier is even higher, 22.5 kcal/mol. This fact can be explained because in the classic WNA, one proton is released to the media and explicit water molecules are needed to capture this proton. In contrast, the SET-WNA directly uses the OH- anion as nucleophile, so no proton is released, minimizing the potential role for the external water.

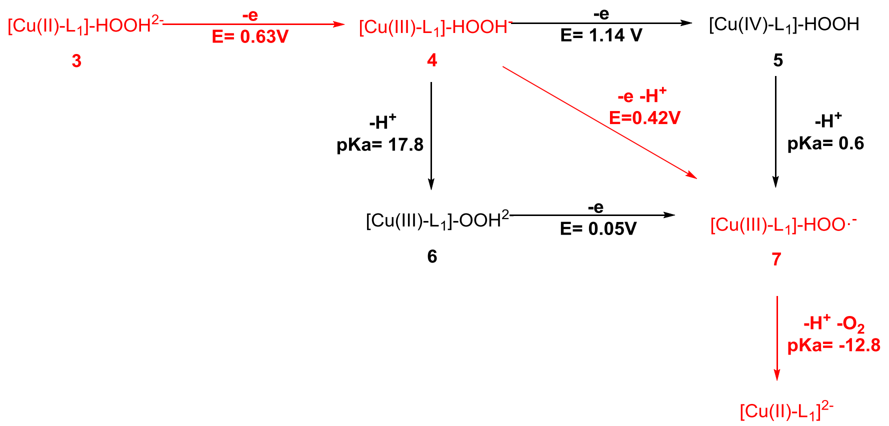

Figure 4.10 Thermodynamic diagram for oxygen evolution from intermediate **3**. The most favored pathway is highlighted in red.

Finally, oxygen evolves from the hydrogen peroxide complex **3** (Figure 4.10) to form the final molecular oxygen product after two consecutive oxidations. We constructed the thermodynamic cycle to find the key steps in this process. The first step is the oxidation of intermediate **3** to intermediate **4**, with a standard redox potential of 0.63 V. Then, there are three different possibilities: second electron transfer + deprotonation (**4** to **5** and **5** to **7**), deprotonation + second electron transfer (**4** to **6** and **6** to **7**) or the proton coupled electron transfer (PCET) (**4** to **7**). The most favored is the PCET, with an oxidation potential of only 0.42 V. The other two possibilities imply higher energy pathways, the first one with a high potential of 1.14 V (from **4** to **5**) and the second one with an associated pK_a of 17.8, too high for experimental conditions (pH = 11.5). Finally, molecular oxygen evolves from intermediate **7** after deprotonation. We do not find any transition state here, since the oxygen is released upon proton removal.

Overpotential control

The calculated mechanism of the copper-catalyzed water oxidation revealed some interesting features that could be used for the rational improvement of the reaction. We demonstrated, in agreement with the experimental work, that the catalytic wave is based on the redox active ligand, and the free energy barrier of the process is below 15 kcal/mol, confirming the experimental evidence that the second oxidation is the rate determining step of the reaction. For this reason, we decided to modify the backbone of the ligand in order to stabilize the radical in the active species.

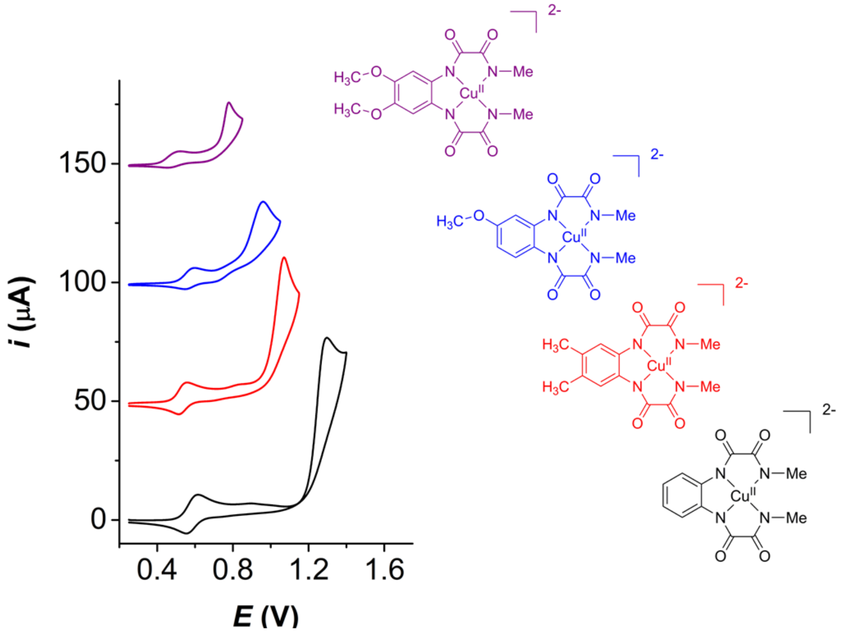

Figure 4.11 Cyclic voltammetries of the family of copper water oxidation catalyst using 1mM solutions in phosphate buffer at pH 11.5 (0.1 M of ionic strength). Glassy carbon (GC) was used as working electrode, together with mercurous sulfate reference and Pt mesh counter electrodes.

In this way, the overpotential of the reaction would be easily modified in a rational way. Garrido-Barros synthesized efficiently the modified ligands and the associated copper complexes that are depicted in Figure 4.11. He obtained three other different compounds, introducing donating groups in the phenyl ring (Figure 4.11). The red one ([Cu(II)-L_2]), with two methyl groups, the blue one ([Cu(II)-L_3]) with one methoxy and the purple one ([Cu(II)-L_4]) with two methoxy groups. As expected, the overpotential of the reaction decreased progressively when more donating groups are present, as the cationic radical formed after the second oxidation is more stabilized. The overpotential decreases from 700 mV in Cu(II)-L_1 to the remarkable value of 170 mV above the thermodynamic water oxidation potential. This is the first time in the literature that a rational design of a ligand allows the precise control of the electrocatalytic wave, representing also a record low for first row transition metal complexes.

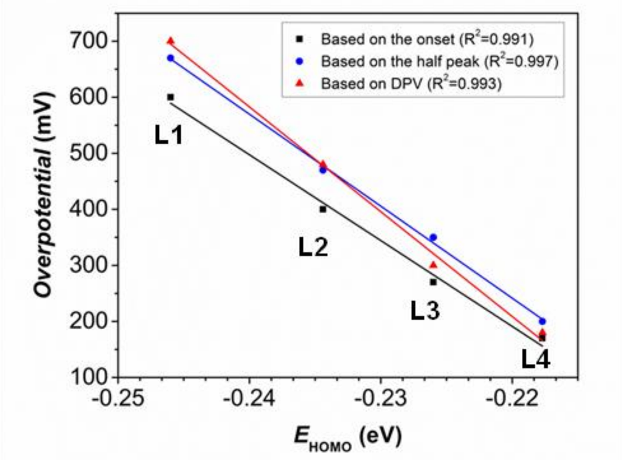

Figure 4.12 Correlation between the experimental overpotential obtained from the wave onset (black), the half peak potential (blue) or the differential pulse voltammetry (red) and the HOMO energy of the free ligands.

To confirm that only the ligand affects the catalytic wave, we constructed a correlation graphic of the overpotential with the different complexes and the energy of the HOMO orbital of the free ligand, which is strongly related with the ligand based oxidation (Figure 4.12). The correlation found was excellent, with r^2 values above 0.99. The good relationship did not depend on the specific experimental measurement used, as it worked for either (the onset of the wave, or the half peak or the Differential Pulse Voltammetry (DPV) value). The results undoubtedly assign the electrocatalytic wave to the ligand oxidation as well as discard the possibility of free copper as responsible of water oxidation.

Conclusion

The development of clean ways for energy production is urgent. In this context, water splitting is one of the most promising technologies and efficient and robust catalysts are needed, especially for the water oxidation reaction, which is the bottleneck of the process. Herein, we have developed a new family of mononuclear copper-based water oxidation catalyst. The full control of the overpotential was achieved through modifications in the electronic structure of the ligand, reaching a record value of 170 mV.

The computational mechanistic investigation has given light to the rational modification of the system, demonstrating that the catalytic wave is associated with the ligand oxidation. In addition, a new mechanism for oxygen-oxygen bond formation step has been discovered. This pathway complements the classic water oxidation mechanisms, the interacion between two M-O fragments (I2M) and the water nucleophilic attack (WNA).

We could compute accurately the full catalytic cycle by means of density functional theory calculations (Figure 4.13). The reaction starts with the reversible oxidation of the initial [Cu(II)-L_1] catalyst. Then, the second oxidation produces the active species after the coordination of an hydroxo group. This oxidation is mainly located on the ligand. This complex electronic structure opens the door to a new oxygen-oxygen bond formation mechanism, the single electron transfer-water nucleophilic attack (SET-WNA), which consists of two consecutive one electron oxidations of the reacting oxygen centers.

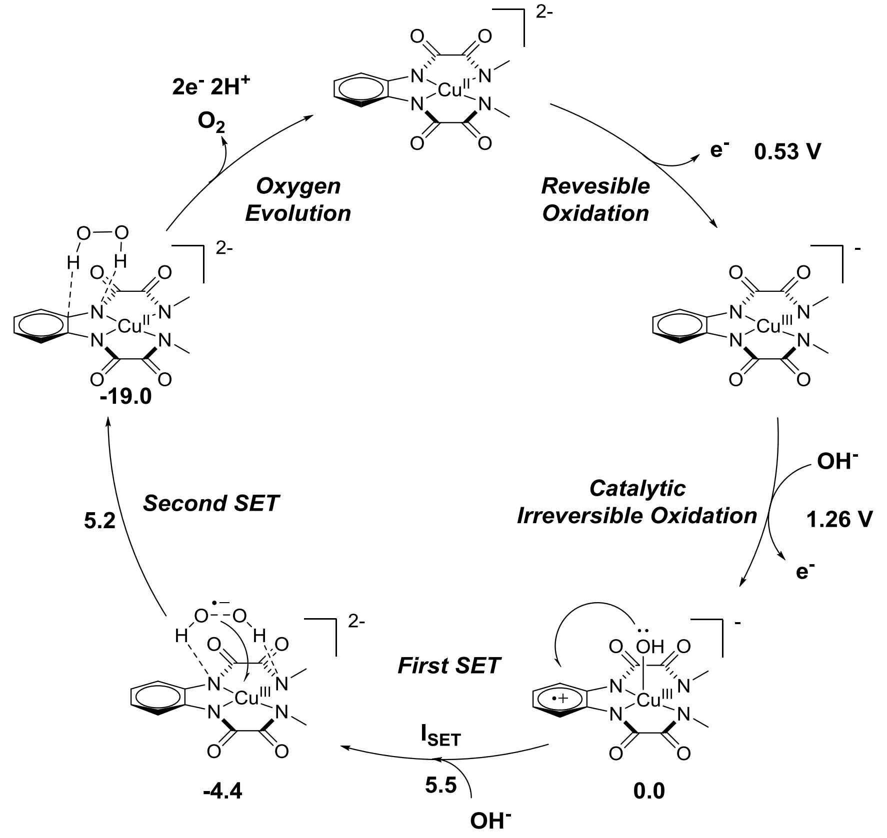

Figure 4.13 Full catalytic cycle of [Cu(II)-L$_1$] catalyzed water oxidation reaction. Oxidation potentials in Volts and free energies in kcal/mol.

The first single electron transfer produces a previously unknown intermediate with the oxygens partially oxidized, forming a three electrons two centers bond, which a partial bond order of 0.5 between oxygens due to the presence of two electrons in the bonding orbital and one in the antibonding orbital. Finally, there is a transition state that connects this species to the peroxo intermediate. This transition state has two open shells despite being a doublet, and involves the release of the antibonding electron from the O-O moiety to the copper(III) center.

Finally, the oxygen evolution takes place easily by consecutive one electron oxidation and proton coupled electron transfer at low potentials. The calculated barriers are in agreement with the experimental result about the rate determining step, which is the second electron transfer to activate the catalyst. Our conclusions were further confirmed by the backbone modification of the ligand, that could reduce the overpotential until 170 mV.

Scheme 4.8 Schematic representation of oxygen-oxygen bond formation mechanisms: I2M, WNA and SET-WNA. The numbers on oxygen indicates the oxidation state of O atoms.

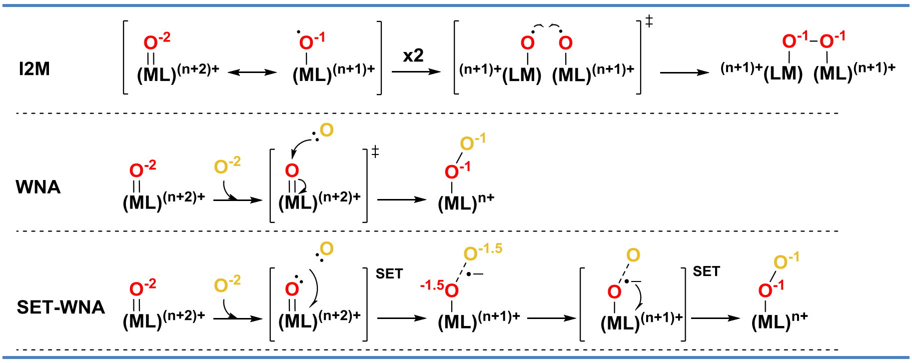

Apart from the study of the new copper water oxidation catalyst, the computational investigation allowed to discover a new oxygen-oxygen bond formation pathway (Scheme 4.8). Therefore, we extended the mechanistic picture of the water oxidation to three main pathways. The interaction between two metals is based on the coupling of two metal-oxyl fragments. In this mechanism the oxidation state of the metal does not change. The second mechanism is the water nucleophilic attack, which consists on the nucleophilic attack of an external water molecule, releasing one proton to the media and forming the hydroperoxo moiety by two electron metal reduction. Finally, the single electron transfer-water nucleophilic attack occurs by two consecutive single electron transfers from the reactive oxygens to the metal. This mechanism is a promising alternative for the first row transition metals, where the oxidation states and spin state are more flexible and the single electron transfers are favoured, especially when high oxidation state cannot be reached, as in copper.

4.4 Extending the SET-WNA Mechanism to Other Systems

Reaction overview of other Cu-based WOC

The development of new catalyst for water oxidation is still a challenge and first row transition metals have became a promising option to improve the sustainability and to reduce the cost associated to the process. However, the lack of mechanistic investigations on these systems implies drawbacks for the advancement of the field. We have demonstrated in the section above that a new mechanism, the single electron transfer-water nucleophilic attack, operates in the oxygen-oxygen bond formation step in a family of copper based water oxidation catalysts.

Scheme 4.9 Catalyst structures for the computational study of SET-WNA mechanism in other systems. The experimental pH and the redox potential of the catalytic wave (in V versus NHE) are shown below each catalyst.

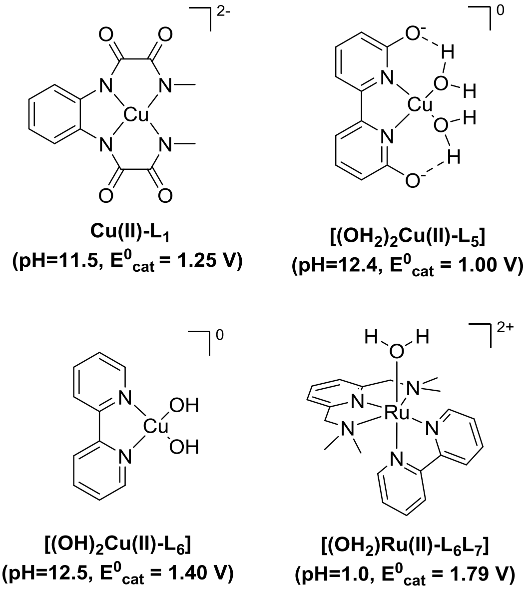

Cu(II)-L$_1$
(pH=11.5, E^0_{cat} = 1.25 V)

[$(OH_2)_2$Cu(II)-L$_5$]
(pH=12.4, E^0_{cat} = 1.00 V)

[$(OH)_2$Cu(II)-L$_6$]
(pH=12.5, E^0_{cat} = 1.40 V)

[(OH_2)Ru(II)-L$_6$L$_7$]
(pH=1.0, E^0_{cat} = 1.79 V)

Thus, the extension of this mechanism to other copper-based water oxidation catalysts seems necessary to complete the mechanistic scenario of WOC. SET-WNA implies different electronic requirements (flexible spin states, single electron transfer processes), so the demonstration of the generality of this pathway would help in the rational development of new catalysts. We selected two copper systems which differs considerably from [Cu(II)-L_1] to cover a wider chemical space (Scheme 4.9). The first one, [$(OH_2)_2$Cu(II)-L_5],[23] is based on a redox active ligand also, but bidentate instead of tetradentate. Therefore the chemical structure and the reactive site are totally different from our catalyst, as the reactive water molecules are coordinated in the plane. The other catalyst, [$(OH)_2$Cu(II)-L_6],[21] is the most active copper-based water oxidation catalyst up to date, although at higher overpotential. The reason is that the bipyridine ligand is not redox active in this case and therefore this catalyst must have spin in either copper of an oxo (thus oxyl) group. In addition, we also wanted to check the feasibility of SET-WNA in a well-established ruthenium water oxidation catalyst, [(OH_2)Ru(II)-L_6L_7].[27] For this reason, we applied the new methodology to a previously reported Ru complex, which has been studied before experimentally and computationally and has been proved to form the oxygen-oxygen bond through water nucleophilic attack.

Catalytic cycle of [$(OH_2)_2$Cu(II)-L_5]

We selected the catalyst [$(OH_2)_2$Cu(II)-L_5], where L_5 is [2,2'-bipyridine]-6,6'bis(olate) (see Scheme 4.9) to continue our investigation on the oxygen-oxygen bond formation step in copper based water oxidation catalysis. This system was reported by Lin and co-workers in 2014, and promotes the water oxidation efficiently at basic pH (12.4), with a catalytic wave at 1.00 V. In addition, some preliminary calculations were also reported, showing that the active species is based also in a redox-active ligand. This complex is structurally very different from the Cu(II)-L_1 complex discussed above because two water molecules are coordinated in plane and no free apical position is available for the catalysis. Thus, it is a good example to check if the SET-WNA mechanism operates in other copper systems.

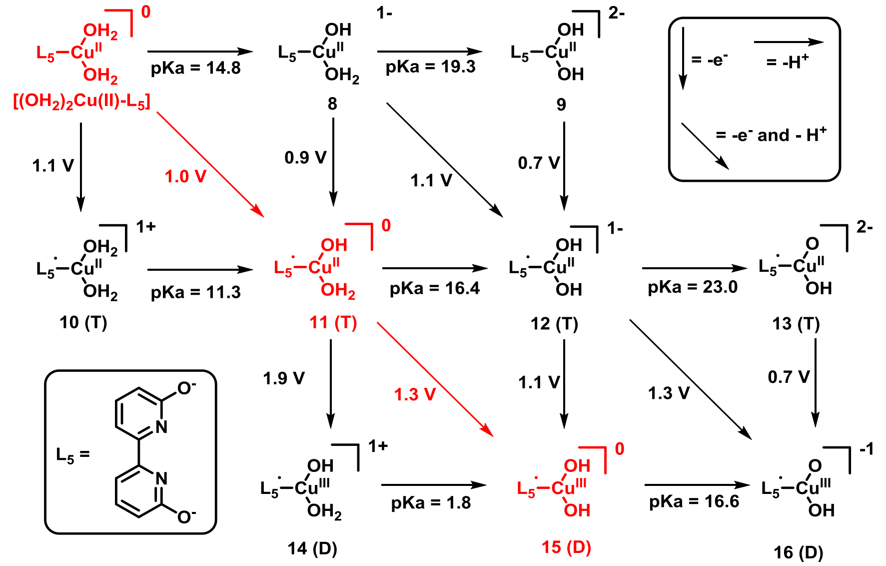

Figure 4.14 Thermodynamic scheme of $[(OH_2)_2Cu(II)\text{-}L_5]$ activation to form the active species. The lowest energy pathway is highlighted in red.

The thermodynamic cycle for the electrochemical catalyst activation was studied using our methodology (see section 4.2 for details). These calculations had also been carried out by Lin and co-workers in the original paper, who arrived to the same active species through a different pathway. We found that two consecutive proton coupled electron transfers (PCET) at 1.0 and 1.3 V respectively, produce the active species 15, which is a Cu(III) species with the ligand oxidized. The main difference comes from the computed energies for the intermediates after the first oxidation. We always found the triplet state more stable than the singlet, while in the pathway proposed by Lin and co-workers the triplet state was not considered. The chemical interpretation of these data leads to the conclusion that the first oxidation is based on the ligand and not on the copper. This is consistent with the chemical structure of the ligand, which has two enolate groups that can be oxidized very easily. In addition, the deprotonation of the initial catalyst has a pKa of 14.8, close to the experimental pH. If the first proton is removed, the first oxidation can be produced at 1.1 V by PCET and the second electron transfer at the same potential, explaining the observation of only one wave in the cyclic voltammetry. The pKa values and electric potentials are very sensitive to the energies, as little variations can change the order of pKa values in almost 1 or 2 units. For these reasons, we cannot conclusively assign a single pathway to the electrochemical formation of the active catalyst. This notwithstanding, the active species is undoubtedly intermediate **15** because is much more stable than alternative species **14** or **16**.

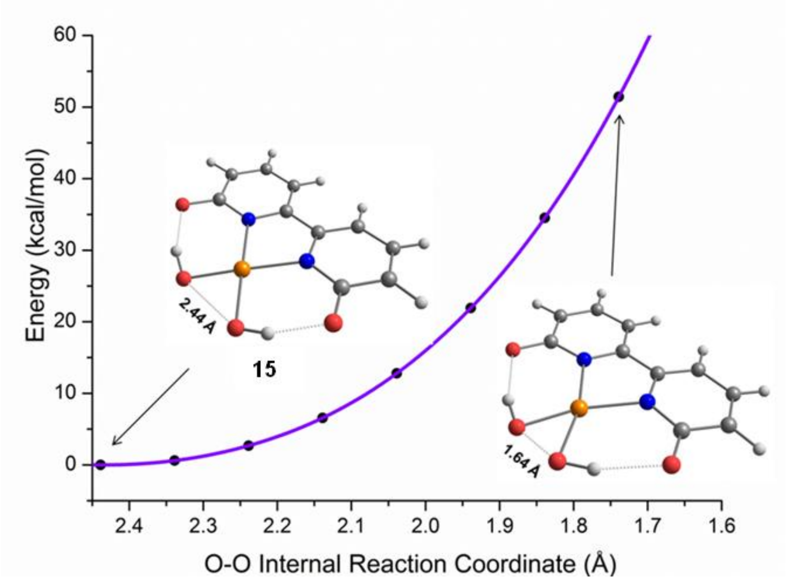

Figure 4.15 Potential energy relaxed scan of intramolecular HO---OH reductive elimination from intermediate **15**.

Then, we analyzed the possibility of an intramolecular reductive elimination because two OH groups are present in the active species **15** (Figure 4.15). The potential energy scan increases in energy dramatically when the O-O bond distance is reduced, up to more than 50 kcal/mol at 1.64 Å. A plausible explanation relies on the fact that during this step, two electrons are released to the copper center, forming an unstable "Cu(I)" species where the ligand is still oxidized. For this reason, we thought that two single electron transfers, one to the ligand and the other to the copper would be favored also in this case.

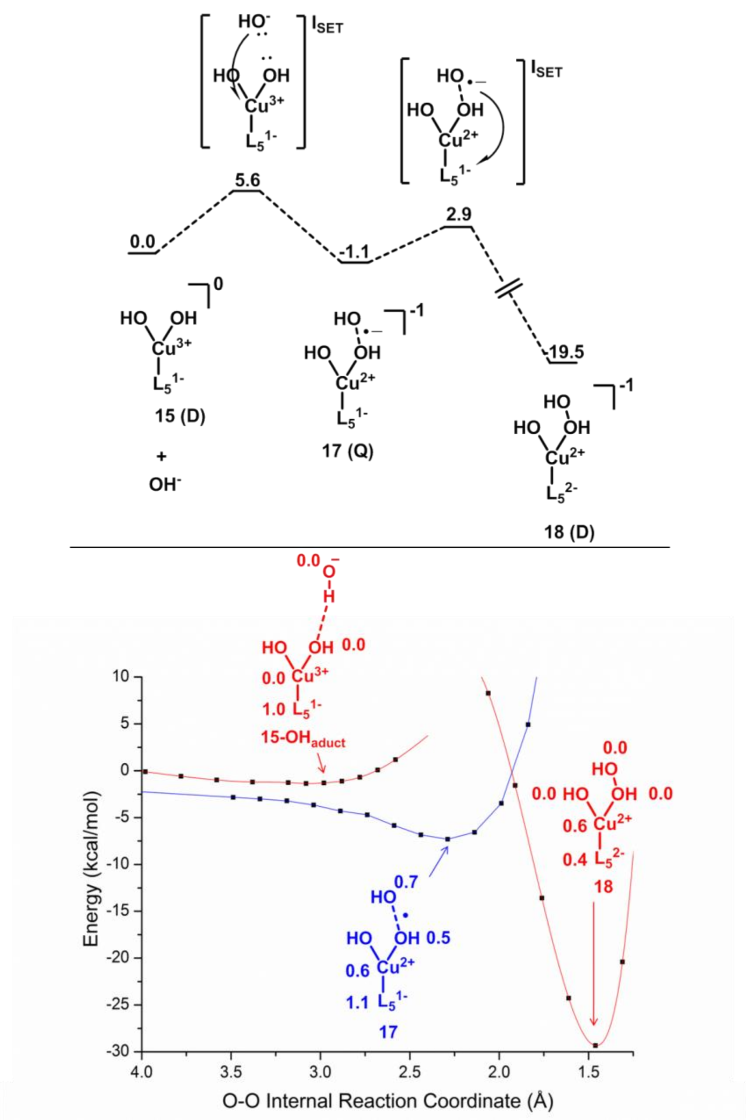

Figure 4.16 Free energy profile of the intermolecular O-O bond formation step through SET-SNA mechanism from the active species **15** (top). Energies in kcal/mol. Potential energy relaxed scan of O-O internal reaction coordinate with spin densities in key structures (bottom).

So, we carried out the calculations of the intermolecular pathway. Again, the first single electron transfer occurs without potential energy barrier. Actually, the reduction of the catalyst takes place firstly in the ligand, producing the 2c3e species **17** in the quartet state through an outer sphere electron transfer at 3.1 Å. Then, an avoided crossing point is obtained and the estimation of the free energy change associated with this process comes from the free energy of the adduct **15-OHAdduct** at 5.6 kcal/mol above the separated reactants. Species **17** is 1.1 kcal/mol more stable than the initial point, proving that the 2-center 3-electron interaction is strong enough to overcome the entropy loss of getting together the two fragments. Finally, the peroxo species **18** is produced through a minimum energy crossing point (MECP) between quartet and doublet surfaces, reducing the ligand by one electron, which comes from the antibonding orbital of the HO---OH moiety. We could not locate this MECP for technical reasons but we could estimate its energy from the potential energy scan, to a value about 2.9 kcal/mol. The technical problem is related to the existence of a doublet state with extra open shells in the region where the O-O bond distance is above 2.0 Å. This “open shell double” coexists with the quartet and the normal doublet spin state. The calculation oscillates between the two doublet electronic states, which precludes convergence. This problem does not exist when considering singlet-triplet crossing because the SCF function can be constrained to the closed-shell singlet, with no spin contamination in the program developed by Harvey and co-workers.[51] The overall barrier of this step is very small, and because of this we decided not to press further the issue.

It is interesting to compare species **17** with intermediate **2** from the previous section. Structurally, species **2** has a square planar ligand and the fragment forming the O--O bond stays on the apical position by hydrogen bonding of HO---OH moiety to the catalyst ligand.

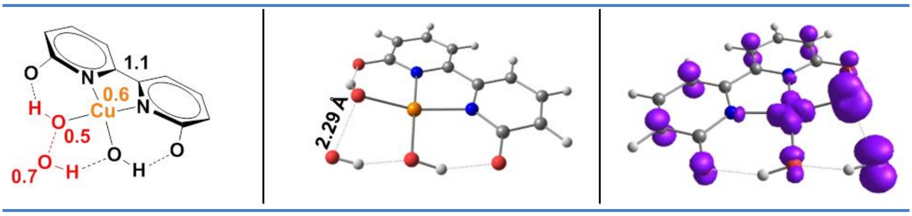

Figure 4.17 Representation of 2c3e HO---OH-Cu(III) structure **17**. 2D molecule with spin densities (left), 3D structure with the O-O bond length interaction in Å (center) and 3D structure with spin density distribution (right).

In contrast, structure **17** has a bidentate ligand and two hydroxo group that react to form the O-O bond (Figure 4.17). Moreover, the electronic structure of the catalysts is different, a quartet state in **17**, with Cu(II) and the ligand oxidized, and a doublet state in **2**, with Cu(III) and the ligand reduced. Despite these differences, the HO---OH moieties share the same characteristics in both intermediates: the sum of the spin densities in the oxygen atoms is very close to 1 (0.5 to 0.7 on each oxygen), the bond length is 2.30 and 2.29 Å, in **2** and **17** respectively, and the spin density distribution is practically the same, with the unpaired electron in the antibonding orbital of HO---OH moiety. This represents a generalitation of the SET-WNA mechanism, where the 2c3e species is essential after the first single electron transfer.

Thus, $[(OH_2)_2Cu(II)\text{-}L_5]$ catalyzed water oxidation occurs also through the SET-WNA mechanism, despite the structural and electronic differences from the previously discussed catalyst Cu(II)-L_1.

Catalytic cycle of $[(OH)_2Cu(II)\text{-}L_6]$

After the mechanistic study on copper-based water oxidation catalysts with redox active ligands, we wondered if the SET-WNA mechanism could operate in a different system, the simple $[(OH)_2Cu(II)\text{-}L_6]$, where L_6 is bipyridine. This ligand is not redox active and this was confirmed by previous calculations before.[23] This catalyst was reported by Mayer and co-workers in 2012. It is very active, with a catalytic TOF of 100 s^{-1} and robust, operating at 1.40 V and 12.5 pH.

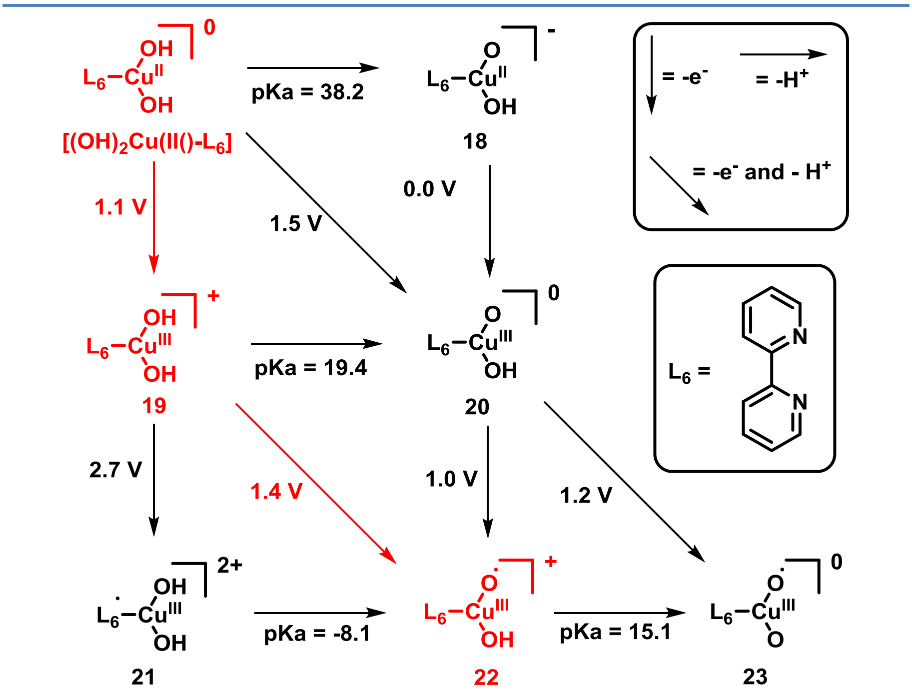

Figure 4.18 Thermodynamic scheme of [(OH)$_2$Cu(II)-L$_6$] activation to form the active species. The lowest energy pathway is highlighted in red.

As for the previous catalysts, we calculated the electrochemical activation of the system using our methodology (described in section 4.2). The formation of the active species is highlighted in red in Figure 4.18. This time, our calculations are in agreement with those previously reported, and the activation process consists on an electron transfer at 1.1V followed by a proton coupled electron transfer (PCET) at 1.4 V. In that way, the active species **22** is formed. It has no spin density on the ligand and all spin is concentrated on the oxygen (spin ~ 1), which forms a Cu(III)-O· unit. This behaviour is totally different respect to the other copper catalysts studied, as here the reactive oxygen is already in the oxidation state -1. Logically, the formation of this highly reactive intermediate costs more energy than in the other cases, with a potential of 1.4 V. This result is consistent with the very high activity of the catalyst.

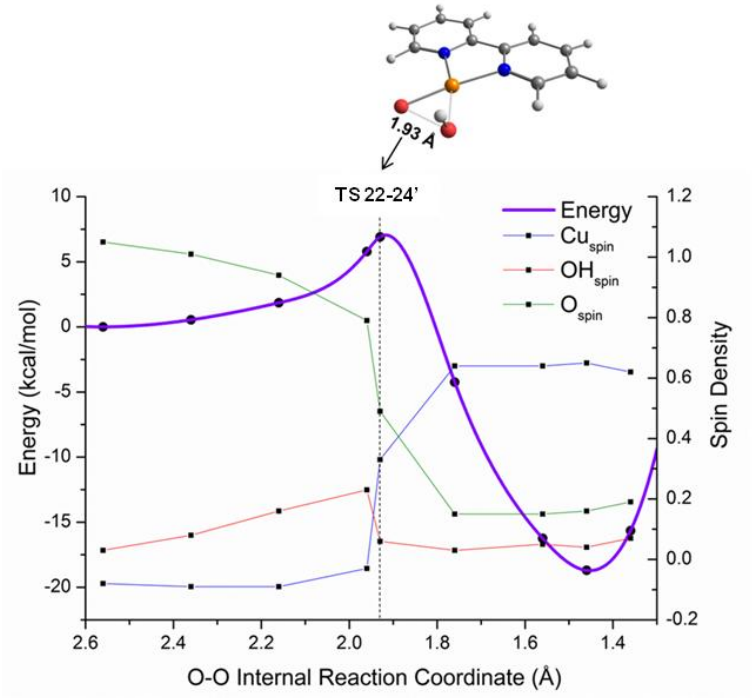

Figure 4.19 Potential energy relaxed scan of intramolecular HO---O• reductive coupling from intermediate **22**.

As no ligand oxidation has taken place, we decided to study the intramolecular oxygen-oxygen formation. Unlike in $[(OH_2)_2Cu(II)\text{-}L_5]$, the potential energy relaxed scan (Figure 4.19) of the intramolecular reductive elimination shows a standard reactive curve. This reductive coupling between OH and O· is similar to the previously reported by Zhang and co-workers in a copper dimer.[52] The free energy of the calculated TS 22-24' is 7.0 kcal/mol above the active species **22**. To understand the electron rearrangement during the reaction coordinate, we analyzed the spin density on Cu (in blue), OH (in red) and O (in green) fragments along the scan. The initial steps showed similar electronic structure than **22**, with Cu(III) (spin ~ 0), OH ligand with little spin density and the oxyl ligand with spin density close to 1. However, in the transition state, the spin density distribution changes dramatically. The free electron is located between Cu and O, representing the one electron reduction process of the metal center. Finally, the peroxo group is formed and copper is already reduced to Cu(II), delocalizing some of the spin density with the ligands.

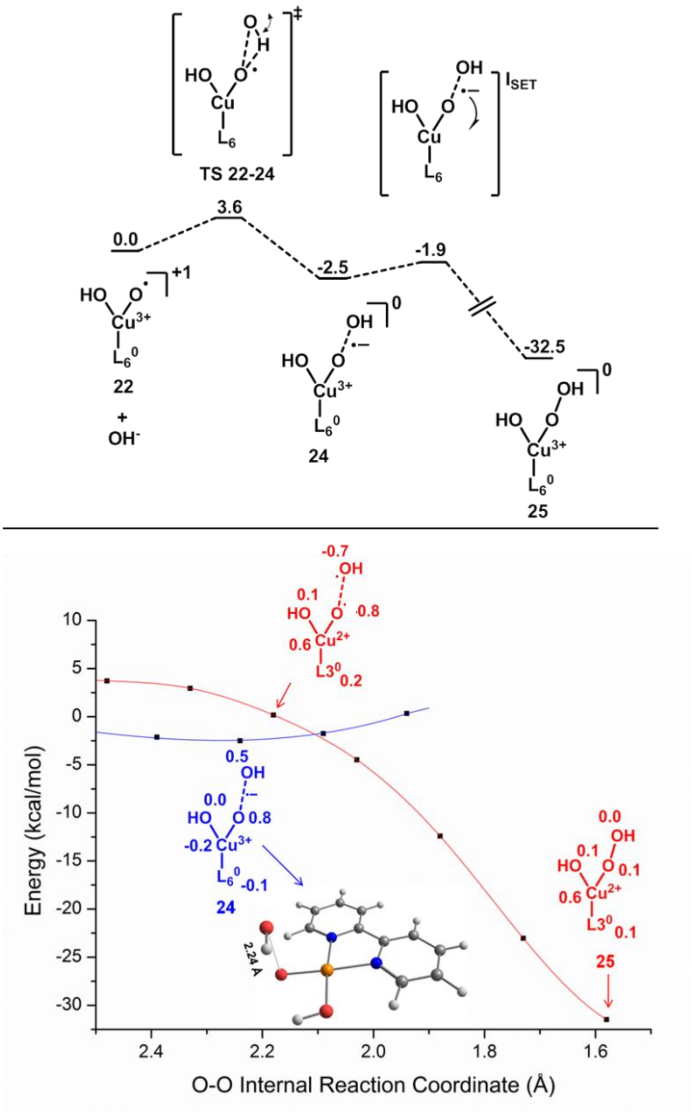

Figure 4.20 Free energy profile of the intermolecular O-O bond formation step through SET-SNA mechanism from the active species **22** (top). Energies in kcal/mol. Potential energy relaxed scan of O-O internal reaction coordinate with spin densities in key structures (bottom).

In order to complete the mechanistic picture of this catalyst, we studied in detail the intermolecular mechanism. Again, single electron transfer-water nucleophilic attack is the preferred way for the O-O bond formation. This time, one of the oxygens is already oxidized in **22** and for this reason only one single electron transfer should take place to generate the oxygen-oxygen bond. However, we found a previous transition state that reoriented the incoming OH group to form the 2c3e interaction in species **24**. Remarkably, the electronic structure of intermediate **24** shares a lot of similarities with species **2** and **17**. The spin density on the oxygens is again close to 1 and the bond length is 2.24 Å, little smaller than in the other species because one of the interacting oxygens is deprotonated. We did not found a transition state of the second electron transfer because the potential energy scan showed that both curves are in different electronic surfaces (there is an actual crossing between them). We estimated as in other cases the free energy of this single electron transfer in only 0.6 kcal/mol, which is consistent with the highly reactive oxyl intermediate. Thus, the overall barrier of the intermolecular SET-WNA is only 3.6 kcal/mol, 3.4 lower than the intramolecular pathway.

We recapitulate all the mechanistic information on this catalyst in the catalytic cycle of Figure 4.21. The active species **22** is formed by two consecutive oxidations, the first one at 1.1 V and the second one, a proton coupled electron transfer, at 1.4 V. The reactive intermediate **22** is already oxidized on the Cu-O bond, forming an oxyl ligand that can react in two different ways. The first one is highlighted in red and implies the intramolecular reductive coupling, with a barrier of 7.0 kcal/mol. The second one, highlighted in blue, is again a single electron transfer-water nucleophilic attack by an external hydroxide. As oxyl was already oxidized, only one single electron transfer is needed to produce the peroxo moiety, although a previous reorganization of the incoming hydroxide has an associated barrier of 3.6 kcal/mol. The intermolecular pathway is therefore more favored than the intramolecular one and the low barriers confirm the high activity demonstrated by the catalyst experimentally, with a TOF of 100 s^{-1}. The mechanistic studies on the three different copper catalysts reveal that SET-WNA is common in copper catalyzed water oxidation and it must be considered to complete the mechanistic picture.

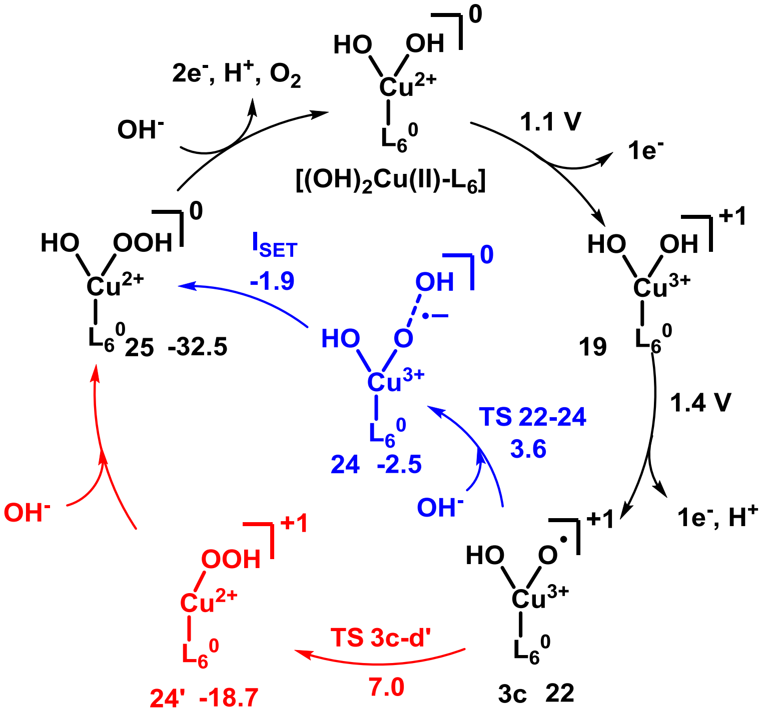

Figure 4.21 Full catalytic cycle of water oxidation for $[(OH)_2Cu(II)\text{-}L_6]$ catalyst. Intramolecular and intermolecular pathways in red and blue. Redox potentials in Volts versus NHE and free energies in kcal/mol.

Extension of SET-WNA to ruthenium catalysis

In order to explore how the SET-WNA mechanism can operate in other transition metals, such as ruthenium, where the WNA mechanism has been well established, we analyzed the formation of the partially oxidized HO---OH moiety in a well-known system, $[(OH_2)Ru(II)\text{-}L_6L_7]$ (L_6 is bipyridine and L_7 is 2,6-bis((dimethylamino)-methyl)pyridine).[27]

The activation steps of this system were studied both experimentally and computationally, with three consecutive oxidations at 0.83, 0.97 and 1.79 V versus NHE, forming the active Ru(V) species **26**. Cramer and Llobet studied the WNA mechanism and they found a free energy barrier of 20.7 kcal/mol, forming the Ru(III)-OOH species.

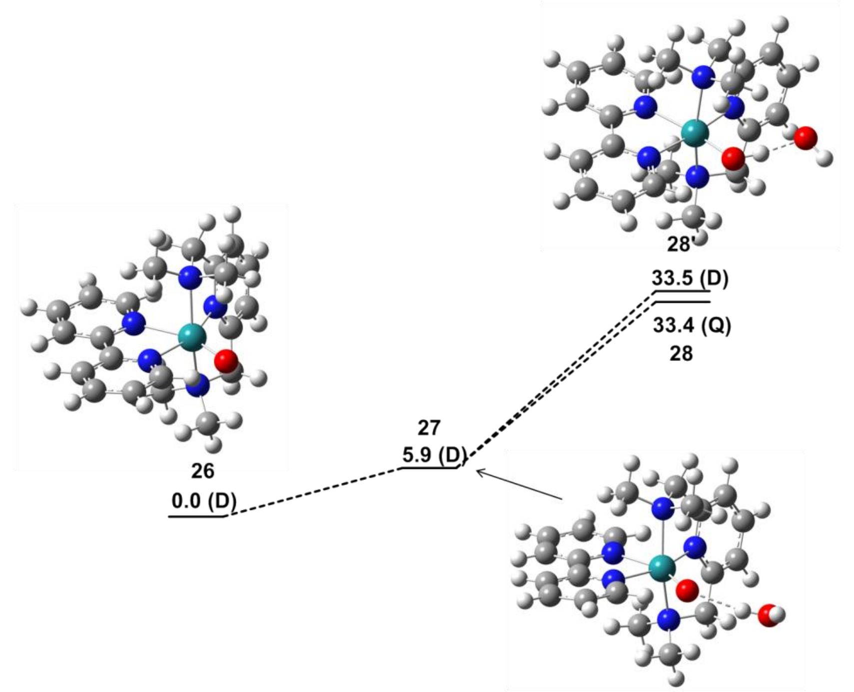

Figure 4.22 Free energy profile of the generation of Ru(IV)-OH---HO• intermediate from active species of [(OH$_2$)Ru(II)-L$_6$L$_7$] catalyst. Energies in kcal/mol.

We tried to drag the system towards a SET-WNA mechanism from intermediate **26**. The interaction of a water molecule (or hydroxide) with the M=O bond does not produced the desired 2c3e interaction. For this reason, we tried to force this type of species by the transfer of a hydrogen radical from the external water molecule analogously to what happens in the R-H activation chemistry previously reported in iron chemistry.[53] Using this approach, Ru(IV) species **28** and an external OH radical were formed. But the relative free energy was as high as 33.4 kcal/mol. This prohibitive energy is associated with the intrinsic instability of OH radical, which is not stabilized through the 2c3e interaction that we reported in the copper systems. In this case, the OH group attached to the metal center only delocalizes its electron with the metal. There is no interaction between the reactive oxygens, discarding the SET-WNA mechanism for this Ru catalyst. This behavior is likely to occur also in similar systems, where the single electron transfers are not favoured, such in other Ru or Ir catalysts.

Conclusion

The Single Electron Transfer-Water Nucleophilic Attack mechanism has been extensively discussed along this chapter, demonstrating the wide applicability of this mechanism to different copper-based water oxidation catalysts. Thus, this mechanism has to be added to the list of oxygen-oxygen bond formation mechanism, especially when first row transition metals are involved. The mechanism is however not universal as proved for the ruthenium case. When the single electron transfer is not favored, as in noble metals, SET-WNA will be higher in energy. We are still working on the study of the extension of this mechanism to other first row transition metals.

The formation of an oxygen-oxygen bond can be schematically explained as the abstraction of two or more electrons from a metal catalyst (electrochemically, chemically or photochemically) and the subsequent consecutive two-electron oxidation of the water (or hydroxo) molecules by the catalyst, forming the peroxo unit. We have drawn a general picture of the available mechanisms for oxygen-oxygen bond formation in a single view (Scheme 4.10). The scheme is as general as possible, so the protonation state of the oxygens along the pathways is not discussed here. We divided the oxygen-oxygen bond formation in three different steps: the metal reversible activation, the complex irreversible activation and the oxygen-oxygen bond formation step.

Scheme 4.10 Overview of the mechanistic scenario for oxygen-oxygen bond formation mechanism in water oxidation reaction. The numbers on the oxygens represent the oxidation state. The directly attached oxygen to the metal is represented in red and the incoming oxygen is represented in yellow.

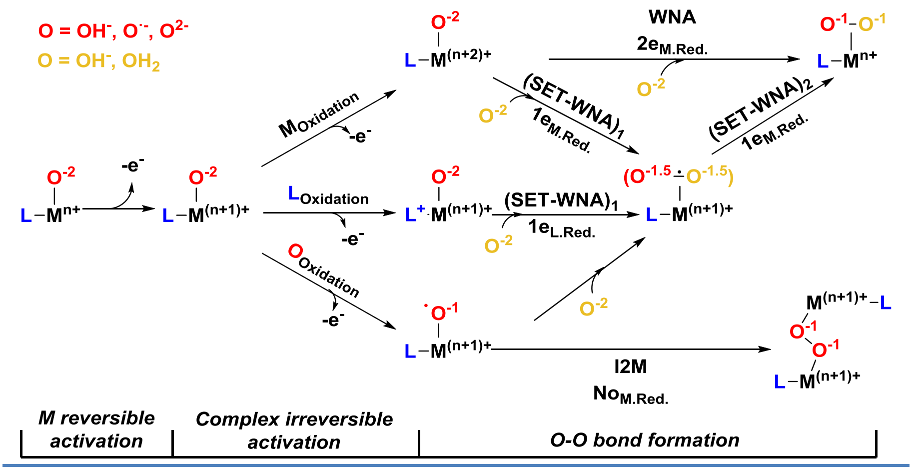

The first one, called M reversible activation, represents the reversible oxidation of the initial catalyst, which is associated with the reversible waves in cyclic voltammetries. After, the second oxidation corresponds to the irreversible activation, leading to the active species. Depending on the site of electron abstraction, there are three different possibilities: the metal can be oxidized directly, as in the $[(OH_2)Ru(II)\text{-}L_6L_7]$ example above, the electron can be removed from the ligand, if it is redox-active, as in the case of $[Cu(II)\text{-}L_1]$ and $[(OH_2)_2Cu(II)\text{-}L_5]$ or the last option, when the metal is not easily oxidized and the electron is removed directly from the oxygen attached to the metal, as in $[(OH)_2Cu(II)\text{-}L_6]$. This option implies usually a higher overpotential but generates a very active species, since oxygen is already oxidized.

Afterwards, when the system is fully oxidized, the active species is ready for the O-O bond formation. There are again three different pathways, the interaction of two M-O units (I2M), the water nucleophilic attack (WNA) and the single electron transfer-water nucleophilic attack (SET-WNA). When the metal reaches a high oxidation state, and a metal polarized M=O bond is present in the active species, the complex can be attacked by an external water molecule, which acts as nucleophile. The oxygen-oxygen bond is form at the same time that the metal is reduced by two electrons through a single transition state. This WNA is the most common pathways for second- or third-row transition metals, as in [$(OH_2)Ru(II)-L_6L_7$]. The second well-recognized mechanism is I2M and takes place when an accessible oxyl species is present on the molecule and the oxidation state of the oxygen is actually -1, so the O-O bond formation is produced by the collapse of two of these fragments. During this mechanism, the metal does not formally change its oxidation state and two fragments come together, so the charge of each fragment should be low to prevent repulsion. Finally, we introduced a new mechanism, the SET-WNA, which complements the others in the cases in which there is a redox-active ligand or when a metal-oxyl species is attacked by an external water (or hydroxo) molecule. In this case, two consecutive single electron transfers occur from the oxygens to the catalysts. This implies that a stable intermediate is reached after the first SET, forming a partially oxidized O---O moiety, with two electrons in the σ bonding orbital and one electron in the σ* antibonding orbital. This interaction has a formal bond order of 0.5 and the bond length is around 2.30 Å. This mechanism has been demonstrated for three different copper based water oxidation catalysts.

In conclusion, the SET-WNA mechanism has been extended from the initial [$Cu(II)-L_1$] system of section 4.3 to other two catalysts, demonstrating its generality and becoming a new tool for water oxidation mechanistic studies. It complements the previously reported WNA and I2M pathways and fits well with first-row transition metal features, the flexibility of spin states, the facility of single electron transfer and its ability of playing with redox active ligands. For this reason, we think that it will help in the development of new catalyst and in the mechanistic study of new systems.

4.5 References

[1] Data taken from 2016 BP Statistical Review available at www.bp.com/statisticalreview.

[2] Lacis, A. A.; Schmidt, G. A.; Rind, D.; Ruedy, R. A. *Science* **2010**, *330*, 356-359.

[3] Melis, A. *Energy Environ. Sci.* **2012**, 5, 5531-5539.

[4] Gust, D.; Moore, T. A.; Moore, A. L. *Acc. Chem. Res.* **2009**, *42*, 1890−1898.

[5] Nowotny, J.; Sorrell, C. C.; Sheppard, L. R.; Bak, T. *Int. J. Hydrogen Energy* **2005**, *30*, 521-544

[6] Youngblood, W. J.; Lee, S.-H. A.; Kobayashi, Y.; Hernandez-Pagan, E. A.; Hoertz, P. G.; Moore, T. A.; Moore, A. L.; Gust, D.; Mallouk, T. E. *J. Am. Chem. Soc.* **2009**, *131*, 926-927

[7] Sun, L.; Hammarstrom, L.; Akermark, B.; Styring, S. *Chem. Soc. Rev.* **2001**, *30*, 36-49.

[8] Dau, H.; Limberg, C.; Reier, T.; Risch, M.; Roggan, S.; Strasser, P. *ChemCatChem* **2010**, *2*, 724-761.

[9] McCrory, C. C. L.; Jung, S.; Peters, J. C.; Jaramillo, T. F. *J. Am. Chem. Soc.* **2013**, *135*, 16977-16987.

[10] Garrido-Barros, P.; Gimbert-Suriñach, C.; Matheu, R.; Sala, X.; Llobet, A. *Chem. Soc. Rev.* **2017**, *Advance Article.* DOI: 10.1039/C7CS00248C.

[11] Creus, J.; Matheu, R.; Peñafiel, I.; Moonshiram, D.; Blondeau, P.; Benet-Buchholz, J.; García-Antón, J.; Sala, X.; Godard, C.; Llobet, A. *Angew. Chem. Int. Ed.* **2016**, *55*, 15382-15386.

[12] Francas, L.; Richmond, C.; Garrido-Barros, P.; Planas, N.; Roeser, S.; Benet-Buchholz, J.; Escriche, L.; Sala, X.; Llobet, A. *Chem. Eur. J.* **2016**, *22*, 5261-5268.

[13] Gersten, S. W.; Samuels, G. J.; Meyer, T. J. *J. Am. Chem. Soc.* **1982**, *104*, 4029-4030.

[14] Duan, L.; Bozoglian, F.; Mandal, S.; Stewart, B.; Privalov, T.; Llobet, A.; Sun, L. *Nat. Chem.***2012**, *4*, 418-423

[15] Matheu, R.; Ertem, M. Z.; Benet-Buchholz, J.; Coronado, E.; Batista, V. S.; Sala, X.; Llobet, A. *J. Am. Chem. Soc.*, **2015**, *137*, 10786-10795.

[16] Karkas, M. D.; Verho, O.; Johnston, E. V.; Akermark, B. *Chem. Rev.* **2014**, *114*, 11863-12001.

[17] Ellis, W. C.; McDaniel, N. D.; Bernhard, S.; Collins, T. J. *J. Am. Chem. Soc.* **2010**, *132*, 10990-10991.

[18] Wasylenko, D. J.; Ganesamoorthy, C.; Borau-Garcia, J.; Berlinguette, C. P. *Chem. Commun.* **2011**, *47*, 4249−4251

[19] Dogutan, D. K.; McGuire, R.; Nocera, D. G. *J. Am. Chem. Soc.* **2011**, *133*, 9178-9180.

[20] Han, Y.; Wu, Y.; Lai, W.; Cao, R. *Inorg. Chem.* **2015**, *54*, 5604-5613.

[21] Barnett, S. M.; Goldberg, K. I.; Mayer, J. M. *Nat. Chem.* **2012**, *4*, 498-502.

[22] Zhang, M.-T.; Chen, Z.; Kang, P.; Meyer, T. J. *J. Am. Chem. Soc.* **2013**, *135*, 2048-2051.

[23] Zhang, T.; Wang, C.; Liu, S.; Wang, J.-L.; Lin, W. *J. Am. Chem. Soc.* **2014**, *136*, 273-281.

[24] Sala, X.; Maji, S.; Bofill, R.; Garcia-Anton, J.; Escriche, L.; Llobet, A. *Acc. Chem. Res.* **2014**, *47*, 504-516.

[25] Neudeck, S.; Maji, S.; López, I.; Meyer, S.; Meyer, F.; Llobet, A. *J. Am. Chem. Soc.* **2014**, *136*, 24-27.

[26] Richmond, C. J.; Matheu, R.; Poater, A.; Favilene, L.; Falivene, Benet-Buchholz, J.; Sala, X.; Cavallo, L.; Llobet, A. *Chem. Eur. J.* **2014**, *20*, 17282-17286.

[27] Vigara, L.; Ertem, M. Z.; Planas, N.; Bozoglian, F.; Leidel, N.; Dau, H.; Haumann, M.; Gagliardi, L.; Cramer, C. J.; Llobet, A. *Chem. Sci.* **2012**, 3, 2576-2586

[28] Concepcion, J. J.; Tsai, M. -K.; Muckerman, J. T.; Meyer, T. J. *J. Am. Chem. Soc.* **2010**, 132, 1545-1557.

[29] Ertem, M. Z.; Gagliardi, L.; Cramer, C. J. Chem. Sci. **2012**, *3*,1293-1299.

[30] Liao, R.-Z.; Li, X.-C.; Siegbahn, P. E. M. *Eur. J. Inorg. Chem.* **2014**, 728-741.

[31] Ruiter, J. M.; Buda, F. *Phys. Chem. Chem. Phys.* **2017**, *19*, 4208-4212.

[32] Joepke, S. J.; Light, K. M.; VanNatta, P. E.; Wiley, K. M.; Kieber-Emmons, M. T. *J. Am. Chem. Soc.* Just Accepted Manuscript. DOI: 10.1021/jacs.7b03278.

[33] Gaussian 09, Revision **D.01**, Frisch, M. J.; Trucks, G. W.; Schlegel, H. B.; Scuseria, G. E.; Robb, M. A.; Cheeseman, J. R.; Scalmani, G.; Barone, V.; Mennucci, B.; Petersson, G. A.; Nakatsuji, H.; Caricato, M.; Li, X.; Hratchian, H. P.; Izmaylov, A. F.; Bloino, J.; Zheng, G.; Sonnenberg, J. L.; Hada, M.; Ehara, M.; Toyota, K.;

Fukuda, R.; Hasegawa, J.; Ishida, M.; Nakajima, T.; Honda, Y.; Kitao, O.; Nakai, H.; Vreven, T.; Montgomery, J. A., Jr.; Peralta, J. E.; Ogliaro, F.; Bearpark, M.; Heyd, J. J.; Brothers, E.; Kudin, K. N.; Staroverov, V. N.; Kobayashi, R.; Normand, J.; Raghavachari, K.; Rendell, A.; Burant, J. C.; Iyengar, S. S.; Tomasi, J.; Cossi, M.; Rega, N.; Millam, J. M.; Klene, M.; Knox, J. E.; Cross, J. B.; Bakken, V.; Adamo, C.; Jaramillo, J.; Gomperts, R.; Stratmann, R. E.; Yazyev, O.; Austin, A. J.; Cammi, R.; Pomelli, C.; Ochterski, J. W.; Martin, R. L.; Morokuma, K.; Zakrzewski, V. G.; Voth, G. A.; Salvador, P.; Dannenberg, J. J.; Dapprich, S.; Daniels, A. D.; Farkas, Ö.; Foresman, J. B.; Ortiz, J. V.; Cioslowski, J.; Fox, D. J. Gaussian, Inc., Wallingford CT, 2009.

[34] Balcells, D. *Adv. Organomet. Chem.* **2016**, *65*, 115-173.

[35] Becke, A. D. *J. Chem. Phys.* **1993**, *98*, 5648-5652.

[36] Gimme, S. Antony, J. Ehrlich, S.; Krieg, H. *J. Chem. Phys.* **2010**, *132*, 154104-19.

[37] Marenich, S. A. V.; Cramer, C. J.; Truhlar, D. G. *J. Phys. Chem.* B **2009**, *113*, 6378-6396.

[38] Roy, L. E.; Hay, P. J.; Martin, R. L. *J. Chem. Theory Comput.* **2008**, *4*, 1029-1031.

[39] a) Hehre, W.J.; Ditchfield, R.; Pople, J.A. *J. Chem. Phys.* **1972**, 56, 2257-2261. b) Hariharan, P.C.; Pople, J.A. *Theoret. Chimica Acta* **1973**, *28*, 213-222. c) Francl, M.M.; Petro, W.J.; Hehre, W.J.; Binkley, J.S.; Gordon, M.S.; DeFrees, D.J.; Pople, J.A. *J. Chem. Phys.* **1982**, *77*, 3654-3665.

[40] Lewis, A.; Bumpus, J. A.; Truhlar, D. G.; Cramer C. J. *J. Chem. Ed.* **2004**, *81*, 596-604.

[41] Lewis, A.; Bumpus, J. A.; Truhlar, D. G.; Cramer C. J. *J. Chem. Ed.* **2007**, *84*, 934-934 [Erratum].

[42] Marenich, A. V.; Majunmdar, A.; Lenz, M.; Cramer, C. J.; Truhlar, D. G. *Angew. Chem. Int. Ed.* **2012**, *51*, 12810-12814.

[43] Winikoff, S. G.; Cramer, C. J. *Catal. Sci. Technol.* **2014**, *4*, 2484-2489.

[44] Zhao, Y.; Schultz, N. E.; Truhlar, D. G. *J. Chem. Theory Comput.* **2006**, *2*, 364-382.

[45] Zhao, Y.; Truhlar, D. G. *J. Chem. Phys.* **2006**, *125*, 194101-18.

[46] Grimme, S. *J. Comp. Chem.* **2006**, *27*, 1787-1799.

[47] Chai, J. D.; Head-Gordon, M. *Phys. Chem. Chem. Phys.* **2008**, *10*, 6615-6620.

[48] Praneeth, V. K. K.; Ringenberg, M. R.; Ward, T. R. *Angew. Chem. Int. Ed.* **2012**, *51*, 10228-10234.

[49] Constentin, C; Drouet, S.; Robert, M.; Saveant, J.-M. *J. Am. Chem. Soc.* **2012**, 134, 11235-11242.

[50] Harcourt, R. D. *J. Am. Chem. Soc.* **1980**, *102*, 5195-5201.

[51] Harvey, J.N.; Aschi, M.; Schwarz, H.; Koch, W. *Theor. Chem. Acc.* **1998**, *99*, 95-99.

[52] Su, X. -J.; Gao, M.; Jiao, L.; Liao, R. -Z.; Siegbahn, P. E. M.; Cheng, J. -P.; Zhang, M. -T. **2015**, *54*, 4909-4914.

[53] Ye, S.; Geng, C.-Y.; Shaik, S.; Neese, F. *Phys. Chem. Chem. Phys.* **2013**, 15, 8017-8030.

Chapter 5

Conclusions

We have shown that Density Functional Theory calculations are very useful for the characterization of the mechanisms of redox reactions. We have extended the scarce knowledge on the field. The reported results will help in the rational design of new reactions in both the oxidative coupling and the water oxidation transformations.

The following paragraphs outline the most relevant conclusions on each chapter. More in-depth conclusions can be found in the last part of each section.

Chapter 2:

- We have developed a new Python program, called Goodvibes, which allows the user to easily apply quasi-harmonic corrections to the free energy calculation, as well as other important parameters such as temperature, concentration of frequency scaling factors.

- The thermodynamic cycle has been applied successfully to obtain an accurate estimation of the standard redox potential (SRP) of metal oxidations. The proper introduction of the corrections of the translational entropy in the cohesive energy and the electronic entropy in the ionization energy were found to be key to obtain accurate values of the SRP.

Chapter 3:

- The role of the oxidant in the rhodium-catalyzed oxidative coupling of benzoic acid and alkyne has been clarified. Both the copper diacetate and silver acetate oxidants cooperate intimately with the rhodium catalyst in the key reaction step, which we have labeled as cooperative reductive elimination. In this step, Rh(II) is formed instead of Rh(I), unveiling a new catalytic cycle based on Rh(III)-Rh(II)-Rh(III) transformations.

- The chemoselectivity of this coupling can be explained by the chemical structure of both oxidants. The bulkier structure of $[Cu(OAc)_2(H_2O)]_2$ blocks the CO_2 extrusion pathway, forming favorably the isocoumarin product. In contrast, $[Ag(OAc)]_2$ is planar, and stabilizes both competitive pathways, the cooperative reductive elimination and the CO_2 extrusion.

- The regioselectivity of the alkyne insertion step can be explained by the steric hindrance between the phenyl groups in the two reactants.

- The role of each of the components in the homocoupling of alkynes catalyzed by ruthenium and copper has been clarified. The ruthenium precursor is oxidized by oxygen at the initial stage of the reaction and later cooperates with the copper dimer to activate the carbazole C-H bonds at positions C1, C2 and C3. The cooperative reductive elimination takes place selectively at the C1 position, reproducing the observed regioselectivity.

- The rate determining step of the alkyne homocoupling is the reductive elimination. The corresponding transition state contains two copper centers and one ruthenium center, in total agreement with the experimental kinetic measurements, which established the optimal ratio of Cu:Ru in 2:1.

Chapter 4:

- We developed, in collaboration with the group of Prof. Llobet in ICIQ, a new family of mononuclear copper-based water oxidation catalysts.

- We characterized a novel pathway for the oxygen-oxygen bond formation step, which have been labeled Single Electron Transfer Water Nucleophilic Attack (SET-WNA). In this new pathway the O-O bond is produced in two consecutive step based on single electron transfers.

- The assignment by DFT of the catalytic wave to the ligand oxidation has opened the door to modifications in the ligand with introduction of donor groups that have led to a lowering the overpotential down to a record value of 170 mV.

- The SET-WNA mechanism has been demonstrated to operate in other copper based water oxidation catalysts. We validated the wide applicability of this mechanism in other two structurally diverse copper systems.

- The SET-WNA does not completely replace the conventional 2-electron WNA, which we have showed to remain operative in a classical ruthenium catalyst.

- We have built a general scheme of all the catalytic pathways available in the O-O bond formation step in water oxidation. This scheme will help the experimental chemists in the development of new catalysts.

Appendix

Goodvibes Code

The code was written in python and it is available with the tutorial and examples at https://github.com/bobbypaton/GoodVibes.

```
#!/usr/bin/python
from __future__ import print_function

# Comments and/or additions are welcome (send e-mail to:
# robert.paton@chem.ox.ac.uk

#############################################
###############################
#                              GoodVibes.py                              #
#  Evaluation of quasi-harmonic thermochemistry from Gaussian 09.      #
#  The partion functions are evaluated from vibrational frequencies   #
#  and rotational temperatures from the standard output.               #
#  The rigid-rotor harmonic oscillator approximation is used as        #
#  standard for all frequencies above a cut-off value. Below this,     #
#  two treatments can be applied: either low frequencies can be set    #
#  to a value of 100 cm-1 (as advocated by Cramer-Truhlar), or the     #
#  free-rotor approximation is applied below the cut-off, (proposed    #
#  by Grimme). A damping function interpolates between the RRHO and    #
```

```
#  free-rotor entropy treatment for  Svib to avoid a discontinuity.   #
#  Both approached avoide infinite values  of Svib as frequencies     #
#  tend to zero.                                                      #
#  The free energy can be evaluated for variable temperature,         #
#  concentration, vibrational scaling factor, and with a haptic       #
#  correction of the translational entropy in different solvents,     #
#  according to the amount of free space available. With a freq.      #
#  cut-off set to 0, the results will be identical to the standard    #
#  values output by the Gaussian program.                             #
#################################################
##################################
########  Written by:  Rob Paton
##############################################
########  Modified by:  Ignacio Funes-Ardoiz
################################
########  Last modified:  Apr 04, 2016
#######################################
#################################################
##################################

import sys, math, time
from glob import glob

from vib_scale_factors import scaling_data, scaling_refs

# PHYSICAL CONSTANTS
GAS_CONSTANT = 8.3144621
PLANCK_CONSTANT = 6.62606957e-34
BOLTZMANN_CONSTANT = 1.3806488e-23
SPEED_OF_LIGHT = 2.99792458e10
AVOGADRO_CONSTANT = 6.0221415e23
AMU_to_KG = 1.66053886E-27
autokcal = 627.509541
kjtokcal = 4.184
atmos = 101.325
def_cut = 100.0

# version number
__version__ = "1.0.1"

stars = "   " + "*" * 128
```

```
grimme_ref = "Grimme, S. Chem. Eur. J. 2012, 18, 9955-9964"
truhlar_ref = "Ribeiro, R. F.; Marenich, A. V.; Cramer, C. J.; Truhlar, D. G. J. Phys. Chem. B 2011, 115, 14556-14562"
goodvibes_ref = "Funes-Ardoiz, I.; Paton, R. S. (2016). GoodVibes: GoodVibes v1.0.1. http://doi.org/10.5281/zenodo.60811"
# Enables output to terminal and to text file
class Logger:
  # Designated initializer
  def __init__(self,filein,suffix,append):
    # Create the log file at the input path
    self.log = open(filein+"_"+append+"."+suffix, 'w' )

  # Write a message to the log
  def Write(self, message):
    # Print the message
    print(message, end='')
    # Write to log
    self.log.write(message)

  # Write a message only to the log and not to the terminal
  def Writeonlyfile(self, message):
    # Write to log
    self.log.write("\n"+message+"\n")

  # Write a fatal error, finalize and terminate the program
  def Fatal(self, message):
    # Print the message
    print(message+"\n")
    # Write to log
    self.log.write(message + "\n")
    # Finalize the log
    self.Finalize()
    # End the program
    sys.exit(1)

  # Finalize the log file
  def Finalize(self):
    self.log.close()

# Read gaussian output for the level of theory and basis set used
def level_of_theory(file):
```

```
    g09_output = open(file, 'r')
    inlines = g09_output.readlines()
    level = "none"
    bs = "none"
    for i in range(0,len(inlines)):
        if inlines[i].strip().find('\\Freq\\') > -1:
            if len(inlines[i].strip().split("\\")) > 5:
                level = (inlines[i].strip().split("\\")[4])
                bs = (inlines[i].strip().split("\\")[5])
    return level+"/"+bs

# translational energy evaluation (depends on temperature)
def calc_translational_energy(temperature):
    """
    Calculates the translational energy (kcal/mol) of an ideal gas - i.e.
    non-interactiing molecules so molar energy = Na * atomic energy
    This approximxation applies to all energies and entropies computed within
    Etrans = 3/2 RT!
    """
    energy = 1.5 * GAS_CONSTANT * temperature
    energy = energy/kjtokcal/1000.0
    #print "\nH_trans", energy
    return energy

# rotational energy evaluation (depends on molecular shape and temperature)
def calc_rotational_energy(zpe, symmno, temperature, linear):
    """
    Calculates the rotaional energy (kcal/mol)
    Etrans = 0 (atomic) ; RT (linear); 3/2 RT (non-linear)
    """
    if zpe == 0.0: energy = 0.0
    elif linear == 1: energy = GAS_CONSTANT * temperature
    else: energy = 1.5 * GAS_CONSTANT * temperature
    energy = energy/kjtokcal/1000.0
    #print "H_rot", energy
    return energy

# vibrational energy evaluation (depends on frequencies, temperature and scaling factor: default = 1.0)
def calc_vibrational_energy(frequency_wn, temperature,freq_scale_factor):
```

```
    """
    Calculates the vibrational energy contribution (kcal/mol)
    Includes ZPE (0K) and thermal contributions
    Evib = R * Sum(0.5 hv/k + (hv/k)/(e^(hv/KT)-1))
    """
    energy = 0.0
    frequency = [entry * SPEED_OF_LIGHT for entry in frequency_wn]
    for entry in frequency:
        factor = ((PLANCK_CONSTANT*entry*freq_scale_factor)/(BOLTZMANN_CONSTANT*temperature))
        temp = factor*temperature*(0.5 + (1/(math.exp(factor)-1)))
        temp = temp*GAS_CONSTANT
        energy = energy + temp
    energy = energy/kjtokcal/1000.0
    #print "H_vib", energy
    return energy

# vibrational Zero point energy evaluation (depends on frequencies and scaling factor: default = 1.0)
def calc_zeropoint_energy(frequency_wn,freq_scale_factor):
    """
    Calculates the vibrational ZPE (kcal/mol)
    EZPE = Sum(0.5 hv/k)
    """
    energy = 0.0
    frequency = [entry * SPEED_OF_LIGHT for entry in frequency_wn]
    for entry in frequency:
        factor = ((PLANCK_CONSTANT*entry*freq_scale_factor)/(BOLTZMANN_CONSTANT))
        temp = 0.5*factor
        temp = temp*GAS_CONSTANT
        energy = energy + temp
    energy = energy/kjtokcal/1000.0
    #print "H_zpe", energy
    return energy
```

```
# Computed the amount of accessible free space (ml per L) in solution accesible to a solute immersed in bulk solvent, i.e. this is the volume not occupied by solvent molecules, calculated using literature values for molarity and B3LYP/6-31G* computed molecular volumes.
def get_free_space(solv):
    """
    Calculates the free space in a litre of bulk solvent,
    based on Shakhnovich and Whitesides (J. Org. Chem. 1998, 63, 3821-3830)
    """
    solvent_list = ["none", "H2O", "Toluene", "DMF", "AcOH", "Chloroform"]
    molarity = [1.0, 55.6, 9.4, 12.9, 17.4, 12.5] #mol/l
    molecular_vol = [1.0, 27.944, 149.070, 77.442, 86.10, 97.0] #Angstrom^3

    nsolv = 0
    for i in range(0,len(solvent_list)):
        if solv == solvent_list[i]: nsolv = i

    solv_molarity = molarity[nsolv]
    solv_volume = molecular_vol[nsolv]

    if nsolv > 0:
        V_free = 8 * ((1E27/(solv_molarity*AVOGADRO_CONSTANT)) ** 0.333333 - solv_volume ** 0.333333) ** 3
        freespace = V_free * solv_molarity * AVOGADRO_CONSTANT * 1E-24
    else: freespace = 1000.0

#   print "free space", freespace
    return freespace

# translational entropy evaluation (depends on mass, concentration, temperature, solvent free space: default = 1000.0)
def calc_translational_entropy(molecular_mass, conc, temperature, solv):
    """
    Calculates the translational entropic contribution (cal/(mol*K)) of an ideal gas
    needs the molecular mass
    Convert mass in amu to kg; conc in mol/l to number per m^3
    Strans = R(Ln(2pimkT/h^2)^3/2(1/C)) + 1 + 3/2)
```

```
    """
    simass = molecular_mass*AMU_to_KG
    lmda = ((2.0*math.pi*simass*BOLTZMANN_CONSTANT*temperature)**0.5)/PLANCK_CONSTANT
    Ndens = conc*1000*AVOGADRO_CONSTANT
    freespace = get_free_space(solv)
    Ndens = Ndens / (freespace/1000.0)
    entropy = GAS_CONSTANT*(2.5+math.log(lmda**3/Ndens))/4.184
    return entropy

# electronic entropy evaluation (depends on multiplicity)
def calc_electronic_entropy(multiplicity):
    """
    Calculates the electronic entropic contribution (cal/(mol*K)) of the molecule
    Selec = R(Ln(multiplicity)
    """
    entropy = GAS_CONSTANT*(math.log(multiplicity))/4.184
    return entropy

# rotational entropy evaluation (depends on molecular shape and temp.)
def calc_rotational_entropy(zpe, linear, symmno, roconst, temperature):
    """
    Calculates the rotational entropy (cal/(mol*K))
    Strans = 0 (atomic) ; R(Ln(q)+1) (linear); R(Ln(q)+3/2) (non-linear)
    """
    # monatomic
    if roconst == [0.0,0.0,0.0]: return 0.0
    rotemp = [roconst[0]*PLANCK_CONSTANT*1000000000/BOLTZMANN_CONSTANT,roconst[1]*PLANCK_CONSTANT*1000000000/BOLTZMANN_CONSTANT,roconst[2]*PLANCK_CONSTANT*1000000000/BOLTZMANN_CONSTANT]

    # diatomic
    if 0.0 in rotemp:
        rotemp.remove(0.0)
        qrot = temperature/rotemp[0]
    else:
      qrot = math.pi*temperature**3/(rotemp[0]*rotemp[1]*rotemp[2])
```

```
        qrot = qrot ** 0.5

    qrot = qrot/symmno

    if zpe == 0.0: entropy = 0.0 # monatomic

    if linear == 1: entropy = GAS_CONSTANT * (math.log(qrot) + 1)
    else: entropy = GAS_CONSTANT * (math.log(qrot) + 1.5)

    entropy = entropy/kjtokcal
    return entropy

# rigid rotor harmonic oscillator (RRHO) entropy evaluation - this is the default
treatment
def calc_rrho_entropy(frequency_wn, temperature,freq_scale_factor):
    """
    Calculates the entropic contribution (cal/(mol*K)) of a harmonic oscillator for
    a list of frequencies of vibrational modes
    Sv = RSum(hv/(kT(e^(hv/KT)-1) - ln(1-e^(-hv/kT)))
    """
    entropy = []
    frequency = [entry * SPEED_OF_LIGHT for entry in fre-
quency_wn]
    for entry in frequency:
        factor =
((PLANCK_CONSTANT*entry*freq_scale_factor)/(BOLTZMANN_
CONSTANT*temperature))
        temp = factor*(1/(math.exp(factor)-1)) - math.log(1-math.exp(-
factor))
        temp = temp*GAS_CONSTANT/4.184
        entropy.append(temp)
    return entropy

# free rotor entropy evaluation - used for low frequencies below the cut-off if
qh=grimme is specified
def calc_freerot_entropy(frequency_wn, temperature,freq_scale_factor):
    """
    Calculates the entropic contribution (cal/(mol*K)) of a rigid-rotor harmonic oscil-
lator for
    a list of frequencies of vibrational modes
    Sr = R(1/2 + 1/2ln((8pi^3u'kT/h^2))
```

```
    """
    #??This is the average moment of inertia used by Grimme - is this optimal for every mode??
    Bav = 10.0e-44

    entropy = []
    frequency = [entry * SPEED_OF_LIGHT for entry in frequency_wn]

    for entry in frequency:
        mu = PLANCK_CONSTANT/(8*math.pi**2*entry*freq_scale_factor)
        muprime = mu*Bav/(mu +Bav)
        factor = (8*math.pi**3*muprime*BOLTZMANN_CONSTANT*temperature)/(PLANCK_CONSTANT**2)
        temp = 0.5 + math.log(factor**0.5)
        temp = temp*GAS_CONSTANT/4.184
        entropy.append(temp)
    return entropy

# A damping function to interpolate between RRHO and free rotor vibrational entropy values
def calc_damp(frequency_wn, FREQ_CUTOFF):
    """
    Calculates the Head-Gordon damping function with alpha=4
    """
    alpha = 4
    damp = []
    for entry in frequency_wn:
        omega = 1/(1+(FREQ_CUTOFF/entry)**alpha)
        damp.append(omega)
    return damp

# The funtion to compute the "black box" entropy values (and all other thermochemical quantities)
class calc_bbe:
    def __init__(self, file, QH, FREQ_CUTOFF, temperature, conc, freq_scale_factor,solv,spc):
        # Frequencies in waveunmbers
        frequency_wn = []
```

```
# Read commandline arguments
g09_output = open(file, 'r')

linear_mol = 0
roconst = [0.0,0.0,0.0]
symmno = 1
linkmax = 0
freqloc = 0
link = 0

#count number of links
for line in g09_output:
    # only read first link + freq not other link jobs
    if line.find("Normal termination") != -1:
        linkmax += 1
    if line.find('Frequencies --') != -1:
        freqloc = linkmax

g09_output.seek(0)

# Iterate over output
for line in g09_output:
    # link counter
    if line.find("Normal termination")!= -1:
        link += 1
        # reset frequencies if in final freq link
        if link == freqloc: frequency_wn = []
    # if spc specified will take last Energy from file, otherwise will break after freq calc
    if link > freqloc and spc == 0: break

      # Iterate over output
      #for line in g09_output:
    # look for low frequencies
    #if line.find("Proceeding to internal job step")!= -1: frequency_wn = [] #resets the array if frequencies have been calculated more than once
    if line.strip().startswith('Frequencies --'):
        for i in range(2,5):
            try:
                x = float(line.strip().split()[i])
                #  only deal with real frequencies
```

```
                        if x > 0.00: frequency_wn.append(x)
                    except IndexError:pass

            # For QM calculations look for SCF energies, last one will be the optimized energy
            if line.strip().startswith('SCF Done:'): self.scf_energy = float(line.strip().split()[4])
            # For ONIOM calculations use the extrapolated value rather than SCF value
            if line.strip().find("ONIOM: extrapolated energy") > -1: self.scf_energy = (float(line.strip().split()[4]))
            # For Semi-empirical or Molecular Mechanics calculations
            if line.strip().find("Energy= ") > -1 and line.strip().find("Predicted")==-1 and line.strip().find("Thermal")==-1: self.scf_energy = (float(line.strip().split()[1]))

            # look for thermal corrections, paying attention to point group symmetry
            if line.strip().startswith('Zero-point correction='): self.zero_point_corr = float(line.strip().split()[2])
            if line.strip().find('Multiplicity') > -1: mult = float(line.strip().split()[5])
            if line.strip().startswith('Molecular mass:'): molecular_mass = float(line.strip().split()[2])
            if line.strip().startswith('Rotational symmetry number'): symmno = int((line.strip().split()[3]).split(".")[0])
            if line.strip().startswith('Full point group'):
                if line.strip().split()[3] == 'D*H' or line.strip().split()[3] == 'C*V': linear_mol = 1
            if line.strip().startswith('Rotational constants'): roconst = [float(line.strip().split()[3]), float(line.strip().split()[4]), float(line.strip().split()[5])]

        # skip the next steps if unable to parse the frequencies or zpe from the output file
        if hasattr(self, "zero_point_corr"):

            # create an array of frequencies equal to cut-off value
            cutoffs = []
            for j in range(0,len(frequency_wn)): cutoffs.append(FREQ_CUTOFF)
```

```
        # Calculate Translational, Rotational and Vibrational contributions to the energy
        Utrans = calc_translational_energy(temperature)
        Urot = calc_rotational_energy(self.zero_point_corr, symmno, temperature,linear_mol)
        Uvib = calc_vibrational_energy(frequency_wn, temperature,freq_scale_factor)
        ZPE = calc_zeropoint_energy(frequency_wn, freq_scale_factor)

        # Calculate Translational, Rotational and Vibrational contributions to the entropy
        Strans = calc_translational_entropy(molecular_mass, conc, temperature, solv)
        Selec = calc_electronic_entropy(mult)
        Srot = calc_rotational_entropy(self.zero_point_corr, linear_mol, symmno, roconst, temperature)

        # Calculate harmonic entropy, free-rotor entropy and damping function for each frequency
        Svib_rrho = calc_rrho_entropy(frequency_wn, temperature,freq_scale_factor)
        if FREQ_CUTOFF > 0.0: Svib_rrqho = calc_rrho_entropy(cutoffs, temperature,1.0)
        Svib_free_rot = calc_freerot_entropy(frequency_wn, temperature,freq_scale_factor)
        damp = calc_damp(frequency_wn, FREQ_CUTOFF)

        # Compute entropy (cal/mol/K) using the two values and damping function
        vib_entropy = []
        for j in range(0,len(frequency_wn)):
          if QH == "grimme": vib_entropy.append(Svib_rrho[j] * damp[j] + (1-damp[j]) * Svib_free_rot[j])
          elif QH == "truhlar" and FREQ_CUTOFF > 0.0:
            if frequency_wn[j] > FREQ_CUTOFF: vib_entropy.append(Svib_rrho[j])
            else: vib_entropy.append(Svib_rrqho[j])

        # Add all terms to get Free energy - perform separately for harmonic and quasi-harmonic values out of interest
        qh_Svib = sum(vib_entropy)
        h_Svib = sum(Svib_rrho)
```

```
      self.enthalpy = self.scf_energy + (Utrans + Urot + Uvib +
GAS_CONSTANT*temperature/kjtokcal/1000.0)/autokcal
      self.zpe = ZPE/autokcal
      self.entropy = (Strans + Srot + h_Svib + Selec)/autokcal/1000.0
      self.qh_entropy = (Strans + Srot + qh_Svib + Se-
lec)/autokcal/1000.0
      self.gibbs_free_energy = self.enthalpy - temperature * self.entropy
      self.qh_gibbs_free_energy = self.enthalpy - temperature *
self.qh_entropy

      #Uncomment to compute the magnitude of the quasi-harmonic correction to
the RRHO entropy
      #QH_correction = h_Svib - qh_Svib
      # self.QH_correction = -QH_correction * temperature/1000.0

      #Uncomment to compute the magnitude of the haptic (i.e. concentration-
dependent) correction to the RRHO entropy
      #Strans1atm = calc_translational_entropy(molecular_mass, at-
mos/(GAS_CONSTANT*temperature), temperature, solv)
      #conc_correction = Strans - Strans1atm
      #self.conc_correction = -conc_correction * temperature/1000.0

if __name__ == "__main__":
  # Takes arguments: cutoff_freq g09_output_files
  files = []
  log = Logger("Goodvibes","dat", "output")
  QH = "grimme"; spc = "none"; FREQ_CUTOFF = "none"; tem-
perature = "none"; conc = "none"; freq_scale_factor = "none"; solv =
"none"; temperature_interval = []; conc_interval = []
  if len(sys.argv) > 1:
    for i in range(1,len(sys.argv)):
      if sys.argv[i] == "-f": FREQ_CUTOFF = float(sys.argv[i+1])
      elif sys.argv[i] == "-t": temperature = float(sys.argv[i+1])
      elif sys.argv[i] == "-qh": QH = (sys.argv[i+1]).lower()
      elif sys.argv[i] == "-c": conc = float(sys.argv[i+1])
      elif sys.argv[i] == "-v": freq_scale_factor = float(sys.argv[i+1])
      elif sys.argv[i] == "-s": solv = (sys.argv[i+1])
      elif sys.argv[i] == "-ti": temperature_interval =
list(eval(sys.argv[i+1]))
      elif sys.argv[i] == "-ci": conc = list(sys.argv[i+1])
      elif sys.argv[i] == "-spc": spc = 1
```

```
      else:
        if len(sys.argv[i].split(".")) > 1:
          if sys.argv[i].split(".")[1] == "out" or sys.argv[i].split(".")[1] ==
"log":
            for file in glob(sys.argv[i]): files.append(file)
    freespace = get_free_space(solv)

    start = time.strftime("%Y/%m/%d %H:%M:%S", time.localtime())
    log.Write("   GoodVibes v " + __version__ + ": "+start)
    log.Write("\n   REF: " + goodvibes_ref +"\n")

    if temperature != "none": log.Write("\n   Temperature =
"+str(temperature)+" Kelvin")
    else: log.Write("\n   Temperature (default) = 298.15K",); tempera-
ture = 298.15

    if conc != "none": log.Write("   Concn = "+str(conc)+" mol/l")
    else: log.Write("   Concn (default) = 1 atmosphere"); conc =
12.187274/temperature; conc_ini="None"

    if freq_scale_factor != "none": log.Write("   Frequency scale factor
= "+str(freq_scale_factor))
    else:
      l_o_t = []
      for file in files: l_o_t.append(level_of_theory(file))
      level_of_theory = l_o_t[0]
      for scal in scaling_data:
          if level_of_theory.upper().find(scal['level'].upper()) > -1 or
level_of_theory.upper().find(scal['level'].replace("-","").upper()) > -1:
            log.Write("\n\n   " + "Found vibrational scaling factor " +
str(scal['zpe_fac']) + " for " + level_of_theory + " level of theory")
            freq_scale_factor = scal['zpe_fac']; ref = scal-
ing_refs[scal['zpe_ref']]
            log.Write("\n   REF: " + ref)
      if freq_scale_factor == "none":
        log.Write("   Frequency scale factor (default) = 1.0");
freq_scale_factor = 1.0
      for level in l_o_t:
        if level != level_of_theory:
```

```
            log.Write("\n   WARNING - different levels of theory found - " + level_of_theory + " != " + level)

    if spc == "none": spc = 0
    else: log.Write("\n   Link job: combining final single point energy with thermal corrections")

    if freespace != 1000.0: log.Write("   Specified solvent "+solv+": free volume"+str("%.1f" % (freespace/10.0))+"(mol/l) corrects the translational entropy")

    if FREQ_CUTOFF == 0.0:
      log.Write("\n\n   Quasi-harmonic cut-off value = "+str(FREQ_CUTOFF)+" wavenumbers (no corrections applied!)")
      if QH == "truhlar": log.Fatal("\n   FATAL ERROR: The defined quasi-harmonic model is incompatible with a cut-off value of zero wavenumbers")

    elif FREQ_CUTOFF == "none":
      FREQ_CUTOFF = def_cut
    log.Write("\n\n   Quasi-harmonic treatment: frequency cut-off value of "+str(FREQ_CUTOFF)+" wavenumbers will be applied")

    if QH == "grimme":
       log.Write("\n   QH = Grimme: Using a mixture of RRHO and Free-rotor vibrational entropies"); qh_ref = grimme_ref
    elif QH == "truhlar": log.Write("\n   QH = Truhlar: Using an RRHO treatment where low frequencies are adjusted to the cut-off value"); qh_ref = truhlar_ref
    else: log.Fatal("\n   FATAL ERROR: Unknown quasi-harmonic model "+QH+" specified (QH must = grimme or truhlar)")
    log.Write("\n   REF: " + qh_ref)

  else: log.Fatal("\n   FATAL ERROR: Wrong number of arguments used.\n   Correct format: GoodVibes.py (-qh grimme/truhlar) (-f cut-off_freq) (-t temp) (-c concn) (-v scalefactor) g09_output_file(s)\n")

  # Standard mode: tabulate thermochemistry ouput from file(s) at a single temperature and concentration
  if len(temperature_interval) == 0 and len(conc_interval) == 0:
    log.Write("\n\n   "+"Structure".ljust(39))
```

```
    log.Write('{:>13} {:>10} {:>13} {:>10} {:>10} {:>13}
{:>13}'.format("E/au", "ZPE/au", "H/au", "T.S/au", "T.qh-S/au",
"G(T)/au", "qh-G(T)/au"))
    log.Write("\n"+stars)
    for file in files:
      bbe = calc_bbe(file, QH, FREQ_CUTOFF, temperature, conc,
freq_scale_factor, solv, spc)
      log.Write("\no ")
      log.Write((file.split(".")[0]).ljust(39))
      if hasattr(bbe, "scf_energy"):
log.Write('{:13.6f}'.format(bbe.scf_energy))
      else: log.Write("N/A   ")
      if not hasattr(bbe,"gibbs_free_energy"): log.Write("   Warning!
Couldn't find frequency information ...\n")
      else:
        if all(getattr(bbe, attrib) for attrib in ["zero_point_corr", "en-
thalpy", "entropy", "qh_entropy", "gibbs_free_energy",
"qh_gibbs_free_energy"]):
           log.Write('{:10.6f} {:13.6f} {:10.6f} {:10.6f} {:13.6f}
{:13.6f}'.format(bbe.zpe, bbe.enthalpy, (temperature * bbe.entropy),
(temperature * bbe.qh_entropy), bbe.gibbs_free_energy,
bbe.qh_gibbs_free_energy))
    log.Write("\n"+stars+"\n")

  #Running a variable temperature analysis of the enthalpy, entropy and the free
energy
  if len(temperature_interval) != 0:
    # If no temperature step was defined, divide the region into 10
    if len(temperature_interval) == 2: tempera-
ture_interval.append((temperature_interval[1]-
temperature_interval[0])/10.0)
    log.Write("\n\n   Running a temperature analysis of the enthalpy,
entropy and the entropy between")
    log.Write("\n   T_init:  %.1f,  T_final:  %.1f,  T_interval: %.1f" %
(temperature_interval[0], temperature_interval[1], tempera-
ture_interval[2]))
    temperature = float(temperature_interval[0])

    log.Write("\n\n   "+"Structure".ljust(39))
```

```
    log.Write('{:>13} {:>13} {:>10} {:>10} {:>13}
{:>13}'.format("Temp/K", "H/au", "T.S/au", "T.qh-S/au", "G(T)/au",
"qh-G(T)/au"))
    for file in files:
      #output_file = file.split(".")[0] + "_temperature.txt"
      #temperature_txt = open(output_file,"w")
      log.Write("\n"+stars[:120])

      for i in range(int(temperature_interval[0]),
int(temperature_interval[1]+1), int(temperature_interval[2])):
        temperature = float(i)
        log.Write("\no  "+file.ljust(39))
        log.Write('{:13.1f}'.format(temperature))
        if conc_ini == "None": conc =  at-
mos/(GAS_CONSTANT*temperature)
        bbe = calc_bbe(file, QH, FREQ_CUTOFF, temperature, conc,
freq_scale_factor, solv, spc)
        if not hasattr(bbe,"gibbs_free_energy"): log.Write("Warning!
Couldn't find frequency information ...\n")
        else:
          if all(getattr(bbe, attrib) for attrib in ["enthalpy", "entropy",
"qh_entropy", "gibbs_free_energy", "qh_gibbs_free_energy"]):
            log.Write('{:13.6f} {:10.6f} {:10.6f} {:13.6f}
{:13.6f}'.format(bbe.enthalpy, (temperature * bbe.entropy), (tempera-
ture * bbe.qh_entropy), bbe.gibbs_free_energy,
bbe.qh_gibbs_free_energy))
      log.Write("\n"+stars[:120]+"\n")
  log.Finalize()

##################################
##################################
##################################
```